1-1-2014

Membrane Forces and Key Protein Determinants of Hematopoietic Cell Function: Lamins and Myosin-II in Hematopoiesis and CD47 in Immunotherapy of Cancer

Kyle Spinler
University of Pennsylvania, kspinler@seas.upenn.edu

Membrane Forces and Key Protein Determinants of Hematopoietic Cell Function: Lamins and Myosin-II in Hematopoiesis and CD47 in Immunotherapy of Cancer

Abstract

Hematopoiesis in human bone marrow generates every second about 10^5 – 10^6 anucleated platelets and red blood cells as well as nucleated white blood cells that are capable of infiltrating distant tissues. The thesis begins in the marrow with a description of (1) nuclear membrane 'lamina' physicochemical properties that influence marrow-to-circulation trafficking, and proceeds to detail (2) the physicochemical roles of membrane cortex 'myosin' in key marrow processes of motility and division as well as platelet biogenesis and disease. The thesis finishes with (3) studies of macrophages in peripheral tissues far from the marrow and aspects of how such cells distinguish 'foreign' cells from 'self' cells.

Collaborative studies show the lamin–A:B ratio controls nuclear viscoelasticity and in turn cell trafficking relevant to marrow escape. Additionally, differential lamin expression can direct erythroid and megakaryocyte differentiation. Secondly, xenografts show that MIIB is required for blood cell generation, while MIIA is required for long–term HSC/P engraftment. MII inhibition by blebbistatin prior to xenotransplantation enriches for long–term hematopoietic multilineage reconstituting cells, and also multi–nucleated megakaryocytes. Cone and plate rheometry demonstrates an optimal shear stress for platelet–like–particle generation from MKs that is enhanced by MII inhibition, and that MIIA heavy chain phosphorylation at S1943 is shear sensitive. Micropipette aspiration of MKs with mutations of the MIIA gene, *MYH9*, recapitulates *MYH9*–RD macrothrombocytopenia. Comparing *MYH9*–RD patient and normal donor platelets shows a similarity in pre/pro-platelets when normals are treated with blebbistatin. These findings provide evidence that regulation of MIIA activity through S1943 phosphorylation is critical to proper MK fragmentation and proplatelet fission to generate platelets of normal size and number.

The dissertation concludes with an investigation of an immunotherapy approach to treat peripheral solid tumors by controlling tumor cell CD47 expression and administering an anti–human polyclonal IgG antibody. These *in vivo* xenograft models provide a mechanism of selective tumor clearance driven by FcR stimulation of macrophages. In all, this work highlights biophysical factors of cortical and nuclear membranes that govern hematopoietic differentiation and trafficking, normal and pathological thrombopoiesis, and a mechanism of phagocytic clearance of cancer cells through CD47 attenuation and species specific but epitope non–specific antibody infusion.

Degree Type
Dissertation

Degree Name
Doctor of Philosophy (PhD)

Graduate Group
Chemical and Biomolecular Engineering

MEMBRANE FORCES AND KEY PROTEIN DETERMINANTS OF HEMATOPOIETIC CELL FUNCTION: LAMINS AND MYOSIN-II IN HEMATOPOIESIS AND CD47 IN IMMUNOTHERAPY OF CANCER

Kyle Richard Spinler

A DISSERTATION

In

Chemical and Biomolecular Engineering

Presented to the Faculties of the University of Pennsylvania in Partial

Fulfillment of the Requirements for the Degree of Doctor of Philosophy

2014

Supervisor of Dissertation:

Signature: _____
Dennis E. Discher, Ph.D., Robert D. Bent Professor of Chemical and Biomolecular Engineering

Graduate Group Chairperson:

Signature: _____
Raymond Gorte, Ph.D., Professor of Chemical and Biomolecular Engineering

Dissertation Committee:
Mortimer Poncz, M.D., Professor of Pediatrics
Scott L. Diamond, Ph.D., Humphrey Professor of Chemical and Biomolecular Engineering
Kathleen Stebe, Ph.D., Goodwin Professor of Chemical and Biomolecular Engineering

MEMBRANE FORCES AND KEY PROTEIN DETERMINANTS OF HEMATOPOIETIC CELL FUNCTION: LAMINS AND MYOSIN-II IN HEMATOPOIESIS AND CD47 IN IMMUNOTHERAPY OF CANCER

Kyle Richard Spinler

ACKNOWLEDGEMENTS

I would first like to express my sincerest gratitude to my mentor and thesis advisor Dr. Dennis Discher without whom none of this would have been possible. He had the faith in me to allow me to work on this project without a substantial background in either cell biology or biophysics. His belief drove me to not let him down and to do so meant I always read one more paper or made time for one more seminar or class. Under his tutelage my knowledge and experience has grown exponentially. I have been afforded the opportunity to work on a variety of projects with a diverse group of people. When I started grad school I do not think I ever would have thought that I would be leaving having worked with mice, but five years later that is exactly where things stand. For that I am greatly appreciative of Dr. Discher supporting me in these latest endeavors. I would also like to thank him for instilling in me the approach to research and manuscript writing in which one should start writing the paper from the onset. Writing a research paper can be a daunting challenge, but with his guidance the process feels much more like crafting a narrative. We always focus on the "story" and what the data is telling us. Using this framework it was amazing how my megakaryocyte paper morphed from its initial focus to its much broader and translatable current form. I can saw without a doubt that these things that I take from Dr. Discher will aid me throughout my career.

I would also like to thank the members of my thesis committee: Dr. Kathleen Stebe, Dr. Scott Diamond, and Dr. Mortimer Poncz for their guidance, support, and connections to collaborators. One such collaborator that I would like to thank is Dr. Michele Lambert from CHOP who, through Dr. Poncz, I was granted access to one of her

MYH9-RD patients. Dr. Lambert also provided valuable guidance from the viewpoint of a hematologist when in came time to write my MK paper and council whenever I found holes in the existing literature.

Within the Discher Lab, I would like to thank members current and past including Drew Bradshaw, Dr. Amnon Buxboim, Dave Dingal, Takamasa Harada, Jerome Irianto, Dr. Irena Ivanovska, Praful Nair, Edward Pratt, Pia Rodriguez, Nisha Sosale, Dr. Joe Swift, and Manu Tewari. I would like to acknowledge the productive, and sometimes not so productive, discussions and often, for providing critical hands-on training.

I would especially like to thank former colleague Dr. Jae-Won Shin who in a granular sense is really the reason I was able to get anything done at all. He taught me nearly every lab technique that I use today. Additionally, he provided a strong knowledge base from which my work emerged. To this day he continues to be a great source of advice on anything from research related or the most mundane everyday problems.

One other former lab member that I would like to specifically mention is Dr. David Christian. When I first started in the Discher Lab he was the person responsible for acclimating me to the lab. More recently, he has provided beneficial instruction and advisement when it comes to mouse husbandry and experimentation.

Similarly, I would also like to thank Anthony Secreto and Joshua Glover both from the Stem Cell and Xenograft Core whom have also taught and advised me on not only husbandry, but also animal acquisition and *in vivo* experimental design.

Finally, I owe a tremendous debt of gratitude to my family, my mom especially. Since my dad passed away in 2005 I cannot imagine how hard it must be to have your only child have way across the country and only seeing him twice a year. I want to

apologize for all of the heartache this must have caused you, but know that I am thankful for your encouragement and belief in my pursuit of education. To my father, if my actions do not already convey this, I want to make it clear that everything I do, I do with you in mind. Your memory, the lessons you taught me, and the virtues you instilled in me will always live on. Regardless of whether your battle with leukemia led me down my current path of research serendipitously, it is my motivation and has become my mission in life.

ABSTRACT

MEMBRANE FORCES AND KEY PROTEIN DETERMINANTS OF HEMATOPOIETIC CELL FUNCTION: LAMINS AND MYOSIN-II IN HEMATOPOIESIS AND CD47 IN IMMUNOTHERAPY OF CANCER

Kyle R. Spinler

Dennis E. Discher

Hematopoiesis in human bone marrow generates every second about 10^5 – 10^6 anucleated platelets and red blood cells as well as nucleated white blood cells that are capable of infiltrating distant tissues. The thesis begins in the marrow with a description of (1) nuclear membrane 'lamina' physicochemical properties that influence marrow-to-circulation trafficking, and proceeds to detail (2) the physicochemical roles of membrane cortex 'myosin' in key marrow processes of motility and division as well as platelet biogenesis and disease. The thesis finishes with (3) studies of macrophages in peripheral tissues far from the marrow and aspects of how such cells distinguish 'foreign' cells from 'self' cells.

Collaborative studies show the lamin-A:B ratio controls nuclear viscoelasticity and in turn cell trafficking relevant to marrow escape. Additionally, differential lamin expression can direct erythroid and megakaryocyte differentiation. Secondly, xenografts show that MIIB is required for blood cell generation, while MIIA is required for long-term HSC/P engraftment. MII inhibition by blebbistatin prior to xenotransplantation

enriches for long-term hematopoietic multilineage reconstituting cells, and also multi-nucleated megakaryocytes. Cone and plate rheometry demonstrates an optimal shear stress for platelet-like-particle generation from MKs that is enhanced by MII inhibition, and that MIIA heavy chain phosphorylation at S1943 is shear sensitive. Micropipette aspiration of MKs with mutations of the MIIA gene, *MYH9*, recapitulates *MYH9*-RD macrothrombocytopenia. Comparing *MYH9*-RD patient and normal donor platelets shows a similarity in pre/pro-platelets when normals are treated with blebbistatin. These findings provide evidence that regulation of MIIA activity through S1943 phosphorylation is critical to proper MK fragmentation and proplatelet fission to generate platelets of normal size and number.

The dissertation concludes with an investigation of an immunotherapy approach to treat peripheral solid tumors by controlling tumor cell CD47 expression and administering an anti-human polyclonal IgG antibody. These *in vivo* xenograft models provide a mechanism of selective tumor clearance driven by FcR stimulation of macrophages. In all, this work highlights biophysical factors of cortical and nuclear membranes that govern hematopoietic differentiation and trafficking, normal and pathological thrombopoiesis, and a mechanism of phagocytic clearance of cancer cells through CD47 attenuation and species specific but epitope non-specific antibody infusion.

TABLE OF CONTENTS

LIST OF TABLES

LIST OF FIGURES

LIST OF ABBREVIATIONS

7-AAD: 7-Aminoactinomycin D
Ab: rabbit anti-human RBC antibody
ADCC: Antibody Dependent Cell-mediated Cytotoxicity
AF: Alexa Fluor
AML: Acute Myeloid Leukemia
AJ: Aster-Jandel
APC: Allophycocyanin
BFU-E: Erythroid Burst-Forming Units
Bleb: Blebbistatin
BM: Bone Marrow
BMT: Bone Marrow Transplant
BSA: Bovine Serum Albumin
C: Celsius
CD: Cluster of Differentiation
CD47 KD^{+} or KD^{++}: tdTomato A549 CD47 knockdown or deep knockdown
CFSE: Carboxy-Fluorescein Succinimidyl Ester
CFU-E: Colony Forming Unit-Erythroid
CFU-GEMM: Colony Forming Unit -Granulocyte, Erythroid, Monocyte, and Megakaryocyte
CFU-GM: Colony Forming Unit -Granulocyte and Monocyte
CK-II: Casein Kinase-II
CLL: Chronic Lymphocytic Leukemia
CLP: Common Lymphoid Progenitor
CMP: Common Myeloid Progenitor
CRT: Calreticulin
Cy7: Cyanine 7 dye
d: day
DMSO: Dimethyl Sulfoxide
DNA: Deoxyribonucleic Acid
E: Elasticity
ECM: Extracellular Matrix
EDTA: Ethylenediaminetetraacetic Acid
ELC: Essential Light Chains
Epo: Erythropoietin
Ery: Erythroid
ESC: Embryonic Stem Cell
$F(ab')_2$: Fragment Antigen Binding dimer (Fc excised immunoglobulin)
FBS: Fetal Bovine Serum
FcR: Fragment Crystallizable region Receptor
FITC: Fluorescein
fL: femtoliter
G-CSF: Granulocyte Colony-Stimulating Factor
GFP: Green Fluorescent Protein

G/M: Granulocyte/Monocyte
GMP: Granulocyte-Monocyte Progenitor
GPA: Glycophorin A
hr: hour
HSC/P: Hematopoietic Stem Cell/Progenitor
IC50: half maximal Inhibitory Concentration
IL-3: iInterleukin-3
IgG: Immunoglobulin G
ITP: Idiopathic Thrombocytopenic Purpura
J: Compliance
KD or k.d.: knockdown
kDA: kilodalton
kPa: kilopascal
LPH: Liposome-Protamine-Hyaluronic acid
LSK: $Lin^{-}Sca\text{-}1^{+}c\text{-}Kit^{+}$
M: molar
M1 or M2: activated, differentially polarized Macrophage
MIIA, B, C: Non-muscle myosin IIA, B, C
Mϕ: Macrophage
MEP: Megakaryocyte-Erythroid Progenitor
MFI: Mean Fluorescence Intensity
min: minute
MLCK: Myosin Light Chain Kinase
MM: Multiple Myeloma
MPV: Mean Platelet Volume
MK: Megakaryocyte
MT: Microtubule
μL: microliter
μm: micrometer
μM: micromolar
mg: milligram
mL: milliliter
mM: millimolar
MPP: Multi-Potent Progenitor
MSC: Mesenchymal Stem Cell
MYH9-RD: *MYH9*-Related Disease
NHL: Non-Hodgkin's Lymphoma
NK cells: Natural Killer cells
NSG: Non-Obese Diabetic / Severe Combined Immunodifficiency / IL-2R$\gamma^{-/-}$
Pa: Pascal
PB: Peripheral Blood
PE: Phycoerythrin
PLP: Platelet-Like-Particle
PRP: Platelet Rich Plasma
pS1943: Phosphorylation of Serine 1943 residue in MIIA

RBC: Red Blood Cell
Rh: Rhesus Factor
RLC: Regulatory Light Chains
ROCK: Rho-associated protein Kinase
RT: Room Temperature
SCF: Stem Cell Factor
Scr: Scrambled
SDF-1: Stromal Derived Factor-1
SDS-PAGE: Sodium Dodecyl Sulfate Polyacrylamide Gel Electrophoresis
SEM: Standard Error of the Mean
shRNA: Short-Hairpin Ribonucleic Acid
siRNA: Small Interfering Ribonucleic Acid
SIRPα: Signal Regulatory Protein α
SRF: Serum Response Factor
TAM: Tumor Associated Macrophage
Tax or Taxol: Paclitaxel
tdTomato: Tandem Dimer Tomato
TGF-β: Transforming Growth Factor β
Tpo: Thrombopoietin
WT: Wild-Type
WT Scr: tdTomato A549 expressing normal levels of CD47

CHAPTER 1: INTRODUCTION

1.1 SIGNIFICANCE

Adult stem cells of many diverse tissue types have been an intense area of research since the first human bone marrow transplant (BMT) (Thomas et al., 1957) and the discovery of hematopoietic stem cell/progenitors (HSC/Ps) by clonal assay (Becker et al., 1963). These cells have the capacity to either integrate in a target tissue or act as vehicles to deliver signals without integration (Daley and Scadden, 2008). More than 50,000 BMT procedures were performed in 2006 saving a large percentage of otherwise untreatable patients (Gratwohl et al., 2010). While BMT is successful for many recipients, many other patients are not as fortunate. Such limitations have motivated researchers to elucidate mechanisms by which a few, or even a single, stem cell(s) can generate an entire, regenerating tissue. The demands of the human hematopoietic system are exceptionally great. The human body generates $3x10^{10}$ nucleated blood cells, $2x10^{13}$ anucleated red blood cells (RBCs), and $1x10^{11}$ platelets daily. Factors that regulate HSC proliferation, differentiation, and dispersion continue to be defined, and include biophysical forces and membrane mechanics that are addressed throughout the following chapters.

Advances in isolation and identification of HSC/Ps versus committed lineages have defined the hematopoietic hierarchy. Of particular importance has been the isolation of HSC/Ps by flow cytometry based on particular sets of surface antigens (Weissman and Shizuru, 2008) combined with quantification of HSC frequency by means of limiting dilution transplantations (Szilvassy et al., 1990). In addition to these methods, numerous soluble growth factors have been identified that support and drive differentiation of various blood lineages. Despite these advances, much less is known about *in vivo*

physical factors that might govern HSC self-renewal and commitment. A stem cell "niche" was proposed to be a requirement for long-term hematopoiesis from HSCs (Schofield, 1978). Further understanding of the niche is likely to reveal strategies of HSC/P direction *ex vivo* that will allow enhancement of *in vivo* engraftment in patients. Such efforts will also benefit *ex vivo* production of mature blood cell products, particularly RBCs and platelets that are very commonly transfused. Despite the discovery of erythropoietin (Epo) (Miyake et al., 1977) and thrombopoietin (Tpo) (Kaushansky et al., 1994) as cytokines that facilitate erythroid and megakaryocyte (MK) differentiation from HSC/Ps, *in vitro* generation of terminally differentiated cells in quantities large enough to meet demand has remained elusive. Further, none of the growth factors, cytokines, or chemokines has yet proven sufficient to reproduce artificial marrow-like environments conducive to generation of all blood cell-types from HSC/Ps.

Conversion of extracellular mechanical inputs to intracellular signals, both biochemical and biophysical has been termed mechanotransduction (Wang et al., 2009). Mechanotransduction is mediated by intracellular tension that is sustained by adhesion to matrix or other cells and generated by the actin-myosin-based cytoskeleton (Discher et al., 2005), which in turn couples to the nucleus (Pajerowski et al., 2007). Since HSC/Ps and derived lineages intimately interact in numerous ways with their microenvironments, microenvironment mechanical aspects can in principle regulate stem and progenitor cell functionality. Stem cells generate forces in processes ranging from cell division to migration, while external stresses in stem cell microenvironments, including fluid flows, impact adhesion and associated signaling so do mechanical factors and nuclear elasticity of HSC/Ps (Pajerowski et al., 2007; Shin et al., 2011). All of these structures with

mechanical functions can impact stem cell maintenance, lineage specification, and trafficking. Therefore, nuclear lamin and myosin-II (MII) will be investigated in the context of HSC/P lineage commitment and marrow egress followed by an examination of the regulation of MII activity and pathology in thrombopoiesis.

Cortical and nuclear membranes not only facilitate migration of hematopoietic cells within the marrow, out of the marrow, and throughout the circulation, but extravasation from the peripheral blood (PB) to surrounding tissue as well. Leukocytes, particularly macrophages, actively transit between circulation and tissue in response to inflammation. Macrophages can be either pro- or anti-tumorigenic depending on their polarization, either M2 or M1 respectively (Mantovani et al., 2002; Murdoch et al., 2008). The invasiveness of macrophages allows these cells to respond to antigens far from circulation. One such signal that triggers macrophage action is cell surface expressed CD47. Human tissues ubiquitously express CD47 on their surface to avoid their phagocytosis by patrolling macrophages. CD47 expression on circulating blood cells is particularly important as these cells encounter macrophages in much greater frequency. In fact, as RBCs age, they lose CD47 to effectively mark them for clearance. CD47 acts as a "don't eat me" signal by interaction with SIRPα on the phagocyte (Rodriguez et al., 2013). It has been shown in numerous types of cancer that CD47 is expressed at abnormally high levels providing tumor cells an immunologic invisibility (Jaiswal et al., 2009). Others have shown that patients with tumors expressing higher CD47 have worse tumor progression and are less successfully treated (Majeti et al., 2009). The capacity for macrophages to infiltrate deep into tissue, discriminate between

self and foreign, and selectively clear non-self cells introduces the potential to augment the efficacy of chemotherapeutic and immunotherapeutic modalities.

1.2 ACTOMYOSIN FORCES IN STEM CELLS AND PROGENITORS

Cells generate intracellular forces with actin and MII in response to extracellular mechanical cues ranging from matrix adhesion to fluid shear stress. These force generating processes are important to a myriad of biological functions relevant to differentiation, including cytokinesis, cortical tension, and migration. Of particular relevance to the work to follow, MII, is a crucial force generating motor and plays a major role in hematopoietic tissues and stem and progenitor cell contexts. Actin is a principal filamentous constituent of the cytoskeleton that can also translocate to the nucleus as a monomer. Myosin motor proteins pull on actin filaments by dynamically crosslinking and translating along the filaments in a process driven by ATP hydrolysis (Pollard and Korn, 1973). These activities can impact actin monomer pools (Wilson et al., 2010) that in turn can impact serum response factor (SRF), which is an ubiquitous actin regulated transcription factor with multiple co-factors that traffic between the cytoplasm and nucleus (Olson and Nordheim, 2010). Non-muscle cells express isoforms of MII that assemble in small mini-filaments that appear notably less ordered than in muscle. *MYH9, MYH10,* and *MYH14* are the genes encoding for the three MII heavy chain isoforms A, B, and C respectively. Hematopoietic cells express A and B isoforms, but not C, and these cells show dynamic expression patterns during differentiation (Engler et al., 2006). Additionally, the A:B ratio increases as megakaryocytes mature

ultimately leading to exclusive expression of A type MII in platelets (Lordier et al., 2012).

MIIA knockout is embryonic lethal in mice at E6.5 with defects in visceral endoderm morphogenesis and overall tension of the embryo, which appears flaccid (Conti et al., 2004). Together, these defects are a result of the inability to differentiate despite the capacity to adhere and divide. MIIB knockout mice survive longer, but die at E14.5 due to abnormalities in heart and brain that include more binucleated cells (Takeda et al., 2003; Tullio et al., 1997). Myosin-II deletion in *Dictyostelium* leads to increased distortion of the cell membrane and multinucleation in suspension cultures where cells cannot crawl apart to facilitate division (Merkel et al., 2000). Pharmacological inhibition of MII in adherent cells by blebbistatin also tends to increase the number of binucleated cells, indicating a role for MII in efficient cytokinesis (Straight et al., 2003). MII is also important in matrix sensing. Blebbistatin eliminates the effect of matrix elasticity on lineage specification of MSCs (Engler et al., 2006) and also maintenance of HSC/P numbers on highly flexible tropoelastin surfaces (Holst et al., 2010).

MII levels vary markedly between cell types as well as during differentiation, and MII is capable of rapidly responding to changes in intracellular and extracellular forces through changes in its phosphorylation states. MII is comprised of two heavy chains (230 kDa), two essential light chains (17 kDa), and two regulatory light chains. Myosin heavy chain consists of an ATP-hydrolyzing N-terminal motor domain head, which directly interacts with F-actin, and a ~150 nm long C-terminal helical tail that forms coiled-coil dimers which can further assemble into myosin filaments (Adelstein et al., 1972). Essential light chains are required for heavy chain stabilization (Hernandez et al., 2007).

Numerous studies, such as the one by Matsumura (Matsumura, 2005), have shown that regulatory light chains (RLC) modulate MII activity via phosphorylation by numerous kinases, including myosin light chain kinase (MLCK) and Rho-associated protein kinase (ROCK), both of which can phosphorylate the Thr18 and Ser19 RLC residues. MII heavy chain can be phosphorylated at Ser1943 in the tail and Tyr277 in the head. Protein kinase C and casein kinase-II phosphorylate the heavy chain, but additional kinases are likely relevant (Dulyaninova et al., 2005; Even-Faitelson and Ravid, 2006). Since the heavy chain directly binds with F-actin, regulation of heavy chain phosphorylation seems likely to have the most direct impact on MII activity compared to RLC. Recent mutagenesis studies implicate MIIA phosphorylation in regulating polyploidization of MKs more dramatically than inhibitors of MLCK or ROCK (Shin et al., 2011).

Although MII's functions in early HSC/Ps remain elusive, it nonetheless plays critical roles in differentiated hematopoietic lineages. In lymphoid cells, MII plays roles in the critical functioning of natural killer cells (Andzelm et al., 2007), T-Cells (Ilani et al., 2009; Jacobelli et al., 2010; Rey et al., 2007; Samaniego et al., 2007), and B-cells (Vascotto et al., 2007). In myeloid cells, MII is required in dendritic cells (Faure-André et al., 2008; Fernandez et al., 2011), neutrophils (Shin et al., 2010), and macrophage phagocytosis (Tsai and Discher, 2008). Actin-mediated forces have been shown to contribute to enucleation in erythroid lineages (Koury et al., 1989). *MYH9* mutations in MK lineages are associated with May-Hegglin anomaly, Fechtner Syndrome, Sebastian Syndrome (all part of a general classification of *MYH9*-related disorders). Such mutations are responsible for low platelet counts (thrombocytopenia) and abnormally large platelets (Kelley et al., 2000; Seri et al., 2000). Transgenic mice recapitulating *MYH9*-RD show

longer bleeding times and defects in clot retraction in addition to thrombocytopenia (Zhang et al., 2012). While *MYH9* mutations appear to impair platelet generation, other previous studies using *in vitro* MKs show increased proplatelet formation upon MII knockout or pharmacological inhibition (Chen et al., 2007; Eckly et al., 2009). Indeed, blebbistatin promotes platelet-like fragmentation by the fluid stresses that mimic shear stress in capillaries of the marrow (Shin et al., 2011). Despite these complications, actomyosin forces are an attractive target for mechanically modulating hematopoiesis in lineage specification and/or function.

1.3 DEFORMABILITY OF THE CELL CORTEX AND NUCLEUS PERMITS EGRESS FROM THE NICHE

For stem cells and their progeny, adhesion, retention, migration, and egress from a niche are all processes grounded, at least in part, on cell mechanics. While some mature blood cells such as RBCs and platelets must enter the circulation to carry out their role, at least some of the immature HSC/Ps must be retained in the marrow to sustain long-term hematopoiesis. The deformability of hematopoietic cells can change during differentiation, thus this property is likely a factor in regulating cell trafficking under mechanically constrained conditions that involve migration across the marrow-blood endothelial barrier and into 2-3 μm diameter capillaries. An early micropipette study showed that a 20-fold increase in aspiration pressure was necessary to deform myeloid progenitors (immature myeloblasts) compared to more deformable mature granulocytes (Lichtman, 1970). Additionally, myeloblasts cannot transit through 1-8 μm pores under a

chemotactic gradient, whereas the deformable mature granulocytes can (Giordano and Lichtman, 1973). How hematopoietic differentiation leads to changes in the deformability of cells and hence trafficking has, until now, not been deeply investigated. Recent studies with MSC migration through 3D gels (Raab et al., 2012) has provided additional credence to the hypothesis that both cell cortex and nucleus likely contribute to overall cell deformability and thereby impacting cell motility, niche retention, and trafficking.

In the context of fluid flow stresses on blood cells, membrane deformability has been characterized for platelets (White et al., 1984), megakaryocytes (Smith et al., 1989), granulocyte and lymphocytes (Dong et al., 1991), and RBCs (Discher et al., 1994). From these studies it is clear that the cytoskeleton specialization is a particularly key part of each cell type's program. In contrast to granulocyte differentiation, erythroid progenitors are stiffer than mature RBCs (Waugh et al., 2001). Nucleus stiffening could be a driving factor for enucleation to allow egress of RBCs (Lichtman et al., 1989). In general, primitive stem cells tend to be soft, perhaps due to the immature cytoskeletal architecture, and thus allow cell plasticity to be particularly susceptible to physical changes in external forces in their surroundings. For example, undifferentiated ESCs are 10-fold softer than differentiated progeny and posses higher sensitivity to a local cyclic stress that triggers cell spreading and differentiation (Chowdhury et al., 2010).

Since MII regulates cortical stiffness, whether HSC/Ps are softer than differentiated cells is likely dependent on the absolute abundance of MII isoforms during hematopoiesis. Myosin-II itself is sensitive to external force and has shown to become polarized and assemble in regions of high stress (Reichl et al., 2008). In the epithelial-to-mesenchymal transition, cells undergo MII isoform switching from C to B, promoting

cell motility and invasion (Beach et al., 2011). In this vein, recent work has shown that MII isoform switching between A and B regulates differentiation and motility of hematopoietic cells (Shin et al., 2014).

Hematopoietic cells have a small cytoplasmic volume, and so in addition to cell cortex, the nucleus is likely to contribute to overall cell deformability and trafficking. Nuclear deformability is largely understudied in the hematopoietic system and only recently has deformability of isolated nuclei or nuclei in living cells been probed with micropipette aspiration (Ivanovska et al., 2010). Previous studies from the Discher group have indicated that nuclei in human hematopoietic $CD34^+$ cells from marrow were slightly stiffer than nuclei from human ESCs but considerably softer than other differentiated nuclei suggesting that nuclear deformability is developmentally regulated (Pajerowski et al., 2007). Furthermore, the same study demonstrated that nuclear stiffness is dependent on lamins, which are intermediate filaments that assemble as coiled-coil dimers at the nuclear envelope and associate at least indirectly with chromatin (Shimi et al., 2010). Using micropipette and entry into 3D pores, our group has provided further evidence to the involvement of lamins in nuclear stiffness which further supports the relevance of nuclear deformability in the hematopoietic system (Shin et al., 2013). One hypothesis is that the polyploidy nucleus of the MK is too large and rigid to allow egress into the blood, but extension of membrane projections is permissive. These extensions fragment under shear flow to generate platelets as seen by *in vivo* imaging (Junt et al., 2007). Additionally, lamin-A, C is strongly upregulated upon T-cell activation (Andrade et al., 2003) and this could similarly favor retention of a T-cell at a site of inflammation. Similar to the hypothesis that MII actively regulates deformability of the cell cortex, it

appears reasonable to propose that differential lamin expression regulate nuclear stiffness throughout hematopoiesis and that this influences the ability of cells to migrate through and within the dense marrow or tissue and across the endothelium into the blood circulation.

1.4 PHYSIOLOGICAL SHEAR FLOW INFLUENCES LINEAGE DIFFERENTIATION

Fluid shear forces are an important external biophysical factor to consider in the context of differentiation. Such forces have been investigated most extensively with endothelial cells (due to direct exposure to blood flow) but also to a lesser extent with osteocytes which experience distinct fluid flows as bone is stressed in daily activity (Weinbaum et al., 1994). Endothelial cells can be differentiated from ESCs upon shear flow *in vitro* via the downstream activation of histone deacetylase 3 (Zeng et al., 2006), and osteoblast differentiation from BM-derived MSCs is facilitated by continuous shear *in vitro* (Stiehler et al., 2009). Additionally, controlled shear flow *in vitro* induces differentiation from embryoid-body-derived cells into hematopoietic precursors as indicated by a strong upregulation of the Runx1 transcription factor (Adamo et al., 2009). Zebrafish models also show that both chemical and genetic ablation of blood flow severely reduces HSC number (North et al., 2009).

Interplay between intrinsic and extrinsic mechanical factors likely contributes to cells fates. Fluid shear produces forces that are balanced by cell adhesions and the actomyosin cytoskeleton otherwise fluid shear can be so strong that it dominates to convect and disperse cells or even fragment them such as shown in platelet generation

(Junt et al., 2007). Additionally, an absence of adhesion to external surfaces for many cell types limits cytokinesis, those cells that do survive tend to become multi-nucleated in suspension, whereas adhesion-based traction forces help cells pull apart (Ben-Ze'ev and Raz, 1981). MK polyploidization is thus inhibited on stiff matrix where increased adhesion maximizes the traction forces for cell division even when MII is inhibited (Shin et al., 2011). Conversely, cell cycle progression can also be inhibited by soft matrix for at least some adherent cells (Klein et al., 2009). Adhesion, matrix elasticity, and external forces thus couple MII in processes central to hematopoietic fates such as cell division (symmetric or asymmetric) and platelet generation.

1.5 MEMBRANE EXPRESSION OF CD47 PROTECTS CELLS FROM PHAGOCYTOSIS BY MACROPHAGES AND IS UPREGULATED IN CANCER

CD47 is a cell surface molecule that binds several proteins including integrins (Brown and Frazier, 2001) and thrombospondin-1 (Lindberg et al., 1996), and has been shown to play roles in physiologic process including cell migration (Jaiswal et al., 2009; Lindberg et al., 1996; Liu et al., 2001), T-cell and dendritic cell activation (Sarfati et al., 2008), and axon development (Miyashita et al., 2004). Additionally, CD47 functions as an inhibitor of phagocytosis through association with SIRPα expressed on phagocytes. This interaction leads to tyrosine phosphatase activation and inhibition of MII accumulation at the phagocytic synapse (Tsai and Discher, 2008). In this role, CD47 acts as a "don't eat me signal" and a marker of self, as loss of CD47 leads to homeostatic phagocytosis of aged or damaged cells (Blazar et al., 2001; Gardai et al., 2005; Oldenborg, 2000). CD47 is widely expressed on a majority of normal tissues (Reinhold et

al., 1995), which suggests that its role in regulating phagocytosis is widespread. While expression is ubiquitous on normal cells, multiple tumor types have been shown to express increased levels of CD47 (Chao et al., 2010a, 2011a; Jaiswal et al., 2009; Majeti et al., 2009). A study in which a CD47-deficient myeloid leukemia cell line was forced to overexpress CD47 facilitated aggressive dissemination and fulminant death in xenograft mice, in contrast to minimal engraftment upon transplantation of the CD47-deficient cells (Jaiswal et al., 2009). Upregulation of CD47 expression in human cancers also appears to influence tumor growth and dissemination. Expression of CD47 in several hematologic malignancies was found to be associated with a worse clinical prognosis, and was able to predict refractoriness to standard chemotherapies in acute lymphoblastic leukemia (ALL) (Chao et al., 2010a, 2011a; Majeti et al., 2009). Conversely, shRNA knockdown of CD47 in human non-Hodgkin's lymphoma (NHL) led to a dramatic decrease in hematogenous dissemination and spread to major organs compared to control NHL cells (Chao et al., 2011b). Such findings support a hypothesis of cancer progression in that overexpression of CD47 enables tumors to escape innate immune system surveillance through evasion of phagocytosis.

Targeting the CD47-SIRPα pathway has currently been an active area of research. Treatment with an anti-CD47 antibody has proven efficacious in mouse models of acute myeloid leukemia (AML), ALL (Chao et al., 2011a; Majeti et al., 2009), NHL (Chao et al., 2010a), multiple myeloma (MM) (Kikuchi et al., 2005), bladder cancer (Chan et al., 2009), and breast cancer (Manna and Frazier, 2004). While anti-CD47 antibodies disrupt the CD47-SIRPα interaction on tumor cells, these antibodies likewise can bind to CD47 on normal tissue. However, administration of anti-CD47 antibodies did not result in

severe off-target toxicity (Majeti et al., 2009). This paradox can be resolved if in addition to blocking the anti-phagocytic an additional pro-phagocytic stimulus is required for tumor clearance. Indeed, it has been shown that many hematologic and sold tumors express the pro-phagocytic signal calreticulin (CRT) on their cell surface while normal cells did not (Chao et al., 2010b).

Expanding on the simple therapies targeting only CD47, recent studies have combined CD47-SIRPα blocking with tumor-targeting antibodies to maximize efficacy. The primary role of tumor-targeted antibody is to stimulate Fc-mediated functions such as antibody-dependent cellular cytotoxicity (ADCC) and FcR-mediated phagocytosis to augment tumor cell killing. This method stimulates phagocytosis by blocking a negative signal and delivering a positive signal. Such treatments have been leveraged in preclinical models of NHL using anti-CD47 and the anti-CD20 antibody rituximab leading to synergistic elimination of xenografts in mice (Chao et al., 2010a). In another context, anti-SIRPα antibody plus the anti-Her2/Neu antibody trastuzumab potentiated ADCC of breast cancer cells. Co-administration of macrophage stimulating cytokines, M-CSF and GM-CSF, has shown to enhance anti-tumor activity against multiple tumor types (Hernandez-Ilizaliturri et al., 2005; Sanda et al., 1992; Stockmeyer et al., 1997; Valerius et al., 1993). Concurrent administration of chemo-radiation therapy with anti-CD47 is yet another combination strategy that may prove successful. A treatment regimen consisting of chemo-radiation prior to anti-CD47 may lead to increased macrophages effector cells, as chemotherapy can induce an inflammatory response that attracts infiltrating macrophages to tumor sites (Funada et al., 2003; Le et al., 2007; Welsh et al., 2005). Prior studies have shown that chemo-radiation leads to increased expression of CRT on

tumor cell surfaces (Obeid et al., 2007) thus potentially augmenting the efficacy of anti-CD47 antibody treatment. The many ways that CD47-SIRPα blocking could lead to an efficacious treatment of a variety of cancers with minimal side effects motivates the further investigation of the mechanisms behind such ADCC.

1.6 MOTIVATION AND OUTLINE OF THESIS

Investigation of hematopoiesis has primarily focused on soluble factors (Metcalf, 2008), surface antigens (Weissman and Shizuru, 2008), and genetic studies of cell cycle components (Orford and Scadden, 2008) and transcription factors (Novershtern et al., 2011). Only recently have researchers began to understand the role of the niche in stem cell maintenance and differentiation. Yet, the roles of cytoskeletal and nuclear membrane mechanics and accompanying forces in hematopoiesis have been grossly under investigated. Due to the high nucleus-to-cytoplasm ratio of hematopoietic cells it seems reasonable to envision that processes such as partitioning between marrow and blood could be, at least partially, dependent on nuclear deformability and that deformability is modulated by lamin-A and –B.

Asymmetric division of stem cells is known to be established by polarization of MII (Ou et al., 2010). MIIA is found in most tissues (Ma et al., 2010) including blood (Maupin et al., 1994) and is essential to embryonic development (Conti et al., 2004). Meanwhile, MIIB is more polarizable, particularly during cell migration, (Raab et al., 2012; Vicente-Manzanares et al., 2008) and recent studies have demonstrated roles in MK differentiation (Lordier et al., 2012) and asymmetric erythroid enucleation (Ubukawa et al., 2012). Thus, it is plausible that specific MII isoforms play unique roles in

hematopoiesis. We demonstrate critical roles for MIIA and MIIB in adult hematopoiesis and use that understanding to enrich highly heterogeneous HSC/Ps for long-term hematopoietic stem cells.

After the investigation of lamin and MII in early hematopoiesis, focus is shifted to MII in the terminal stages of platelet production. Intravital imaging of mouse bone marrow has captured the process of proplatelet fragmentation from MKs (Junt et al., 2007) while others have demonstrated that MIIA activity inhibited by blebbistatin results in an increase in proplatelet extension length (Chen et al., 2007; Eckly et al., 2010). Individuals with genetic mutations of *MYH9* encoding MIIA show macro-thrombocytopenia (Balduini et al., 2011). Recent work has provided additional insight into the further processing of sheared proplatelets to smaller platelets, but was chiefly focused on microtubules yet likened the process to cytokinesis, which is driven by MIIA activity (Thon et al., 2010). Together these findings seem to indicate that precise control of MIIA activity is critical to proper proplatelet extension, fragmentation, and processing in order to maintain proper platelet size and number.

To address the issues of early hematopoiesis, we employ either siRNA or shRNA knockdown or overexpression of lamin-A, -B, MIIA, or MIIB to explore roles of individual isoforms or stoichiometric effects in $CD34^+$ cells. Cells are then assayed by means of micropipette aspiration or colony forming assay *in vitro* and primary, secondary, or competitive xenotransplantation *in vivo* using mice. The role of MIIA in platelet generation and fragmentation is addressed by cone and plate rheometry and micropipette aspiration either with or without blebbistatin. Mutagenesis approaches are used to further explore MIIA phosphorylation as well as known *MYH9*-RD mutations.

All or which leads to imaging and characterization of *MYH9*-RD patient platelets and a comparison with platelets from normal donors in the presence or absence of blebbistatin.

The thesis then shifts from membrane determinants of hematopoiesis to harnessing the membrane recognition and phagocytic capacity of macrophages to treat cancer. The Discher lab has already shown that CD47 expression attenuates phagocytosis, particularly that phagocytosis of beads opsonized with a peptide engineered from CD47 is decreased (Rodriguez et al., 2013). Others have shown dramatic tumor shrinking results using an engineered SIRPα variant in combination with a monoclonal anti-cancer antibody (Weiskopf et al., 2013), while others have demonstrated increased efficacy of rituximab with co-administration of anti-CD47 antibody (Chao et al., 2010a).

We use a NSG mouse model to generate human xenograft tumors of either normal or near complete knockdown of CD47. Tumor progression is monitored throughout the studies by live animal fluorescence imaging. Mice are treated with a human specific polyclonal antibody and tumors, spleen, and blood are collected at the termination of treatment. These tissues are then analyzed by flow cytometry to assess CD47 levels, macrophage number and maturity as well as antibody opsonization and macrophage phagocytosis of human material. Anemia and thrombocytopenia are assessed from the blood collection. Furthermore, a GFP expressing cell line of normal CD47 expression was generated and spiked into CD47 knockdown tumors to determine which, if any, cell type was preferentially eliminated.

The chapters of this thesis are organized to address early hematopoiesis, specifically the roles of lamins and myosins, in Chapter 2 including an exploration into

the roles of myosins in HSC/P self-renewal, which leads to an *in vivo* demonstration of how perturbation of MII effects hematopoietic reconstitution and long-term engraftment. Chapter 3 explores the role of MIIA in fragmentation of proplatelets from MKs and further preplatelet fission to normal size and number platelets. This work includes a direct comparison of normal platelets with those obtained from *MYH9*-RD patient PB. The role of CD47 attenuation in cancer treatment is presented in Chapter 4. An *In vivo* solid tumor xenograft model provides mechanistic insight into the clearance of tumor cells following antibody treatment. Finally, Chapter 5 summarizes the conclusions of the prior three chapters and presents future directions, some of which are currently in progress. In all, this work highlights biophysical factors of cortical and nuclear membranes that govern hematopoietic differentiation and trafficking, normal and pathological thrombopoiesis, and provides a mechanism of phagocytic clearance of cancer cells through CD47 attenuation and species specific but epitope non-specific antibody infusion to stimulate macrophages.

CHAPTER 2: CORTICAL AND NUCLEAR MECHANICS MODULATE DIFFERENTIATION AND THEIR DETERMINANTS ARE LINEAGE SPECIFIC

The work presented in this chapter is a combination of novel contributions to the following articles appearing in publication and used with permission of the senior author.

Myosin-II inhibition and soft 2D matrix maximize multinucleation and cellular projections typical of platelet-producing megakaryocytes. Shin JW, Spinler KR, Discher DE, et al. PNAS. 108:11458-11463. (2011)

Lamins regulate cell trafficking and lineage maturation of adult human hematopoietic cells. Shin JW, Spinler KR, Discher DE, et al., PNAS. 110:18892-18897. (2013)

Nuclear lamin-A scales with tissue stiffness and enhances matrix-directed differentiation. Swift J, Spinler KR, Discher DE, et al., Science. 341:124014. (2013)

Contractile forces sustain and polarize hematopoiesis from stem and progenitor cells. Shin JW, Spinler KR, Discher DE, et al., Cell Stem Cell. 14:81-93. (2014)

ABSTRACT

Adult marrow niches provide the residence of hematopoietic stem and progenitor cell, as well as nucleated erythroblasts and megakaryocytes while other blood cells easily cross through endothelial sinusoids into the circulation. Due to the high nuclear to cytoplasm ratio in hematopoietic cells, we propose that cells cross microporous barriers preferentially due to regulation of nuclear deformability controlled by lamin-A and –B and that lamin levels can directly modulate hematopoietic programs. Using micropipette aspiration we demonstrate that nuclear flexibility is limited by lamin-A:B stoichiometry across hematopoietic lineages. Furthermore, differentiation is altered by disrupting the A:B ratio by overexpression or knockdown of either lamin-A or –B. We also show that high A:B promotes erythroid differentiation while high ploidy megakaryocytes are inhibited by lamin suppression. Thus, lamins contribute to differentiation and trafficking. Whereas lamins confer nuclear mechanical properties, nonmuscle MII acts at the cell cortex. Self-renewal and differentiation of stem cells rely on asymmetric division and polarized motility that is modulated by MII forces and matrix mechanics in other cell types. Here, we show *in vivo* that MIIB is required for generation of blood, while MIIA is required for long-term HSC/P engraftment. Reversible pharmacological inhibition of either MIIA or MIIB with blebbistatin *in vitro* enriches for long-term hematopoietic multilineage reconstituting cells by at least 5-fold as assessed *in vivo*. Additionally, megakaryocytes become more polyploid and produce 4-fold more platelets. These results implicate MII as a multifunctional node in polarized division and niche sensing. We conclude by taking a larger scale look at the relationship between stress and bulk tissue stiffness, which reveals that matrix stiffness directly feeds back to adjust lamin-A at the

protein level. Particularly, in the context of high stiffness/stress, lamin-A levels increase to stabilize the nucleus.

2.I PREFACE

The author of this thesis contributed towards the following specific experiments and figures (organized by publication):

Myosin-II inhibition and soft 2D matrix maximize multinucleation and cellular projections typical of platelet-producing megakaryocytes. Shin JW, Spinler KR, Discher DE, et al. PNAS. 108:11458-11463. (2011)

- All micropipette aspiration studies leading to generation of **Figure 2.1** and accompanying text

Lamins regulate cell trafficking and lineage maturation of adult human hematopoietic cells. Shin JW, Spinler KR, Discher DE, et al., PNAS. 110:18892-18897. (2013)

- All micropipette studies in **Figure 2.2**
- Lamin-A and –B transfections and transductions for **Figure 2.2 and 2.3**
- Culture of HSCs, colony forming assays, and flow cytometry for **Figure 2.3**
- Micropipette aspiration and lamin-B transduction for **Figure 2.S1**
- Transfection and transduction of lamin-A and –B, flow cytometry and colony forming assay for **Figure 2.S2**

Contractile forces sustain and polarize hematopoiesis from stem and progenitor cells. Shin JW, Spinler KR, Discher DE, et al., Cell Stem Cell. 14:81-93. (2014)

- MIIB transduction, colony forming assays, and flow cytometery for **Figure 2.4**
- Micropipette aspiration for **Figure 2.5**
- Cell culture, MIIB transduction, animal husbandry, blood sampling, and flow cytometry of bone marrow and peripheral blood for **Figure 2.6A, B**
- Tamoxifen administration, animal husbandry, blood sampling, and flow cytometry of bone marrow and peripheral blood for **Figure 2.6D-G**
- Xentransplants, bone marrow harvest and flow cytometry for **Figure 2.7B**
- MIIA transduction for **Figure 2.S3**
- Flow cytometry and colony forming assay for **Figure 2.S4**

Nuclear lamin-A scales with tissue stiffness and enhances matrix-directed differentiation. Swift J, Spinler KR, Dischер DE, et al., Science. 341:124014. (2013)

- Micropipette aspiration of tumor tissue for **Figure 2.8C**

2.1 INTRODUCTION

In theory, mechanical properties of a given tissue should relate to the physical stress exerted on said tissue. The dissipative capacity of soft brain and fat may explain why these tissues are soft compared to the rigidness characteristic of adult bone necessary to endure ambulatory stresses. This stress and tissue feedback has been proposed to be a "mechanostat" (Frost, 1987). More granularly, cells are deformed by physical stress (Vogel and Sheetz, 2006) that can alter gene expression (Chen et al., 2001), yet until recently it was unknown whether any specific proteins are capable of matching stiffness with stress and determining differentiation (Swift et al., 2013). Animal cells cultured on gels or elastomeric substrates have shown to effect differentiation (Engler et al., 2006) and cell shape and motility (Pelham and Wang, 1997). Gels designed to match the stiffness of brain or fat maximize neurogenesis or adipogenesis, respectively (Dupont et al., 2011; Georges et al., 2006; Ulrich et al., 2009). Further, stiffer gels favor myogenesis (Engler et al., 2004, 2008; Gilbert et al., 2010) and hard gels give rise to osteogenesis (Engler et al., 2006; Huebsch et al., 2010; Kong et al., 2005). Collagen and cytoskeletal proteins contribute to sustain forces imparted on cells and within cells proportionally to the surrounding tissue microelasticity (Discher et al., 2005; Engler et al., 2006). These forces propagate into the nucleus where they are resisted by the nuclear lamina. Nuclear stiffness (Lammerding et al., 2006; Pajerowski et al., 2007) and stability (De Vos et al., 2011) is maintained in part by intermediate filaments known as lamins. In addition to conferring mechanical strength to the nucleus, lamins may also modulate transcription (Shimi et al., 2008) and thus may mechanoregulate the genome (Shivashankar, 2011; Wang et al., 2009).

In addition to providing a link between bulk tissue stiffness and stress, lamins may also provide an integral role in hematopoiesis. Hematopoietic cells must traverse the marrow, squeeze through small sinusoids, and enter the blood (Sabin, 1928). Therefore, cell deformability seems to be a potential regulator of both retention and egress of HSC from the marrow niche. Indeed, human polymorphonuclear neutrophils (PMNs) were shown decades ago to become more deformable upon differentiation in the marrow (Lichtman, 1970), with mature PMNs more capable of entering and exiting small capillaries (Lichtman et al., 1989). Leukemic cells are more rigid than normal, potentially explaining the interrupted blood flow and marrow hypercellularity in disease (Lam et al., 2007). Normal hematopoiesis has a well-characterized hierarchy, but it is unclear whether deformability factors into the program (Lichtman et al., 1989). Importantly, because of the high nucleus-to-cytoplasm ratio of hematopoietic cells, key processes such as sorting between marrow and blood could be based in part on nuclear deformability.

Lamins are intermediate filament proteins that assemble into "lamina" networks at the interface between chromatin and the inner nuclear membrane (Dechat et al., 2010), conferring stiffness to the nucleus (Pajerowski et al., 2007). In addition, the lamina is often proximal to heterochromatin, and, at least with embryonic stem cells, some genes alter their interactions with the lamina during cell-fate determination (Peric-Hupkes et al., 2010). Nearly all mammalian cells express A-type and B-type lamins. Early work reported conflicting results of either decreased levels (Gerner and Sauermann, 1999; Olins et al., 2008; Röber et al., 1990) or increased levels (Guilly et al., 1990) of both lamin types even within the same cell type. One dramatic mutation in human LMNA leads to the accelerated aging syndrome Progeria (Dechat et al., 2010), in which protein

accumulates at the nuclear envelope and stiffens it (Dahl et al., 2006), affecting many tissues and increasing platelet numbers by two- fold or more (Merideth et al., 2008). Mice with deletion of *Lmna* survive 6 weeks postnatal (Jahn et al., 2012), despite defective lymphocytes (Hale et al., 2010). Mice deficient in lamina-associated polypeptide 2α show hyperproliferation of erythroid progenitors and impaired differentiation (Naetar et al., 2008). Mutations of B-type lamins are less common but have been shown to result in defective chemotaxis, and elevated lamin-A (Zwerger et al., 2008). Direct roles for lamins in normal human hematopoiesis, trafficking, and rheology have remained elusive until our recent work (Shin et al., 2013). High nuclear flexibility coordinate with low lamin levels may facilitate migration of nucleated cells through constraining pores. Conversely, egress of enucleated reticulocytes may be the result of non-permissive nuclear trafficking due to nuclear stiffening following nuclear condensation of erythroid progenitors. Megakaryocyte maturation results in polyploidization resulting in large nuclei unable to pass through pores effectively anchoring the MK. Anchorage is thought to allow extension of membrane projections into the blood where they are fragmented by blood shear stresses which ultimately produce platelets (Junt et al., 2007).

While trafficking of terminally differentiated hematopoietic lineages is necessary for their function, stem cells must be able to both self-renew and undergo asymmetric division in appropriate microenvironments (Knoblich, 2010). This differential segregation of cell fate determinants produces progenitors that expand symmetrically to generate tissue. Hematopoietic stem cells (HSCs, as a subset of $CD34^+$ cells) exemplify these key properties of stem cells in that they are often quiescent in niches of the bone

marrow (BM), but they and/or their daughter cells polarize and divide asymmetrically in suitable niches to generate progenitors that further divide and specialize to terminally differentiated erythroid, MK, and white cell lineages. Many soluble factors regulating HSC maintenance and differentiation have been described (Trumpp et al., 2010), but physical aspects of hematopoiesis remain unclear. Myosin-II inhibition has been found to play a key role in the actomyosin forces imparting adhesion and matrix sensing in matrix modulated expansion of adult HSC/Ps (Holst et al., 2010). MII in the cell cortex is also known to drive cytokinesis and asymmetry of stem cell division in *C. elegens* is established by MII (Ou et al., 2010). Differentiation in embryogenesis indeed requires active MII (Conti et al., 2004), and while inhibition of MII in adherent embryonic stem cells (ESCs) increases survival in culture by preserving intercellular contacts (Chen et al., 2010), inhibition can also lead to multinucleated cells (Canman et al., 2003). Actomyosin forces stabilize the plasma membrane with an active cortical tension (Merkel et al., 2000), but these forces can drive cell rounding in cytokinesis (Sedzinski et al., 2011) and can be dramatically altered in MSC differentiation (Engler et al., 2006). It has long been established that differentiated granulocytes soften to facilitate trafficking though the marrow (Lichtman, 1970), but until recently it has been unknown whether such processes are accompanied by changes in MII.

There are three isoforms of mammalian MII: A (*MYH9*), B (*MYH10*), and C (*MYH14*), each of which is regulated transcriptionally and posttranslationally. MIIA is found in most tissues (Ma et al., 2010) including blood (Maupin et al., 1994) and is essential to embryonic differentiation (Conti et al., 2004). MIIB is more highly polarized that MIIA, and can be found at the rear of migrating cells (Raab et al., 2012; Vicente-

Manzanares et al., 2008). Additionally, MIIB has been shown to be important for MK differentiation (Lordier et al., 2012) and erythroid enucleation (Ubukawa et al., 2012), but functions in stem cells is generally unknown. We begin our journey through the mechanosensitive properties of hematopoiesis and stress sensing with an investigation of HSC stiffness before transitioning into the lamins and the cell nucleus, moving outward to the cell cortex to reveal roles for MIIA and MIIB in adult hematopoiesis and finish with an investigation of how mechanical properties of the extracellular matrix can impact lamin expression.

2.2 MATERIALS AND METHODS

Cell Culture

Fresh purified bone marrow-derived human $CD34^+$ cells and total mononuclear cells were obtained from either the Penn Xenograft Core Facility or AllCells (Emeryville, CA). Cells from at least five different donors were used in this study. Purity of the samples (>98%) was confirmed by flow cytometry with mono- clonal antibody against human CD34. All experiments with primary cells were performed in primary hematopoietic media (StemLine-II; Sigma) supplemented with 1x antibiotics and the following human recombinant cytokines: stem cell factor (SCF; 100 ng/mL) and Tpo (100 ng/mL). In some occasions, the media were also supplemented by fetal bovine serum (FBS) [10% (vol/vol)], dexamethasone (Sigma; 1 μM), 17β-estradiol (Sigma; 1 μM), granulocyte-colony stimulating factor (G-CSF; 10 ng/mL), Epo (1 U/mL), and interleukin-3 (IL-3, 10 ng/ mL). All cytokines were purchased from R&D Systems. In some cases, after cells were cultured for 4 days, they were treated with different doses of cellular contractility inhibitors, including (±)-blebbistatin (EMD Biosciences) for indicated durations of up to 3 days. MEG01 and COS-1 cells were cultured in RPMI-1640 and DMEM, respectively, supplemented with 10% FBS and 1% antibiotics. Cells were cultured at 37°C in 5% CO_2.

Antibody staining and flow cytometry

Surface marker analysis for HSC/Ps was done on either a LSR II flow cytometer or FACSCalibur (Becton Dickinson). Fresh or cultured $CD34^+$ - derived cells were stained in staining media (2% FBS in PBS) at room temperature for 1 hour (hr) with PE or APC-

Cy7 anti-CD34 (581, Invitrogen or Biolegend), PE-Cy7 anti-CD38 (HIT2, eBioscience), PECy5.5 anti-CD45RA (MEM-56, Invitrogen), APC anti-CD90 (5E10, BD Bioscience), washed and stained with Hoechst 33342 (Invitrogen) at 37°C for 30 minutes to stain nuclei, followed by washing with staining media with 7-AAD (Sigma) to exclude dead cells. Cells isolated from the bone marrow stained for 1 hr with APC anti-mouse CD47 (miap301, AbD Serotec), FITC anti-human CD47 (BD Biosciences), and PE anti-human CD11b, PE anti-human CD19 (both from BD Biosciences), or PE anti-human Glycophorin A (Invitrogen). Platelets and Mks were analyzed by staining with PE anti-mouse CD41 (eBioscience) and FITC anti-human CD41 (eBioscience) for 20 minutes (min), followed by analysis on FACSCalibur on log forward and side scatter scales.

CFSE labeling

$CD34^{+}$-derived cells were labeled with CFSE (2.5 μM) in PBS/5% FBS for 3 min in dark at room temperature and washed once with PBS/5% FBS and once with HSC expansion media. The labeled cells were analyzed every day (d) for 3 days using multi-color flow cytometry with HSC/P markers. Given that cell division is unsynchronized, cell numbers from different CFSE peaks are normalized by dividing the cell numbers by division number to correct for the effect of cell expansion. The mean division number from each sample was calculated by fitting normalized CFSE data to the normal distribution curve and reporting its mean value. The cell decay rate was calculated as described previously (Gett and Hodgkin, 2000): Each peak represents a cohort of cells that entered their first division at the same time, and so one can calculate how many cells of each type

underwent each division with the decay in cell number versus division number reflecting proliferation, differentiation, and cell death.

Electroporation of nucleic acid in cell culture

Primary $CD34^+$ cell culture and MEG01 cell line were transfected with DNA constructs or MIIB siRNA by electroporation ("nucleofection") using the Nucleofector kits (Lonza) as described in the manual. Briefly, cultured cells were washed with PBS and resuspended with transfection solution containing 2 μg/mL DNA constructs or 3 μg/mL siRNA. They were then transferred into a cuvette and transfected with the Nucleofector II. The medium at 37℃ was then added to transfected cells. Cells were incubated overnight and then the medium was exchanged to fresh on the next day.

The siRNA sequences used for MIIB and MIIB knockdown are described previously (Raab et al., 2012; Shin et al., 2011).

To silence the expression of lamin-B1, the retrovirus vector constructs containing shRNA were obtained from the laboratory of Robert Goldman (Northwestern University, Chicago) and prepared as described previously (P1). pSilencer constructs containing either scrambled or lamin-B1 shRNA sequences were transfected into HEK-293T cells, and virus-containing culture supernatants were collected at 24~48 h following transfection in serum-free hematopoietic media. The culture supernatants containing virus were then incubated with $CD34^+$-derived cells for shRNA transduction in the presence of 5 μg/mL polybrene (Sigma) and incubated for 1 d. Virally transduced cells were selected by adding 1 μg/mL puromycin (Invitrogen) for 2 d and incubated in fresh medium for at

least 1 d before further analyses. Lamin-A was also down-regulated stably in a similar manner as lamin-B1 with human lamin-A shRNA (Sigma).

For lamin-A promoter assays, we used a GFP construct driven by the human lamin-A promoter cloned by Genecopoeia. The promoter was derived from the 1,132-base pair upstream region and the first 385-base pair mRNA transcript region. Promoter activity was characterized with or without retinoic acid after transient transfection using LF2k (Invitrogen) per the manufacturer's instructions.

Cell sorting

BM $CD34^+$-derived cells at d 7 were stained with CD41-FITC at room temperature for 1 hr, followed by with Annexin-V-PE (BD Biosciences) in the Annexin-V staining medium for 15min. Cells were then resuspended in 2% FBS/PBS with 7-AAD. Viable HSC/Ps and differentiated cells at d 7 culture were separated on the basis of CD34 surface expression by cell sorting performed on a FACS VantageTM machine (Becton Dickinson). Dead cells stained with 7-AAD and Annexin-V were excluded from sorting. Sorted cells were directly processed for microarray analysis.

Colony forming assay

1000-3000 $CD34^+$-derived cells were seeded into methylcellulose containing media (MethoCult H4434, StemCell Technologies) supplemented with SCF, GM-CSF, IL-3, Epo. They were cultured for 14 days and colonies were scored at 10x magnification based on the published morphological criteria by StemCell Technoloigies. Colony forming content was normalized per 10,000 cells seeded.

Engraftment of CD34$^+$ cells in NSG mice and limiting dilution analysis

BM-derived CD34$^+$ cells were cultured in SCF and Tpo (100 ng/ml each) for 4 days and treated under control conditions or blebbistatin (20 μM) for 3 days. The cells were injected intra-tibially into sublethally irradiated (250 rads) 6-10-week-old NSG mice within 24 hours after irradiation. Engraftment was assessed by analysis of blood or bone marrow using anti-mouse and anti-human CD47 antibodies using flow cytometry. The mice were sacrificed after 16 weeks post-transplantation. For secondary engraftment, 50% of the bone marrow from femurs and tibias from each mouse was transplanted into one sublethally irradiated NSG mouse. 16 weeks after transplantation, blood and bone marrow were harvested from the mice and analyzed by flow cytometry. All animal experiments were done in accordance with institutional guidelines approved by the ethical committee from the University of Pennsylvania. The human repopulation HSC frequency was quantified by extreme limiting dilution analysis (ELDA) software (Hu and Smyth, 2009).

Lentiviral transduction of CD34$^+$ cells

For MIIB knockdown experiment, fresh human BM CD34$^+$ cells were transduced with lentiviral vector containing MIIB shRNA sequence previously verified (pLKO.1-puro, Sigma):

5’CCGGGCCAACATTGAAACATACCTTCTCGAGAAGGTATGTTTCAATGTTGG CTTTTTG-3’

Transduction was done on plate coated with 100 ng/ml retronectin (Lonza) in the presence of 5 μg/mL polybrene (Sigma). After 2 days of transduction, untransduced cells were selected by adding 1 μg/mL puromycin for 2 days, followed by transplantation.

Inducible knockout mice, transplantation and engraftment

Cre;MYH9loxP/loxP mice were produced by the laboratory of Catherine Léon and Christian Gachet (Université de Strasbourg) and provided by the laboratory of Christopher Hunter (University of Pennsylvania). 8-12 week-old gender-matched mice were used. For competitive repopulation, a total of 2 million donor BM cells from Cre;MYH9loxP/loxP (CD45.2) and genetically matched WT mice (CD45.1) were mixed 1:1 and injected retro-orbitally into the lethally irradiated recipient WT mice (B6.SJL, $CD45.1^{+}$). 8 weeks later, 20 mg/mL tamoxifen in sterilized corn oil (both from Sigma) was administered into the recipient mice 5 times for one week to induce *Myh9* deletion. Chimerism was determined by flow cytometry analysis on PB at indicated time points, and the mice were sacrificed after 8 weeks of *Myh9* deletion to perform BM and SP analysis.

Micropipette aspiration

Capillary tubes of 1.0 mm inner diameter (World Precision Instruments, Sarasota, FL) were pulled into micropipettes using a Flaming-Brown Micropipette Puller (Sutter Instrument, Novato, CA) and cut further using a deFonbrune-type microforge (Vibratome, St. Louis, MO). The average micropipette diameter was around 3 μm. Micropipettes were attached to a dual-stage water manometer with reservoirs of

adjustable height. Suction was applied by a syringe, and the corresponding pressure was measured by pressure transducer (Validyne, Northridge, CA) calibrated by a mercury U-tube manometer. Images were acquired using a Nikon Eclipse TE300 inverted microscope using a 20x or 40x objective and a Cascade CCD camera (Roper Scientific).

For experiments from Shin, et al., PNAS 2011, cells from BM $CD34^+$ cultures in SCF and Tpo between 3 and 8 days were treated with 20 μM Bleb for 30 min-1 hr, followed by micropipette analysis. Pressures for different experiments ranged from 0.5 to 20 kPa. In some cases, cells were labeled with a very low dose (10 nM) of fluorescent BODIPY-Taxol (Invitrogen) for 1 hr at 37°C to visualize the initial stage of microtubule polymerization during micropipette aspiration.

For experiments from Shin, et al., PNAS 2013, primary cells or cell lines in suspension were subjected to micropipette analysis. Pressures for different experiments ranged from 0.5 to 15 kPa.

For experiments from Swift, et al., Science 2013, the average micropipette diameter was around 15 μm. For untreated samples from mice, tissue was immediately aspirated. Collagenase treated samples were incubated at 37°C for 10 minutes in the presence of 0.1 mg/mL collagenase (Sigma) and aspirated in the presence of enzyme. Pressures for different experiments ranged from 1 to 20 kPa. For aspiration of nuclei, cells were treated with 0.2 μg/mL Latrunculin A (Sigma) for 1 hr at 37°C, detached with trypsin/EDTA, centrifuged and resuspended in aspiration buffer of 135 mM NaCl, 5mM KCl, 5 mM HEPES, 1.8 mM $CaCl_2$, 2 mM $MgCl_2$, 2% BSA, 1:3000 propidium iodide (Molecular Probes). Nuclei were stained with Hoechst 33342 (Molecular Probes). Images were capture using a 60x oil objective.

For experiments from Shin, et al., Cell Stem Cell 2014, fresh BM $CD34^+$ cells or transfected COS-1 cells in suspension were subjected to micropipette analysis. Pressures for different experiments ranged from 0.5 to 15 kPa.

2.3 RESULTS

Myosin-II inhibition increases MK membrane fragmentability – (*PNAS*, 2011)

To investigate the role of MII in membrane integrity under shear, cells were subjected to micropipette aspiration with stepwise decreases in pressure using pipettes similar in diameter to human capillaries (~3 μm). The cell and its membrane shear and flow into the micropipette, resembling, in shape, elongated proplatelets. After just 30 min of blebbistatin, cells are approximately four-fold more compliant (Fig. 2.1A, right and Fig. 2.1B), and 40% of treated cells also rapidly fragment to average sizes similar to those of large human platelets (3~4 μm). Platelets are now known to be generated by shearing of proplatelets (Thon et al., 2010), and no fragmentation was observed in untreated cells. Projection lengths up to the point of divergent fragmentation vary from 10~20 μm, which is similar to *in vivo* fragmented proplatelet lengths of ~14 μm (Junt et al., 2007). Fragmentation stresses here correspond to effective membrane tensions of ~1 mN/m, which is 10-fold lower than cell membrane lysis tensions (Hategan et al., 2003). Platelets not only maintain membrane integrity but also exhibit characteristic structures, such as cortical, coil-like microtubules (MTs), and so we also aspirated primary MKs and MEG01 cells (an MK-like line) after labeling with a very low and cell-viable dose of fluorescent-Taxol (10 nM) (Guminski et al., 2001). Even at a 1,000-fold higher dose of Taxol, proplatelets are known to extend (Italiano et al., 1999). In slow aspirations here, MT-coils could be visualized extending into the projection tips at ~0.7 μm/min (Fig. 2.1C) and bundles of MTs appear more likely than individual MTs, all consistent previously reported rates and structures (Italiano et al., 1999). Although final structures are rate- and force-dependent as transition rates ~ exp(force) (Hategan et al., 2003), the

basic findings here indicate both nonlytic fragmentation under shear and MK polyploidization could be promoted in part by MII inhibition, even with microtubule polymerization as reported (Italiano et al., 1999).

Lamin A regulates trafficking and lineage maturation – (*PNAS* 2013)

Transendothelial migration involves large deformation as nucleated cells pass through much smaller pores (Lichtman et al., 1989). Aspiration of a cell into a micropipette illustrates the requisite nuclear deformation (e.g., G/M cells, Fig. 2.2A). Our group's previous aspiration experiments on a lung epithelial cell line showed that disruption of the cytoskeleton with or without lamin knockdown can reveal the contribution of lamins to nuclear properties (Pajerowski et al., 2007). This previous study prompted a similar approach here, but with care to use low stresses commensurate with those generated by cells during migration (Oakes et al., 2009). With G/M cells, lamin-A knockdown by ~50% (Fig. 2.2A) indeed softens the nucleus ~two-fold (Fig. 2.2A). Further experiments using transwell migration showed an increase in trafficking for lamin-A knockdown cells at small pore area (Shin et al., 2013).

Lamin Isoform Stoichiometry Predicts Nuclear Rheology – (*PNAS* 2013)

Of the many studies of hematopoietic cell deformability (e.g., Lichtman 1970), nuclear deformability has not yet been directly characterized and compared across lineages. Our group has shown that fresh human $CD34^{+}$ cells are highly deformable compared with solid-tissue cell types (Pajerowski et al., 2007), perhaps indicative of the stem cell/progenitor's ability to traffic between marrow and circulation. The progressive

increase in aspirated length of a nucleus at a constant pressure (Fig. 2.2B) gives the nuclear compliance and often fits a power law $J(t) = a \cdot t^b$ that is typical for polymer rheology (Pajerowski et al., 2007). The initial compliance is given by a, whereas b = 1 indicates a simple fluid that flows and does not recover after release of stress, and b = 0 indicates a simple elastic solid that will fully recover its shape. Lymphoid and myeloid nuclei show high initial compliance ($a = 20\ kPa^{-1}$) (Fig. 2.2B), as predicted from their low lamin levels and are roughly similar in this respect to fresh $CD34^+$ cells (Pajerowski et al., 2007). T-cell nuclei are also more viscous (b = 0.22) than myeloid nuclei (b = 0.08) (Fig. 2.2B), consistent with a previous report that granulocytes do not permanently deform as they pass through marrow (Lichtman et al., 1989). In contrast, erythroid (Ery) progenitors generally show at least 10-fold lower initial nuclear compliance (Fig. 2.2B). Although ProEry ($CD44^+GPA^-$) nuclei exhibit viscoelastic behavior similar to that of T-cell nuclei, late Ery ($CD44^-GPA^+$) nuclei are completely stiff and solid, consistent with their condensation during terminal differentiation. Megakaryocyte (MK) nuclei also have lower initial compliance than myeloid or lymphoid nuclei. Compared with MK progenitor ($CD34^-CD41^+$) nuclei (with b = 0.47), mature MK ($CD41^+CD42^+$) nuclei have 20-fold higher compliance despite being more solid-like (b = 0.11) (Fig. 2.2B). The large size and complex shape of polyploid MK nuclei, rather than compliance itself, are therefore likely to limit MK traffickability. Consistent with this, lamin-A:B stoichiometry correlates strongly with local nuclear stiffness [reciprocal of compliance, 1/J(t), in Fig. 3B] measured at different time points (Fig. 2.S1C), which is not the case for A+B intensity (Fig. 2.S1D). Given that B-type lamins localize to the lamina during erythroid differentiation (Krauss et al., 2005) and that nuclear stiffness increases with lamin A:B

(Fig. 2.2C), we hypothesized that down-regulation of B-type lamin(s) would effectively stiffen the nucleus during maturation. Typically, one expects that stiffness correlates positively with protein abundance, and so the prediction here is highly unusual for biopolymer physics. ProEry indeed shows decreased expression of B-type lamins compared with fresh $CD34^+$ cells (Fig. 2.S1B), and nuclear stiffness of ProEry is high compared with circulating nucleated cells (Fig. 2.2C). To directly address the hypothesis, we knocked down lamin-B1, which is expressed at much higher levels than lamin-B2 in hematopoietic cells based on mass spectrometry analyses (data not shown). In erythroid precursors, partial knockdown of lamin-B1 by RNAi (~50%) (Fig. 2.S1E) increases nuclear stiffness (Fig. 2.2D plot shows decreased compliance). Nuclear stiffening after lamin-B1 knock- down was also measured for a U251 glioma cell line in which the lamin-B1 isoform is only slightly more abundant and where knockdown-induced differentiation is unlikely (Fig. 2.S1F). Lamin- B1 down-regulation in erythroid lineages is thus sufficient to promote nuclear stiffening, which is likely to favor marrow retention of a cell (Fig. 2.S1A). A preliminary study using pharmacological perturbations of erythropoietic pathways suggests the association with nuclear rigidification (Fig. 2.S1G).

Lamins Modulate Differentiation: Erythroid Lineage – (*PNAS* 2013*)*

Recent studies of a few primary cells have shown significant modulation of differentiation by lamins. In particular, lamin-A overexpression in marrow-derived MSCs increases osteogenesis (Scaffidi and Misteli, 2008) whereas knockdown promotes adipogenesis (Naito et al., 2012). However, lamin knockout mice develop all tissue types before succumbing at or shortly after birth (Jahn et al., 2012; Kim et al., 2011), and so

most or all tissue lineages seem to develop to some extent, which implies lamins function as lineage maturation factors. Here, we manipulated lamin levels in those hematopoietic lineages with extreme expression, Ery and MK, to assess direct modulation of differentiation (Fig. 2.3A). Overexpression of lamin-A by ~three-fold in $CD34^+$ cells (Fig. 2.S2A) is close to the increased level measured during erythropoiesis (Fig. 2.S1B) and resulted in a significant shift toward blast forming unit-erythroid (BFU-E) from colony forming unit-granulocyte and macrophage (CFU-GM) (Fig. 2.3B), consistent with the map (Fig. 2.S1B). The multipotent CFU-granulocyte erythroid macrophage megakaryocyte (GEMM) was unaffected (Fig. 2.3B). B-type lamins decrease during erythroid development (Krauss et al., 2005; Zermati et al., 2001) (Fig. 2.S1B), and knockdown of lamin-B1 by RNAi in early hematopoietic progenitors indeed favors BFU-E (Fig. 2.3C). In addition, lamin-B1 RNAi decreases CFU-GEMM in contrast to lamin-A overexpression, revealing lamin-B1 as more influential to the maintenance of multipotent progenitors. The results thus show that lamins regulate lineage specification induced by soluble factors.

Lamins Modulate Differentiation: MK Lineage – (*PNAS* 2013)

MKs normally show an increase in total lamin levels (Fig. 2.S1B), but also an increase in A:B ratio. Overexpression of lamin-A indeed increases the number of both early and late MK progenitors cultured from BM $CD34^+$ cells based on surface markers (Fig. 2.3D). Furthermore, although lamin-B1 knockdown suppresses polyploid and 4n populations (Fig. 2.3E), overexpression of lamin-A enhances polyploidy (Fig. 2.S2B). Because Progeria patients reportedly have twofold more platelets in circulation (Merideth et al.,

2008), we also tested the impact of the progerin mutant (Δ50) on MK polyploidy. Overexpression of progerin, which tends to drive lamin accumulation at the envelope (Dahl et al., 2006), does not greatly enhance the number of 8n MKs, but both wild-type and mutant overexpression increase high ploidy (≥16n) MKs (Fig. 2.S2B). The finding here that overexpression of both wild-type and progerin lamin-A gave the same phenotype is consistent with similar findings of increased osteogenesis in MSCs (Scaffidi and Misteli, 2008), suggesting a common mechanism of increased lamina assembly. Phosphorylation of lamin-A promotes disassembly and is high during cell division (Labbaye et al., 1994), and so we hypothesized that an S22A mutant that cannot be phosphorylated would limit nuclear division and again facilitate polyploidization. Overexpression of this mutant indeed shows a greater gain in 8n MKs than WT (Fig. 2.S2B). Overall, the MK results suggest that, whereas lamina regulatory mechanisms might play a role during the formation of early polyploid MKs, the accumulation of lamin-A content per se appears sufficient to drive the formation of late polyploidy MKs through unknown mechanisms.

Lamin-A Modulates Lineage Decisions – (*PNAS* 2013)

Lamin-A knockdown with shRNA (~75% efficiency) (Fig. 2.S2C) was performed to assess fate choices in the presence of a cytokine mixture that promotes multiple lineages (myeloid, erythroid, and MK). In such cultures, knockdown increases the total number of CFU-GM (Fig. 2.3F, Left) but decreases CFU-E and differentiated erythroid lineages without affecting BFU-E or the other differentiated lineages (Fig. 2.3F, Right). Together with the restriction of BFU-E by lamin-B1 (Fig. 2.3C), the results confirm predictions

from the lamin map (Fig. 2.S1B) that lamin-A and B1 play opposite roles in erythroid differentiation.

Asymmetric Division Is Biophysically Regulated by MIIB – (*CSC* 2014)

Large cortical tensions are generated in cells as they round up and divide during asymmetric division (Sedzinski et al., 2011). Because *MYH10* correlates with a half-dozen genes involved in asymmetric division of hematopoietic cells (Ting et al., 2012), confocal imaging and partial knockdown (Fig. 2.4Ai) were used to assess MIIB in asymmetric division of $CD34^+$ cells (Fig. 2.4Aii), which occurs in ~30% of cells (consistent with Lordier et al., 2012). MIIB enriches toward the CD34hi daughter cell, concentrating near the cleavage furrow by ~3-fold (Fig. 2.4B), whereas CD34 appears segregated between cells but otherwise locally homogenous, consistent with lateral mobility of this membrane protein. The results suggest that high cortical tensions in the cleavage furrow have a similar effect on receptor-independent localization of MIIB as that of local stressing by a micropipette. Partial knockdown of MIIB abolishes the asymmetry and also the segregation of CD34 (Figure 2.4B, bottom). Whereas asymmetric division of $CD34^+$ cells results in 6-fold higher MIIB in the $CD34^+$ daughter than in the $CD34^-$ daughter, knockdown decreases the MIIB level in $CD34^+$ to that in $CD34^-$ and suppresses asymmetric division (Figure 2.4C). Prolonged cultures of MIIB knockdown cells increase the relative number of $CD34^+$ progenitors with more CFU-GM (Figure 2.4D), consistent with MIIB regulating asymmetric division when late $CD34^+$ progenitor cells transition to $CD34^-$ cells and when CD34 molecularly segregates between daughter cells. Tracking of division using carboxyfluorescein diacetate succinimidyl ester (CFSE)

(Hawkins et al., 2007) shows that partial knockdown of MIIB increases the number of $CD34^+CD38^-$ cells by 2-fold (Figure 2.4Ei) or for $CD34^+CD38^+$ cells by 1.5-fold (Figure 2.4Eii), whereas $CD34^-$ numbers remain unaltered (Figure 2.4Eiii). On the other hand, partial MIIA knockdown (~30%) did not alter numbers of any subpopulations (Figure 2.S3B). The data reveal MIIB as a major factor in asymmetric division and differentiation of $CD34^+$ cells to $CD34^-$ cells.

MIIA Dephosphorylates in Differentiation to a Mechanically Active State – (*CSC* 2014)

MIIA is often the dominant MII isoform and can influence MIIB (Raab et al., 2012), which implies that phosphoregulation of MIIA can in principle influence hematopoiesis (Figure 2.5A). We therefore examined regulation by niche factors of pS1943 in $CD34^+$ cells and found the highest levels of pS1943 in uncultured $CD34^+$ cells (Figure 2.5Bi; Figure 2.S13A), with levels systematically decreased upon differentiation with Tpo and Granulocyte-Colony Stimulating Factor (G-CSF), but not Stem Cell Factor (SCF) alone (Figure 2.5Bii). Transforming Growth Factor-β (TGF-β) promotes HSC hibernation (Yamazaki et al., 2011) and blocks the decrease in pS1943 with cytokines (Figure 2.5B). Remarkably, blebbistatin mimics TGF-β (Figure 2.5B). In contrast, very low pS1943 in myeloid $CD33^+$ cells (Figure 2.S3A) and in the human monocytic cell line (THP-1) are consistent with rapid proliferation of THP-1 in suspension (which can be blocked by blebbistatin). Both $CD34^+$ and $CD34^-$ cell numbers anti- correlate with the level of pS1943, and the half-maximal effect was observed at ~35% pS1943-MIIA (Figure 2.5B). MIIA is thus modulated by cytokines critical to pre-circulation differentiation.

Fresh $CD34^+CD38^-$ cells are softer than $CD34^+CD38^+$ (Figure 2.5Ci), and consistent with the high pS1943-MIIA in $CD34^+$ cells. Cells transfected with a site-specific MIIA phosphomimetic mutant (S1943D) fragment more often (from a weak cortex) and also divide more slowly compared to wild-type controls (Figures 2.5Cii and 2.5Ciii). These functional results all indicate that high pS1943-MIIA impacts cell mechanics and limits cell division, and hence, differentiation.

In Vivo **Roles in HSC/Ps: MIIB Contributes to Differentiation, whereas MIIA Confers Survival** – (*CSC* 2014)

Based on our in vitro results, a major knockdown of MIIB in human cells grafted into BM should repress asymmetric division and lead to (1) an accumulation of human cells in marrow and (2) a suppression of circulating human blood cells. To test this hypothesis, fresh human $CD34^+$ BM cells were transduced with shRNA-carrying lentivirus to knock down MIIB, which was followed by puromycin selection of transduced cells. Cells were injected directly into bone of NOD/SCID/IL-$2R\gamma^{-/-}$ (NSG) mice to study BM retention both at 16 hr and at 20 weeks (Figure 2.6Ai); this same duration has been described by others (Notta et al., 2011) as providing ‘‘a stringent test of long-term repopulation’’ of human xenografts injected into the femurs of NSG mice for which ‘‘HSCs were operationally defined by lymphomyeloid engraftment that persisted for at least 20 weeks after transplant.’’ Standards for mouse HSCs differ from those of human (Doulatov et al., 2012), but 12–16 weeks is currently considered as ‘‘long-term engraftment’’ (Oguro et al., 2013). We injected directly into marrow rather than into blood to avoid any potential effect of knockdown on trafficking from blood to marrow.

Human cells in mice were identified by dual immunostaining for hCD45 and hCD47 (Figure 2.S4A), since human RBC and platelets do not express hCD45 while hCD47 confers immunocompatability to all human cells within NSG mice (Rodriguez et al., 2013; Takenaka et al., 2007). Partial permanent MIIB knockdown (by ~40%) (Figure 2.6Aii) leads to 3-fold greater retention of cells in marrow when they are assayed just 16 hr after marrow injection (Figure 2.6Bi); this could reflect the fact that knockdown impairs migration through constraining micropores by 20% ($p < 0.05$; data not shown). Despite this initial retention advantage, the percentage of human PB cells in circulation at 6 weeks after transplantation is 7-fold lower for the MIIB knockdown cells (Figure 2.6Bii), and the difference is maintained after 20 weeks (Figures 2.6Ci and 2.6Cii). Sustained engraftment is evident in control mice with significant human cell numbers in marrow and four of five mice showing human cells in PB. In contrast, MIIB knockdown cells were 6-fold more abundant in marrow, but only one of five mice had human cells in circulation. MIIB is thus required to generate PB cells. Because MIIA is the dominant isoform in hematopoietic cells and is phosphoregulated distinctly in marrow cells versus PB cells, we characterized MIIA contributions to hematopoiesis by performing competitive transplants of BM from tamoxifen-inducible cre-Myh9 knockout mice. These conditional knockout cells (with surface marker CD45.2) were mixed 1:1 with cells from wild-type mice (CD45.1) and injected into sublethally irradiated recipient mice (CD45.1) (Figure 2.6Di). This knockout strategy with mouse cells instead of human cells proved necessary for understanding MIIA because our in vitro results for proliferation indicated no effect with partial knockdown of MIIA in contrast to major defects with MIIB partial knockdown (Figure 2.4A). At 8 weeks after transplantation of the mixed cells, the total

percentage of donor and competitor blood cells was ~50% each, and upon tamoxifen treatment, MIIA decreased as expected only in CD45.2 donor cells (Figure 2.6Dii). In PB, donor myeloid cells decreased rapidly compared to lymphoid cells ($t_{1/2}$ = ~30–40 hr versus ~20–25 days) (Figure 2.6E), but these half-lives are within 2-fold of those reported for both myeloid (Basu et al., 2002; van Furth and Cohn, 1968) and lymphoid (Fulcher and Basten, 1997; Sprent and Basten, 1973) lineages in mouse blood. MIIA loss therefore does not greatly affect viability of terminally differentiated lymphoid cells, while blood cell production from progenitors is clearly suppressed. Consistent with this, we find in BM that $Lin^-Sca\text{-}1^+c\text{-}Kit^+$ (LSK) $CD150^+$ cells (which include progenitors or HSC/Ps; (Kiel et al., 2005)) are reduced 10-fold at just 8 weeks after *Myh9* deletion (16 weeks since transplant), with similar results for LSK in spleen and LS in blood (Figures 2.6Fi, 2.6Fii, and 2.6Fiii, respectively). MIIA is thus required for sustained engraftment *in vivo* and hematopoiesis. An early apoptotic fraction (Annexin-V^+ and 7-AAD^-) of the LSK population also increased just 3 days after *Myh9* deletion (Figure 2.6G), although the total LSK number remained unchanged at this time point (Figure 2.6F). Irreversible loss of MIIA therefore suppresses differentiated cell numbers in the long term as defective HSC/Ps progressively apoptose.

Transient Inhibition of MII with Blebbistatin Spares Only Long-Term Multilineage Reconstituting Cells – (*CSC* 2014)

Blebbistatin is a reversible inhibitor of all MII isoforms, and dose-response studies of $CD34^+$ cultures show that it has a surprising but understandable effect: the diploid ‘‘HSC-enriched’’ population (as phenotypically defined per Majeti et al., 2007

and Novershtern et al., 2011) proves relatively stable to a 3-day treatment, which is long relative to the cell cycle, while the blebbistatin-treated multi-potent progenitors (MPP) and common potent progenitors (CPP) are depleted by 1.8-fold (±0.5) and 31-fold (±16), respectively. By suppressing only the progenitors and sparing the HSC-enriched population, the net effect is an enrichment of the latter among total $CD34^+$ cells by up to 16-fold (Figure 2.7Ai). Whole-genome transcript profiles indeed show that blebbistatin cultures correlate well with fresh HSC-enriched cells and MPP, but not CPP (data not shown), whereas control $CD34^+$ cultures correlate with fresh CPPs. blebbistatin treatment beyond 3 days showed a progressive decrease in the HSC-enriched population, consistent with the conditional knockout studies above that suggest that MIIA is essential for hematopoiesis *in vivo* (Figures 2.6D–F). Functional tests of HSC enrichment by blebbistatin were conducted after washing out the drug and involved measuring the frequency of human cells in NSG mice after limiting dilution serial transplantations into multiple primary and secondary recipients (Figure 2.7B). A total duration of 32 weeks in primary plus secondary xenografts was chosen as sufficient to assess long-term multilineage engraftment of human HSCs in NSG mice (Notta et al., 2011). Our blood analyses 16 weeks after primary transplantation showed that positive engraftment required fewer $CD34^+$ cells (~1 in 10,000) from blebbistatin-treated cultures compared to control cultures (Figure 2.7Bi; Figure 2.S4B). If long-term multilineage engraftment were due solely to progenitors (such as MPPs), then the fact that blebbistatin-treated cultures have relatively fewer progenitors (Figure 2.7A) would have required that more (not fewer) blebbistatin-treated $CD34^+$ cells be injected for reconstitution. Both treated and control cultures also showed a similar percentage of human $CD34^+CD38^-$ and

$CD34^+CD38^+$ populations in BM after transplantation (Figure 2.S4C), indicative of engraftment, and blebbistatin results also compare well to uncultured $CD34^+$ cells in previous studies (Nishino et al., 2011). Sustained secondary engraftment provides an assay for cells with appropriate stem cell properties (Doulatov et al., 2012; Notta et al., 2011; Oguro et al., 2013) and our secondary transplantation results show that blebbistatin maintains a higher fraction of the HSC-enriched population compared to untreated cultures (~5-fold once again). Both treated and control human $CD34^+$ transplants produced a similar percentage of multilineage myeloid and lymphoid cells (Figure 2.7Biii). MKs are unique among blood cells in being naturally polyploid and become more so *in vitro* with blebbistatin treatment, which also increases *in vitro* proplatelet formation (Shin et al., 2011). blebbistatin indeed enriches for mature polyploid MKs in culture by 10 fold (Figure 2.7Ci). For other lineages, the sensitivity of individual progenitor lineages to blebbistatin proves cytokine dependent (Figure 2.6A; Figure 2.S4D). For SCF and Tpo $CD34^+$-derived cells, the IC50 for CFU-GM is lower than that of BFU-E, with blebbistatin producing up to a 2-fold higher ratio of BFU-E to CFU-GM (Figure 2.7Cii). Erythroid lineages are thus preserved under non-Epo and submaximal MII inhibition. In contrast, when cells are cultured with Epo, both CFU-E and BFU-E numbers are reduced (Figure 2.7Ciii). Functional studies thus reveal that short-term reversible MII inhibition in combination with specific cytokines enriches for HSCs, mature MKs, and even erythroid progenitors.

Matrix Determines Tissue Stiffness and Lamin-A Adjusts *In Vivo* – (Science 2013)

To address the relative affect of extracellular matrix and lamins on tissue stiffness, human-derived U251 glioblastoma tumors were grown in the brain and in subcutaneous flank sites of nude mice (Fig. 2.8A). In standard culture, these cells had a low A:B ratio similar to normal mouse brain (Fig. 2.8D). However, flank tumors of U251s had more matrix and were much stiffer than brain tumors, with scaling of collagen density versus matrix elasticity, *E*, appearing typical of normal adult tissue (Fig. 2.8B). Flank tumors of human-derived A549 lung cells (A:B ≈ 2.3) had similar *E* as U251 tumors and were only slightly stiffer than normal subcutaneous tissue, revealing a response independent of initial lamin levels (Fig. 2.8C). Collagenase treatment of fresh tumors reduced *E* by > 50% in just 10 min, suggesting that collagen is a key determinant of tissue stiffness, unlike lamin-A. Consistent with this interpretation, human matrix or matrix-associated proteins were among the few proteins more than twofold higher in the flank compared with the soft brain site. Moreover, human lamin-A levels proved higher in flank versus brain sites (data not shown), whereas lamin-B1 and lamin-B2 were only slightly higher in brain. U251 cells thus adjust their lamin-A:B ratio by 1.5-fold, which fits remarkably well to the stiffness-dependent scaling of lamin-A:B found in normal tissues (Fig. 2.8E).

Figure 2.1 Myosin-II inhibition softens MK cortex and facilitates fragmentation – (*PNAS 2011)*

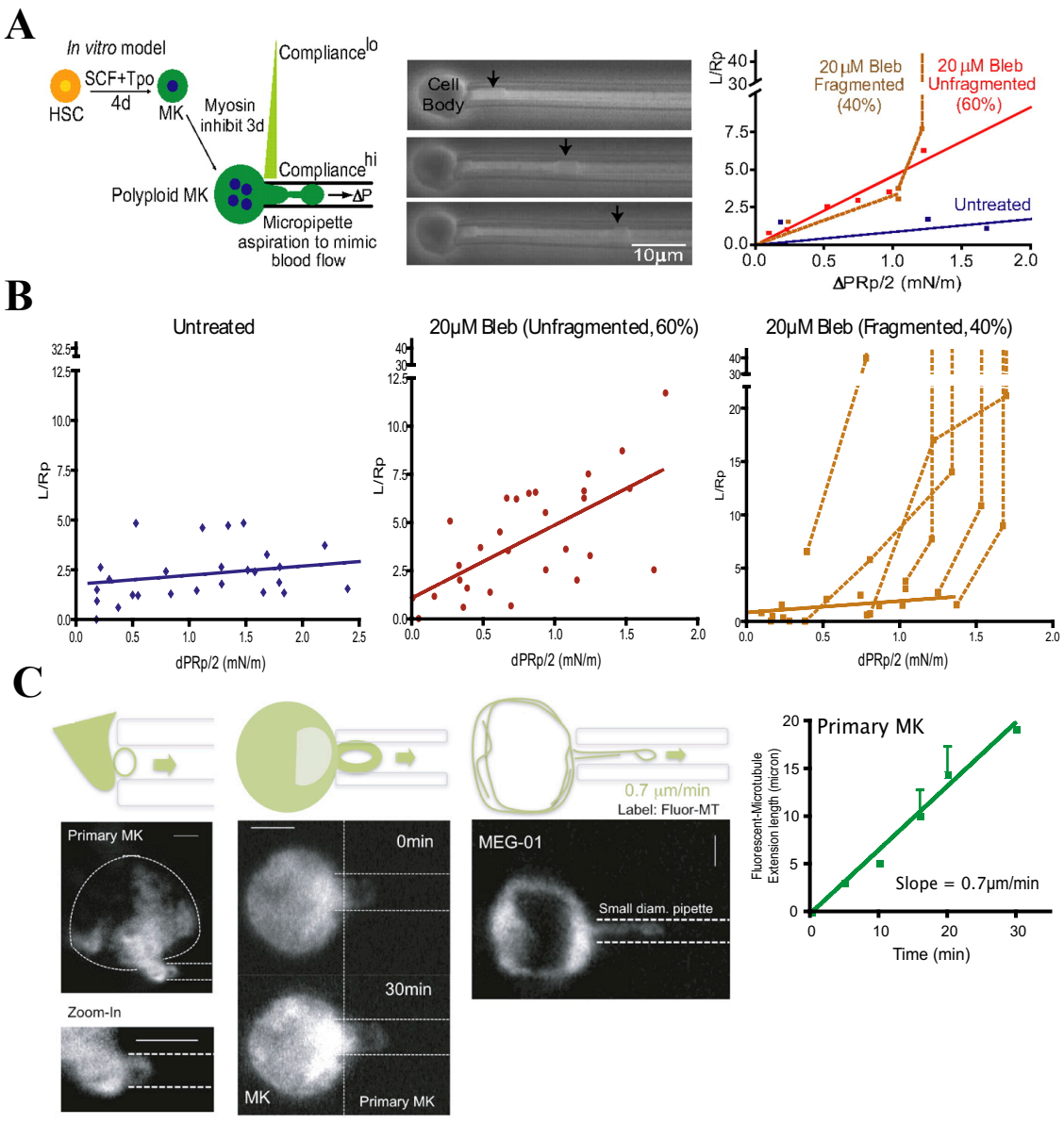

Figure 2.1 Myosin-II inhibition softens MK cortex and facilitates fragmentation – (*PNAS 2011)*

(**A, left**) Modeling MK maturation and platelet fragmentation in vitro by MII inhibition and micropipette aspiration on $CD34^+$-derived cultures. (**A, middle**) Myosin inhibition increases membrane extension and fragmentation in micropipette aspiration. Representative fragmentation within seconds after 30 min of 20 μM blebbistatin treatment and aspiration $\Delta P = 1.4$ kPa. (**A, right**) Aspiration length vs. effective cortical tension with median results shown. (**B**) Micropipette aspiration data from: untreated (n = 14), 20 μM blebbistatin unfragmented (n = 10) and fragmented (n = 6) cells. Slopes indicate compliance in units of $(mN/m)^{-1}$. Untreated cells have median slope of 0.46 ± 0.05, and cells treated at 20 μM and unfragmented have a slope of 3.79 ± 0.84 ($P < 0.0001$). Median fragmentation threshold is ~1 mN/m. (**C**) Primary MKs and MEG01 cells show cortical microtubule coil-like structures in micropipette aspiration. Cells were labeled with a very low and cell-viable dose of fluorescent BODIPY-Taxol (10 nM), which binds specifically to microtubules and not to soluble tubulin. Micropipette aspiration was followed by fluorescence imaging. Representative images are from at least five measurements per cell type. The initial microtubule extension rate measured by lengths of the fluorescent signal over time under aspiration (<10 kPa) is ~0.7 μm/min, consistent with previously reported values. (Scale bars, 10 μm.)

Figure 2.2 Lamin ratios predict nuclear stiffness in hematopoietic lineages – (*PNAS 2013)*

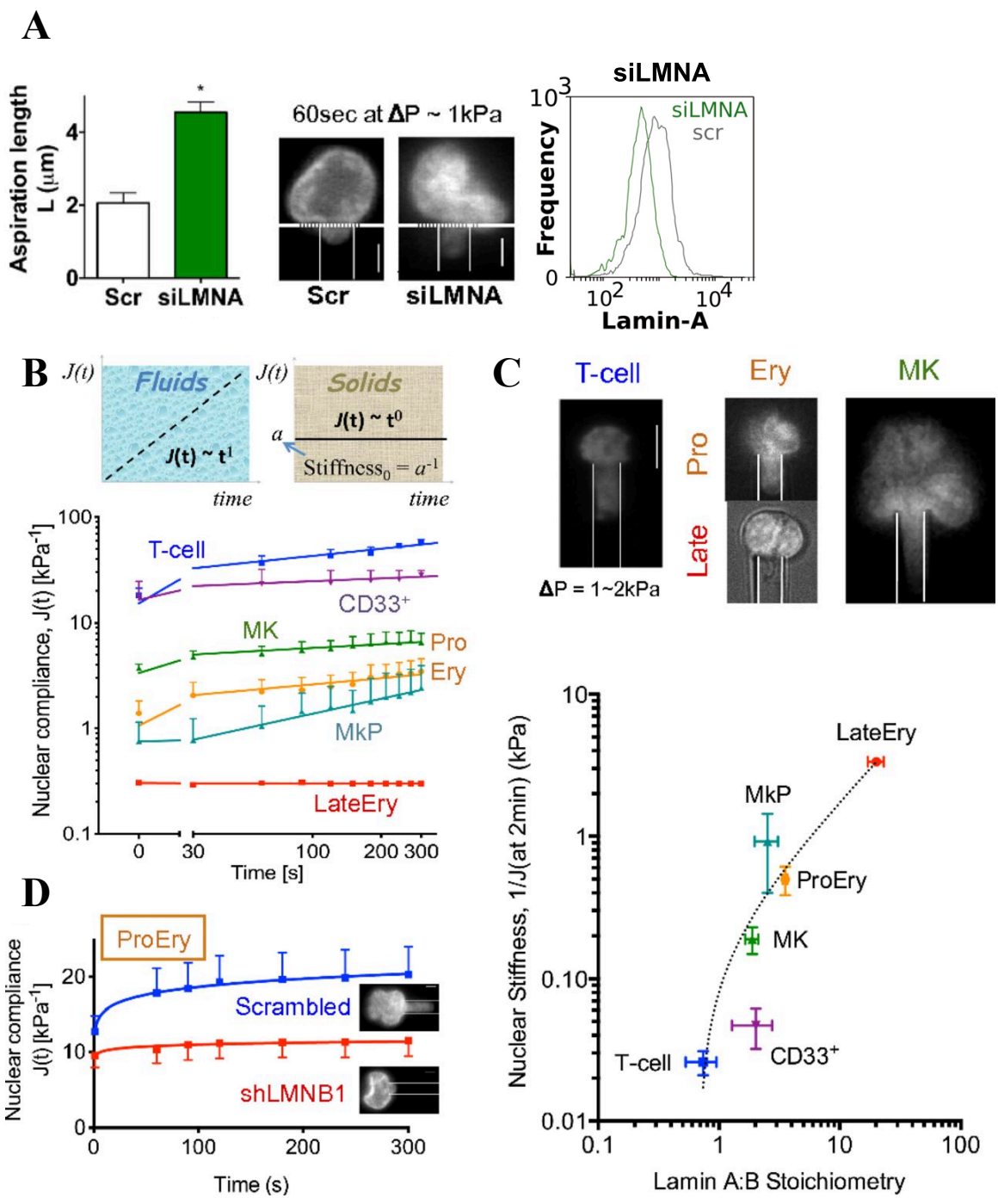

Figure 2.2 Lamin ratios predict nuclear stiffness in hematopoietic lineages – (*PNAS 2013)*

(**A**) Lamin-A confers nuclear stiffness, based on aspiration of G/M cells with or without knockdown with lamin-A siRNA (siLMNA). (Left) Quantitation of aspirated nuclear length (n = 3 donors, *P < 0.05). (Right) Representative image is for ΔP < 1 kPa at 60 s. (**B**) Nuclear compliance change versus time at constant pressure ΔP = 0.3–6 kPa. (Upper) A power law fit, $J(t)\ (kPa^{-1}) = a \cdot t^{b}$ (t = sec) for each blood cell type, where (b = 1 for fluids), (b = 0 for solids). (Lower) Values for (a, b) in each cell type are as follows: (T cell: 15.2, 0.2), ($CD33^{+}$: 16.4, 0.1), (MkP ≥ 30s: 0.16, 0.5), (MK: 3.4, 0.1), (ProEry: 1.1, 0.2), (LateEry: 0.3, 0). (**C**) High lamin-A:B correlates with stiff nuclei. (Upper) Images at 2 min of nuclear aspiration at ΔP = 1–2 kPa. (Scale bar: 5 μm.) (Lower) Correlation between nuclear stiffness (at 2 min) and lamin-A:B fits J (at 2 min) = $0.23*(A:B - 0.68)^{0.91}$ ($R^2 = 0.96$). All results are mean ± SEM of n ≥ 5 for each cell type. (**D**) Lamin-B1 knockdown stiffens nuclei in proerythroblasts, with no change in viable cell numbers (n = 10, P < 0.05). Nuclear compliance change with ΔP = 1–2 kPa where values for (a, b) in each sample are as follows: (scrambled: 12.8, 0.1), (shLMNB1: 9.4, 0.03). (Scale bars: 5 μm.)

Figure 2.3 Lamins regulate erythroid and MK differentiation – (*PNAS 2013)*

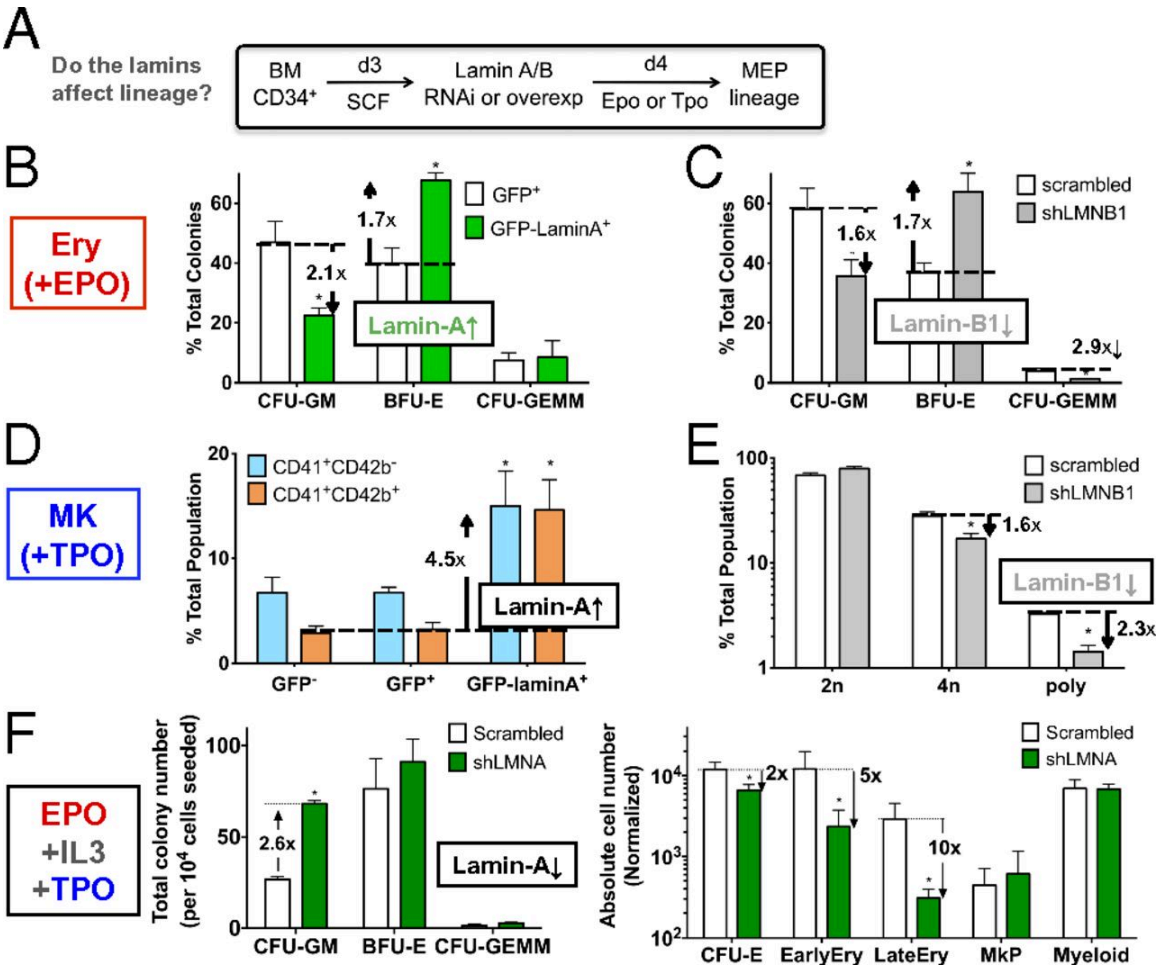

Figure 2.3 Lamins regulate erythroid and MK differentiation – (*PNAS 2013)*

(**A**) Scheme for *in vitro* differentiation. MEP, myeloid and erythroid progenitor; SCF, stem cell factor. (**B** and **C**) Colony-forming assays in methylcellulose medium show a shift to erythroid progenitors after (**B**) overexpression of GFP-lamin-A (~40% transfection efficiency) or (**C**) knockdown of lamin-B1 (shLMNB1, ~50% efficiency) in the presence of Epo for 3 d. *P < 0.05, GFP vs. GFP-lamin-A or scrambled vs. shLMNB1 (n = 3). (**D** and **E**) MK progenitor population enumerated by flow cytometry with CD41 and CD42b. (**D**) MK progenitors increase with lamin-A overexpression. $CD41^+CD42b^-$, early progenitor; $CD41^+CD42b^+$, late progenitor. *P < 0.05, GFP^+ vs. GFP-lamin-A^+ for each progenitor (n = 4). (**E**) Lamin-B1 knockdown decreases average MK ploidy. *P < 0.01, scrambled vs. shLMNB1 (n = 3). (**F**) Lamin-A is required for erythroid differentiation and restricts myeloid progenitor number. Cells were transduced with either scrambled or lamin-A shRNA (shLMNA) and cultured in the presence of Epo, IL-3 and Tpo. Functional progenitors (CFU-GM, BFU-E, CFU-GEMM) were quantified by colony-forming assay (Left) whereas differentiated subpopulations were quantified by flow cytometry as per (Hu *et al*., 2013) (Right), normalized by 10^4 initial cell number. CFU-E, $CD34^-CD36^+IL\text{-}3R^-$; EarlyEry, $CD44^+GPA^+$; LateEry, $CD44^-GPA^+$; MkP, $CD41^+$; Myeloid, $CD33^+$. *P < 0.05, scrambled vs. shLMNA.

Figure 2.4 MIIB polarizes in and promotes asymmetric division of CD34$^+$ to differentiated cells – (*CSC 2014)*

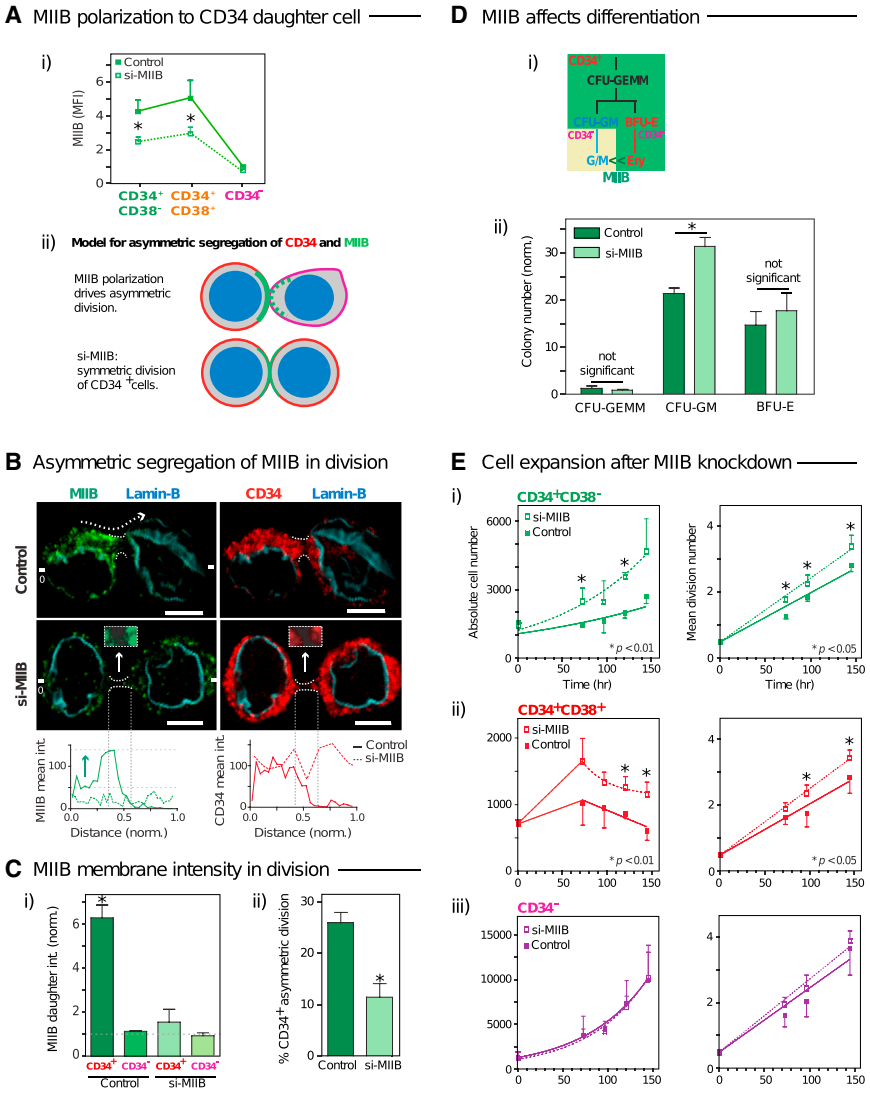

Figure 2.4 MIIB polarizes in and promotes asymmetric division of $CD34^+$ to differentiated cells – (*CSC 2014)*

(**A**) Partial knockdown of MIIB decreases protein by ~40% in $CD34^+CD38^-$ and $CD34^+CD38^+$. (**Ai**) Mean Fluorescence Intensity (MFI) of MIIB protein was measured by flow cytometry. (**Aii**) Hypothetical model for asymmetric segregation of CD34 and MIIB in division shown for WT versus MIIB knockdown. (**B**) MIIB segregates asymmetrically in dividing $CD34^+$-derived cells unless MIIB is knocked down (top). Bar = 5 mm. Intensities of MIIB and CD34 were measured (bottom) along the membrane contour of dividing cells from ‘‘0’’ through the cleavage furrow to the antipole, with distance normalized by total length. A green arrow indicates the difference in MIIB intensity between periphery and cleavage furrow. (**C**) MIIB membrane intensity bifurcates to CD34hi and CD34lo daughters in dividing cell pairs (**Ci**), unless MIIB is knocked down. Percentage of asymmetrically dividing $CD34^+$ cells is suppressed with MIIB siRNA versus control (**Cii**), n>40 cells/group. (**D**) Colony forming assays after 3 days in methyl-cellulose medium supplemented with cytokines. (**Di**) A relationship among different progenitors in terms of CD34 and MIIB expression. (**Dii**) CFU-GM increases with MIIB knockdown. (**E**) Absolute $CD34^+$ cell numbers expand after MIIB knockdown, with normalization to an initial total of 10,000 cells (left), and CFSE tracking shows an increase in mean division number per time (right). Slopes for siMIIB are as follows: control, (0.02: 0.015) for $CD34^+CD38^-$ (**Ei**) and $CD34^+CD38^+$ (**Eii**), and (0.02: 0.02) for $CD34^-$ (**Eiii**). For all graphs, *$p < 0.05$ between Control (= Scrambled) versus MIIB siRNA for each data point, mean ± SEM, and n≥3 donors.

Figure 2.5 Phosphorylation of MIIA regulates the biophysics of CD34$^+$ differentiation – (*CSC 2014)*

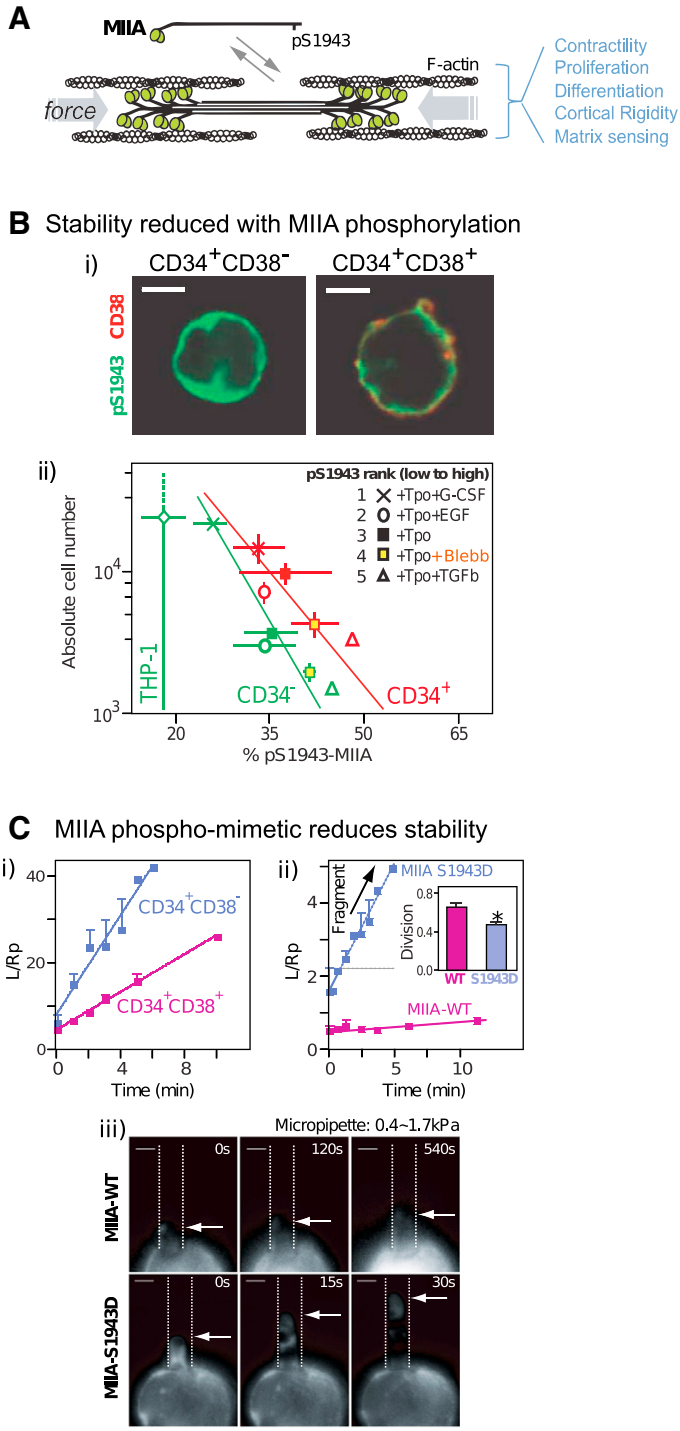

Figure 2.5 Phosphorylation of MIIA regulates the biophysics of $CD34^+$ differentiation – (*CSC 2014)*

(**A**) Dephosphorylation of MIIA at S1943 promotes assembly and function. (B) $CD34^+$ differentiation with soluble factors decreases pS1943. (**Bi**) Representative images showing pS1943 expression in fresh $CD34^+$ cells. Bar = 5 mm. (**Bii**) pS1943 (normalized to MIIA) was measured by flow cytometry [n = 3 donors, ± SEM; fit to Log Y = aX + b (a,b): ($CD34^+$: -0.05, 5.74; in red), ($CD34^-$: -0.10, 6.74; in green)]. Minimum pS1943 per MIIA was measured for THP-1 cells (0.07 ± 0.01). All cells were treated with SCF and indicated cytokines. pS1943% values were normalized as described in Figure 2.S3A (n = 3, ± SEM). pS1943 percentage for SCF only = ~40%. (**C**) MIIA S1943D phosphomimetic decreases both cortical stiffness and cytoskeletal stability. Aspiration length L, normalized by pipette radius, Rp (L/Rp), versus time for various cells with (slope, intercept, effective viscosity h) were as follows: (**Ci**) $CD34^+CD38^-$ (5.7/min, 8.3, 3.2 Pa/s) and $CD34^+CD38^+$ (2.2/min, 4.7, 8.5 Pa/s); (**Cii**) MIIA-WT: (0.02/min, 0.5, 1,400 Pa/s), MIIA- S1943D (0.70/min, 1.6, 40 Pa/s). n = 5, ±SEM. The inset bar graph in (**Cii**) shows the fraction of transfected COS-1 cells after MIIB knockdown that undergo cell division (2n and 4n cells) as calculated by subtracting the fraction of polyploid cells (n = 3, ±SEM, *$p < 0.05$). (**Ciii**) Representative images of aspiration of transfected COS-1 cells (bar = 10 mm, ±SEM).

Figure 2.6 MII isoforms regulate hematopoiesis *in vivo* – (*CSC 2014*)

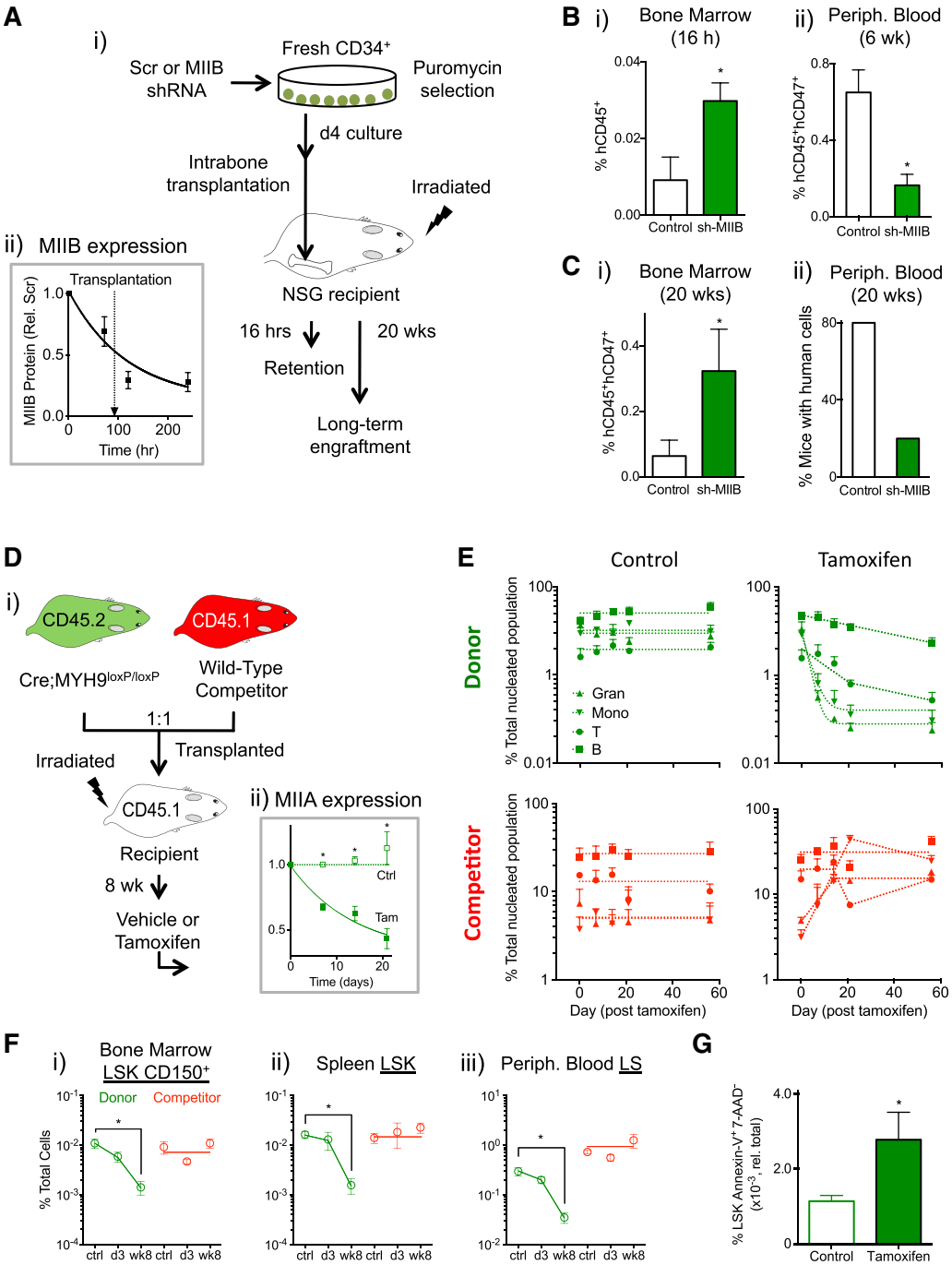

Figure 2.6 MII isoforms regulate hematopoiesis *in vivo* – (*CSC 2014)*

(**A**) Scheme for in vivo experiments to test MIIB functions (**Ai**). (**Aii**) MIIB expression kinetics with shRNA knockdown relative to control. $t_{1/2}$ = 81 hr. n = 5 mice for each group (±SEM for all graphs), transplanted via an intratibial route with $5x10^3$ BM $CD34^+$ cells per sublethally irradiated mouse. Transplantation occurred 4 days after lentiviral transduction, with 2 days puromycin selection. (**B**) MIIB knockdown increases immediate (16 hr) retention in bone marrow (BM) (**Bi**), but decreases short-term (6 week) generation of PB (**Bii**). *p < 0.01 control (scrambled) versus MIIB shRNA. (**C**) MIIB knockdown increases long-term (20 weeks) BM engraftment (**Ci**), but suppresses PB generation (**Cii**). For PB generation, the number of positively engrafted mice is shown (≥0.1% total nucleated cells). (**D**) Scheme for *in vivo* experiment to test MIIA functions (**Di**). BM cells from Cre:*Myh9*loxP/loxP (CD45.2) and from WT competitor (CD45.1) were transplanted at a 1:1 ratio into lethally irradiated WT recipients. (**Dii**) Eight weeks after reconstitution, mice were treated with tamoxifen to delete *Myh9* as assayed by protein expression (*p < 0.01, control versus tamoxifen, n≥3, ±SEM for all graphs). Deletion occurred with $t_{1/2}$ = 9.6 days. n≥8 mice for each group from two independent experiments (±SEM for all graphs). (**E**) PB lineages with deleted *Myh9* are lost from circulation with kinetics similar to clearance of WT cells. The donor (top) and competitor (bottom)- derived granulocyte (Gran, $Gr\text{-}1^+Mac\text{-}1^+$, larger side scatter), monocyte (Mono, $Gr\text{-}1^+Mac\text{-}1^+$, smaller side scatter), T cell (T, $CD3^+$), and B cell (B, $B220^+$) lineages in PB were quantified at the indicated time points after vehicle (left) or tamoxifen (right) treatment. Decay half-lives for tamoxifen-treated donor Gran, Mono, T, and B are 1.3, 1.7, 24.2, and 18.8 days, respectively (**F**) *Myh9* deletion decreases HSC/P subpopulations

across different hematopoietic organs in the long term (8 weeks), but not in the short term (3 days). Donor and competitor HSC/P cells were quantified in BM (LSK-CD150^{+}, **Fi**), spleen (LSK, **Fii**), and PB (LS, **Fiii**) (control versus treated, *p < 0.01). (**G**) *Myh9* deletion increases apoptosis of LSK. Treatment was for 3 days (*p < 0.01).

Figure 2.7 MII inhibition maintains HSC enriched population with long-term multilineage reconstitution potential – (*CSC 2014)*

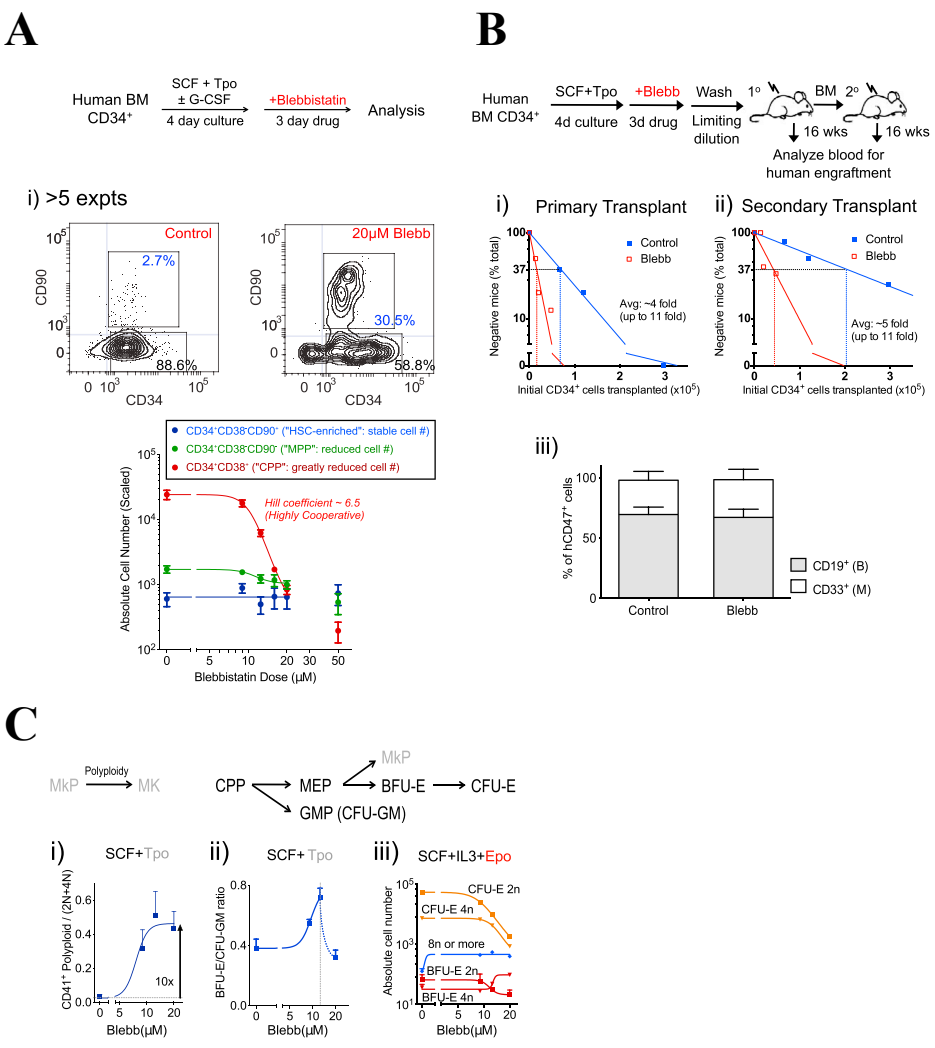

Figure 2.7 MII inhibition maintains HSC enriched population with long-term multilineage reconstitution potential – (*CSC 2014)*

(**A**) Scheme for in vitro experiments (top). (**Ai**) Representative flow cytometry contour plots for $CD34^+$ subpopulations, with dose-dependence of 2n cells showing 15.6- ± 4.1-fold enrichment at 20 mM blebbistatin. Absolute cell numbers were scaled to 10^4 initial cells and fit to dose-response curves: CPP and MPP IC50 = 10.5 mM; HSC-enriched numbers = 646 ± 77 (n≥5 donors, ±SEM). These IC50 values are within ~2-fold of the inhibition constant K_i for pure MII (Kovacs et al., 2004) (**B**) Limiting dilution serial transplant analyses show functional HSCs after MII inhibition after 16 weeks (long-term). (Top) Scheme for *in vivo* experiments. (**Bi**) Limiting dilution primary transplant. The number of transplanted $CD34^+$ cells versus the percentage of unsuccessful engraftment determines the frequency of repopulating cells (n = 26 recipients per group from three independent experiments; $p < 0.0005$). (**Bii**) Secondary transplantation of BM from primary transplant demonstrates the maintenance of higher HSC frequency with blebbistatin compared to control ($n \geq 13$ recipients per group, $p < 0.01$). Transplantation with blebbistatin- exposed $CD34^+$-derived cells shows similar multilineage engraftment in the NSG mice compared to control cells, including myeloid CD ($CD33^+$), lymphoid ($CD19^+$) (**Biii**) (±SEM), and erythroid (GPA^+) (**Biv**). Bar = 5 mm. (**C**) Kinetics of human-$CD41^+$ platelets in circulation were measured after transplantation of human $CD34^+$-derived cells and normalized by the initial number of $CD41^+$ cells transplanted. Areas under curves show significant differences between drug-treated and control. $p < 0.05$ in both phase I and phase II from at least nine recipients in three experiments (±SEM). (**C**) Effects of blebbistatin on progenitors. (**Ci**) Enrichment of polyploidy MKs

by blebbistatin (n = 4). y axis represents the ratios between polyploid MKs and 2n + 4n MKs. EC50 = 7.5 mM; Hill coefficient = 7.0. (**Cii**) Enrichment of BFU-E relative to CFU-GM in the absence of Epo, evaluated by colony forming assays. The maximum ratio was observed at 12.5 mM. IC50 =10 mM, Hillslope = 5.0 (n = 3, ±SEM). (**Ciii**) Sensitivity of erythroid progenitors to blebbistatin in the presence of Epo. BFU-E = $CD34^{+}IL\text{-}3R^{+}CD36^{-}$; CFU-E = $CD34^{-}IL\text{-}3R^{-}CD36^{+}$. Absolute values were normalized to 10^{4} initial cell input and fit to dose-response curves. IC50, Hill coefficient for CFU-E, 2n: 8.7 mM, -4.4 and 4n: 12.9 mM, -6.3; BFU-E, 2n: 10.9 mM, -9.7, 4n: 13 mM, 28, and Poly≥8n: 0.2 mM, 2.0. (n = 2, ±SEM).

Figure 2.8 Lamin-A and collagen levels scale with tissue stiffness, but collagen determines stiffness while lamin-A responds to tissue stiffness – (*Science 2013)*

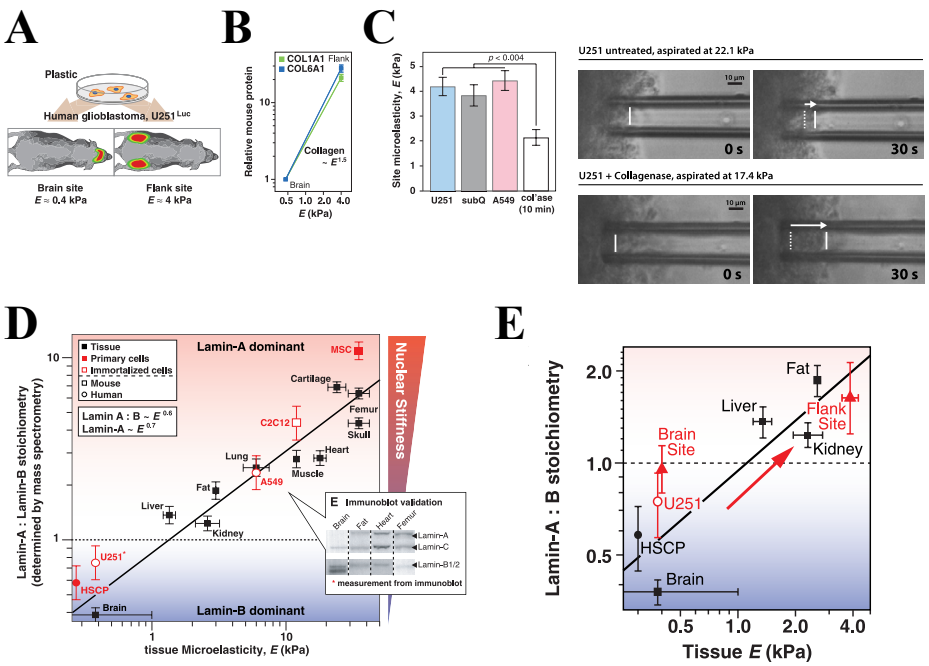

Figure 2.8 Lamin-A and collagen levels scale with tissue stiffness, but collagen determines stiffness while lamin-A responds to tissue stiffness – (*Science 2013)*

(**A**) Human glioblastoma cells U251Luc (expressing luciferase for imaging) were xenografted into mouse brain and flank, and 4-week-old tumors were profiled by MS proteomics. (**B**) Mouse-derived collagens in U251 grown in mouse brain and flank scale with *E* as observed for adult mouse tissues. (**C**) Stiffness of flank tumors made with high (A549) or low (U251) lamin-A:B cells was similar to the stiffness of the subcutaneous site (subQ). Tumors were 50% softer after only a brief treatment with collagenase (col'ase). (**D**) Quantitative proteomics of multiple human and mouse tissues and cells revealed scaling with E of the absolute ratio or stoichiometry of lamin-A to lamin-B through MS quantification of a pan-lamin peptide. Differences in ratios are significant with brain << liver < fat < heart, lung, and muscle << skull << femur and cartilage, where < indicates $P \leq 0.05$ and << indicates $P \leq 0.01$. Nuclei with abundant lamin-A are stiff (20). Cultured cells showed the same trend as their primary source tissue. HSCP, human hematopoietic stem cell progenitors from marrow; U251, human glioblastoma cells from brain; A549, human adenocarcinoma epithelial cells from lung; C2C12, mouse myoblast cells from muscle; MSC, osteo-prone human mesenchymal stem cells from mar- row. (**E**) Lamin composition and stiffness of the tumors fit adult tissue scaling. All points are significantly different where indicated ($n \geq 3$ MS measurements).

2.4 DISCUSSION

The epigenetic changes of lineage specification are likely affected by the nuclear lamina, which might selectively, if indirectly, interact with different chromatin regions during differentiation (Peric-Hupkes et al., 2010). Here, we show roles of the lamins in deformability-based sorting as well as lineage induction of blood cells. This characterization of lamin expression stoichiometry in freshly isolated hematopoietic cells from human marrow and blood demonstrates that absolute lamin A:B ratios correlate with nuclear stiffness (Fig. 2.3B). Although prior studies suggest that lamin-A is "below the detection limit" in terminally differentiated myeloid and lymphoid cells (Gerner and Sauermann, 1999), another study suggested that it is restricted to the late stage of lymphoid development but not earlier stages (Olins et al., 2008). Some studies suggest that B-type lamins are constitutive (Guilly et al., 1990; Röber et al., 1990) whereas other studies indicate that they are down-regulated in primary neutrophils (Olins et al., 2008). One study also acknowledges that, whereas blood granulocytes have much lower levels of both lamin-A and -B than the granulocytic HL-60 cell line, both lamins are detectable by confocal microscopy with distinct polymorphonuclear morphology (Olins et al., 2008). Our efforts to take a standardized approach with MS- IF show that A- and B-type lamins are generally present across different blood-cell types and at different levels. Although our data support some prior studies that total lamin expression is significantly decreased in both lymphoid and myeloid lineages upon differentiation from progenitors ($CD34^{+}CD38^{+}$), lamin A: B ratios are increased to ~1 (Fig. 2.S1B) and correlate with the known distribution of these lineages in marrow versus blood.

Because most small openings between endothelial cells in marrow sinusoids are filled by marrow cells *in situ* (Lichtman et al., 1989), nuclear stiffness seems a reasonable limiting factor. Although it was previously appreciated that granulocytes are highly traffickable due to their unique polymorphonuclear morphology, our study reveals that T cells may be even more amenable to trafficking than granulocytes due to (i) lower lamin A:B ratio (Fig. 2.S1B), (ii) lower marrow:blood cell ratio (data not shown), (iii) lower nuclear stiffness (Fig. 2.2C), and (iv) lower half-maximal pore area for migration (data not shown). In contrast, although MK nuclei remain deformable (Fig. 2.2B), their size and complex morphology generally limit MK migration through small pores. Intact MKs could therefore be occasionally observed in circulation, but further chromatin condensation after exhaustive platelet generation would tend to inhibit traffickability (Lichtman et al., 1989). Flow cytometry analyses of what crosses the micropore filters in our MK experiments indeed show that many more small-cell fragments (e.g., platelet-like particles) traffic across than cells (data not shown), consistent with the platelet generating scheme in Fig. 2.S1A.

Our results indicate that lamin-A:B stoichiometry defines nuclear stiffness, indicating separable roles as distinct polymers in defining viscoelasticity of nuclei. Given that decreasing lamin-A softens nuclei (Pajerowski et al., 2007) (Fig. 2.2A) and that migration sensitivity to pore size increases as the relative amount of lamin-A increases (data not shown), lamin-A dictates time-dependent deformability, which is indicative of a viscous fluid. On the other hand, lamin-B1 confers nuclear elasticity and resilience (Fig. 2.2D) so that its decrease during erythropoiesis produces a nucleus that is slow to recover and effectively stiffer. These results are consistent with previous measurements by

fluorescence correlation spectroscopy (Shimi et al., 2008) showing lamin-A is more mobile than B-type lamins.

Asymmetric division provides a means to maintain stemness while generating the many differentiated cells required for a tissue with high turnover such as blood (10^5 nucleated cells/s). However, it has been unclear as to how two interconnected daughter cells physically sort components to become distinct. While asymmetry of stem cell division in *C. elegans* is driven by its one isoform of MII (Ou et al., 2010), the mammalian homolog, MIIA, is expressed in many cells other than stem cells and unlike MIIB, MIIA polarizes very weakly if at all (Raab et al., 2012; Vicente-Manzanares et al., 2008). Compared to any other hematopoietic lineage, $CD34^+$ cells express the most MIIB relative to MIIA. MIIB polarizes strongly to regions of high cell tension or curvature where it can physically break the symmetry of cytokinesis (Sedzinski et al., 2011). It is therefore almost predictable that MIIB in $CD34^+$ cells will polarize near a cleavage furrow and define the MIIBhi daughter cell in asymmetric division (Figure 2.4). Since MIIB is localized near the membrane and is known to link to membrane proteins (Clark et al., 2006), MIIBhi could also help sort cell surface proteins such as CD34 and thereby correlate with CD34hi as seen. Depletion of MIIB from the CD34lo daughter cell is also propagated as a key aspect of the MII isoform switch that defines and delineates hematopoiesis. How *MYH10* is ultimately repressed in differentiation requires further study: RUNX1 down-regulates *MYH10* during MK differentiation (Lordier et al., 2012), but RUNX1 does not anticorrelate in general with *MYH10* and is not required for normal functions once HSCs are formed from vascular endothelial cells during embryonic development (Chen et al., 2009). Nevertheless, asymmetric processes are hinted at by a

number of polarizable proteins in our early $CD34^+$ cells, including Cdc42, which polarizes in correlation with HSC aging (Florian et al., 2012). Generic polarization of a protein in hematopoietic cells seems predictive of a role in asymmetric division (Beckmann et al., 2007), but MIIB's role in physically breaking the symmetry of cytokinesis seems unique and motivates deeper study of biophysical factors that feed back into transcription programs and perhaps even regulate cancer stem cell differentiation (Cicalese et al., 2009).

Motile cells that are sufficiently adherent can generate enough traction forces to pull themselves apart even in the absence of MII, whereas cells in suspension or daughter cells that cannot crawl away with sufficient force (to break the intercellular bridge) tend to become polyploidy (Zang et al., 1997). HSC/Ps grow well as suspension cells that do not adhere and spread strongly on substrates compared to other solid tissue cell types, and they only possess a thin cortical cytoskeleton; cytokinesis defects are thus likely to favor polyploidy in these cell types. In a blood cancer line that only expresses MIIA, partial knockdown of MIIA indeed increases polyploidy *in vitro* as does blebbistatin and the cancer cells survive (Shin et al., 2011). In healthy human and mouse primary cells, however, such a process of endomitosis is usually seen only for MKs (among blood cells at least), which implies that other cell types are either never tetraploid or apoptose if they become so. Irreversible ablation *in vivo* of MIIA in primary blood cells indeed enhances apoptosis and depletes most dividing blood cell types (Figures 2.6D–G). This seems consistent with cell death in blebbistatin treatments being downstream of MII inhibition. Although the specificity of this drug has been questioned (Shu et al., 2005), the reversible 3-day treatment here with blebbistatin of primary $CD34^+$ cells in vitro increases ploidy of

viable MKs and enhances apoptosis of progenitors with slower dividing stem/progenitor cells dying only with more sustained drug treatments. Our findings ultimately reveal not only a biophysical hierarchy of actomyosin forces in adult hematopoiesis but also some utility in controlling those forces to enrich for stem cells.

Figure 2.S1. Lamin map of human hematopoiesis and correlation analysis between nuclear stiffness and lamins – (*PNAS 2013)*

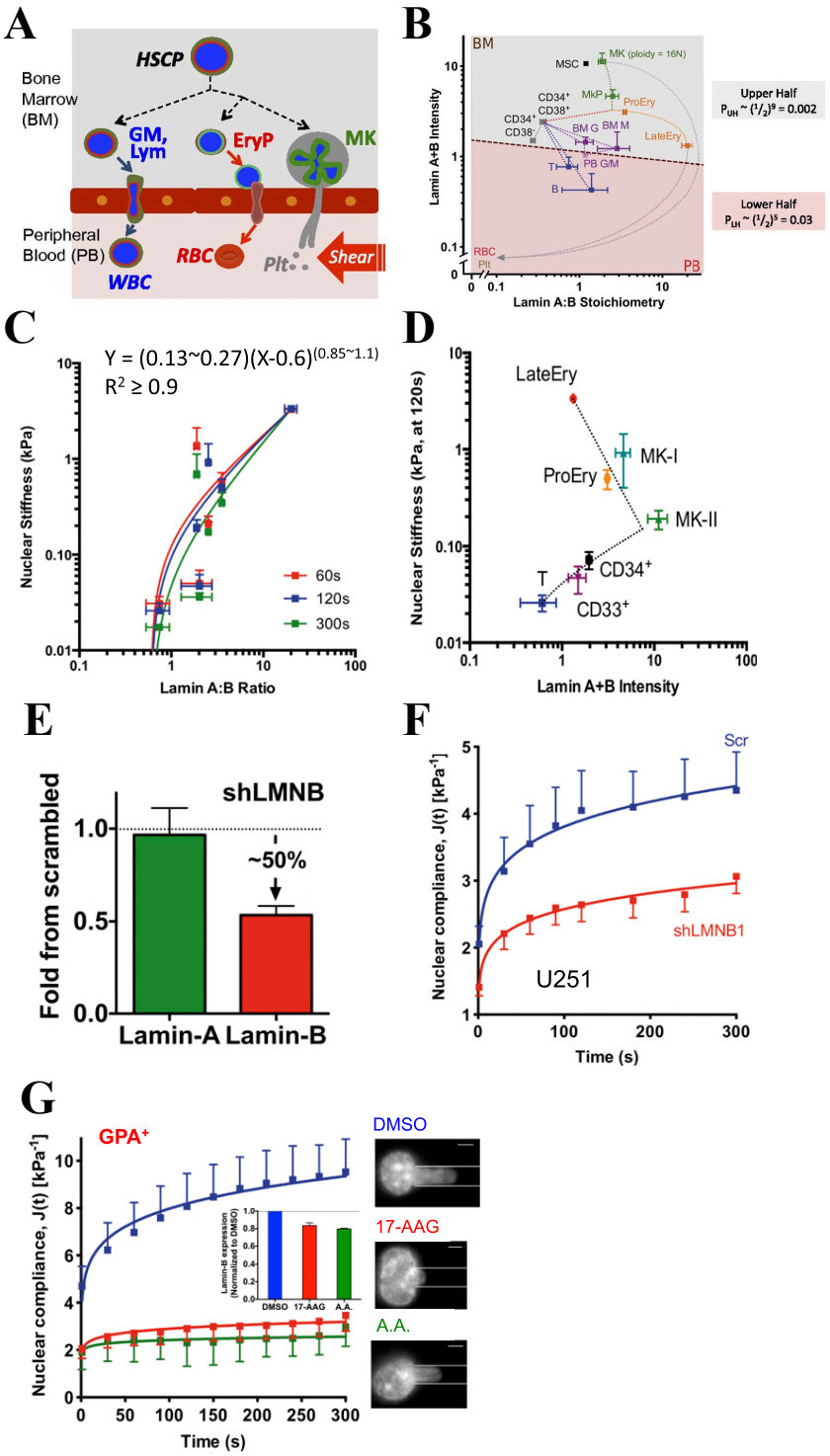

Figure 2.S1. Lamin map of human hematopoiesis and correlation analysis between nuclear stiffness and lamins – (*PNAS 2013)*

(**A**) Hematopoietic cells are mostly in marrow or blood, and only a fraction of cells transmigrate through the endothelium with or without their nucleus. EryP, erythroid progenitors; GM, granulocytes and monocytes; HSCP, hematopoietic stem cell and progenitors; Lym, lymphocytes; MK, megakaryocytes; RBC, red blood cells; WBC, white blood cells. (**B**) Lamin-A relative to B-type lamins, transformed to a measurable A:B ratio versus calibrated sum intensity A+B (a.u.); on log scales, these are the respective difference and sum of chemical potentials for A and B. Mean fluorescent intensity of lamin for each subpopulation from flow cytometry was calibrated to an absolute ratio from MS analyses of a standard A549 cell line (lamin-A:B = 2.3). The dashed line schematically illustrates the semipermeable barrier between bone marrow (BM) and PB, and the net probability of partitioning based on lamin expression can be estimated from the upper half and lower half probabilities: $P_{TOT} = P_{UH}\, P_{LH} = 0.00006$. Measurements are mean ± SEM of $n \geq 3$,with error bars omitted if <5% of mean. BMG, BM granulocytes (CD33mid); BM M, BM monocytes (CD33hi); $CD34^{+}CD38^{-}$, early progenitors; $CD34^{+}CD38^{+}$, common progenitors; LateEry, late erythroblasts ($CD44^{-}GPA^{+}$); MK, polyploid MKs (average 16N); MKP, MK progenitors ($CD34^{-}CD41^{+}$); MSC, mesenchymal stromal cells; PB G/M, PB granulocytes/monocytes; Plt, platelets; ProEry, proerythroblasts ($CD44^{+}GPA^{-}$); RBC, red blood cells; T, B, lymphoids. Representative MSC results from one donor are shown because the variation in A:B ratios between donors and cultured cells was minimal. (**C**) Correlation between nuclear stiffness and lamin A:B ratio at 60, 120, and 300 s after aspiration under constant pressure. The graph

was fitted with a power law, $Y = (0.13\sim0.27)*(X-0.6)^{(0.85\sim1.1)}$, $R^2 \geq 0.9$. Mean ± SEM of n ≥ 5 for each cell type. (**D**) Correlation analysis between nuclear stiffness and lamin total intensity at 120 s after aspiration. The graph was fitted with a power law, $Y = 0.05*(X-0.32)^{0.55}$, $R^2 \geq 0.8$ for T cell, $CD33^+$, $CD34^+$, and MK-II, whereas $Y = 5.50X-1.80$, $R^2 \geq 0.9$ for LateEry, ProEry, MK-I and MK-II. (**E**) Lamin-B shRNA down-regulates lamin-B without affecting lamin-A (n = 3 donors, $P < 0.05$). (**F**) Nuclear stiffening of U251 cells after lamin B1 knockdown. Nuclear compliance change with time under constant pressure $\Delta P \leq 3$ kPa over time with a power law fit, $J(t)$ (kPa^{-1}) $= A \cdot t^B$ (t = sec), where (A, B):): (scrambled (scr): 2.05, 0.13), (shLMNB1: 1.43, 0.13), n = 5, $P < 0.05$, scrambled vs. shLMNB1 at each time point, paired t test. (**G**) HSP90 and histone acetyltransferase inhibitors stiffen nuclei in erythropoiesis. GPA^+ erythroblasts were treated with the HSP90 inhibitor 17-AAG (60 nM) or with the histone acetyltransferase inhibitor anacardic acid (A.A., 20 μM) for 1 d, followed by micropipette aspiration of nuclei. Although GPA^+/hi cells generally have stiffer nuclei than GPAlo (ProEry), all nuclei largely flow irreversibly at constant pressure. Both drugs phenocopy the stiffening of erythroblast and the decrease in lamin-B. Nuclear compliance change with the power law fit (a, b): (DMSO: 4.1, 0.14), (17-AAG 60 nM: 1.9, 0.09), [Anacardic Acid (A.A.) 10 μM: 1.9, 0.05] $P < 0.05$ (n = 5), DMSO vs. 17-AAG or A.A. for each time point in paired t test. (Inset) Graph shows down-regulation of lamin-B with both 17-AAG and A.A. One-way ANOVA $*P < 0.05$, Mean ± SD. (Scale bars: 3 μm.)

Figure 2.S2. Perturbation of lamin-A expression MK polyploidy and colony forming capacity – (*PNAS 2013)*

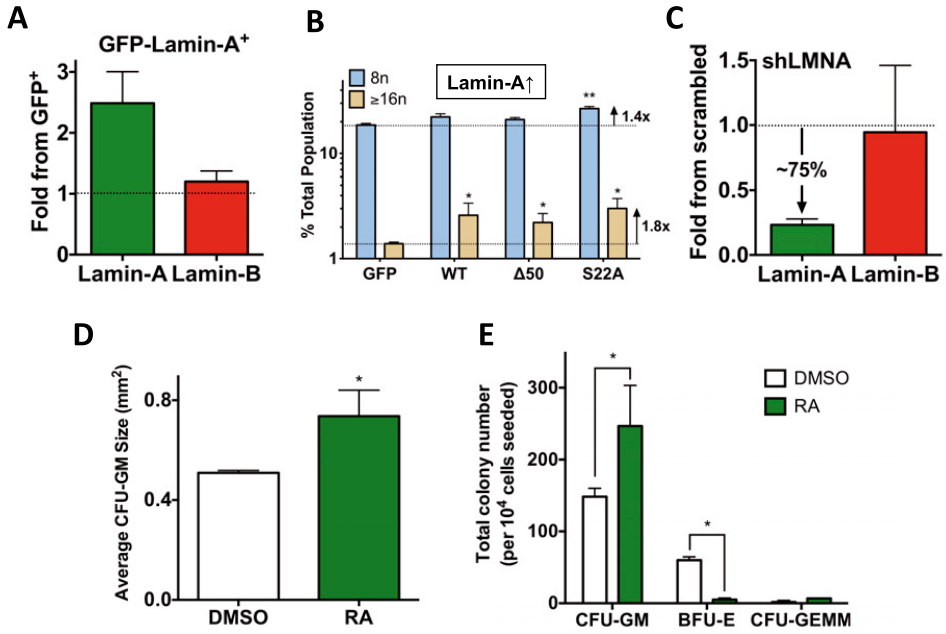

Figure 2.S2. Perturbation of lamin-A expression MK polyploidy and colony forming capacity – (*PNAS 2013)*

(**A**) GFP–lamin-A overexpression increases lamin-A by 2.5-fold compared with GFP control (n = 3 donors, P < 0.05, mean ± SEM). (**B**) Lamin-A enhances MK polyploidization. Overexpression of GFP, wild-type (WT), Progerin mutant (Δ50), and phospho-deficient (S22A) mutant of lamin-A in MEG01 cells. **P < 0.05, GFP vs. S22A 8n. *P < 0.05, GFP vs. WT, Δ50 or S22A (n = 4). (**C**) Lamin-A shRNA down-regulates lamin-A selectively by 75% whereas lamin-B remains unchanged (n = 3 donors, P < 0.05, mean ± SEM). (**D**) Retinoic acid increases the mean size of CFU-GM. (**E**) Retinoic acid increases the number of CFU-GM whereas it decreases that of BFU-E (n = 2 donors, P < 0.05, mean ± SEM).

Figure 2.S3. Myosin-IIA phosphorylation contour and CD34$^+$ quantification following Myosin-IIA knockdown – (*CSC 2014)*

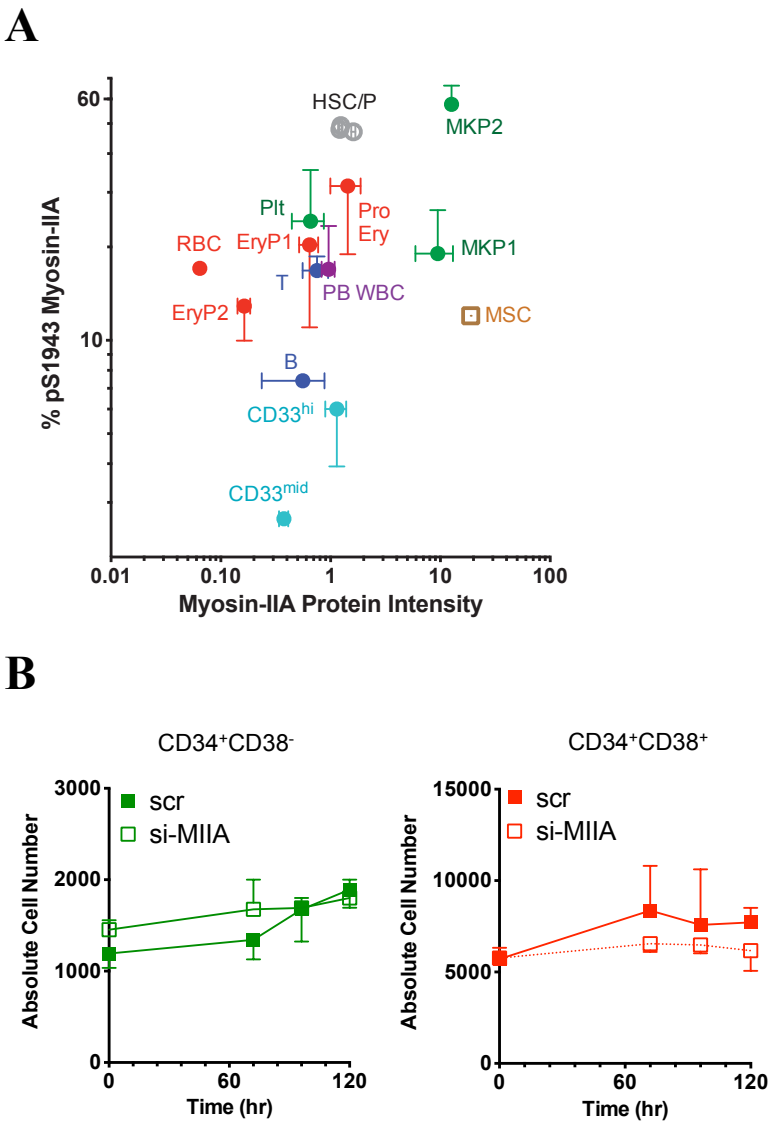

Figure 2.S3. Myosin-IIA phosphorylation contour and $CD34^+$ quantification following Myosin-IIA knockdown – (*CSC 2014)*

(A) % pS1943-MIIA versus total MIIA map (n ≥ 3 donors, ± SEM). (**B**) $CD34^+$ cell numbers do not change after partial MIIA knockdown (30%), evaluated by CFSE tracking as in Fig. 2.4E (n = 2 donors, ± SEM).

Figure 2.S4. Details of primary and secondary transplants following blebbistatin treatment – (*CSC 2014)*

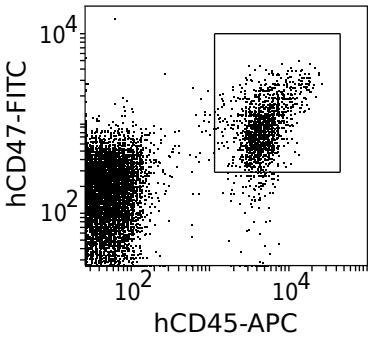

Samples	CD34+ after culture	Primary Transplant	Secondary Transplant
Untreated	67,267	5/8	1/5
	119,485	8/10	2/4
	295,767	8/8	3/4
Blebbistatin	13,791	4/8	0/5
	20,290	8/10	3/5
	47,856	7/8	4/6

Samples	Primary SRC frequency per initial injected CD34+ cell	95% Confidence Interval	P-value
Untreated	1/68,883	1/40,079-1/118,388	
Blebbistatin	1/17,511	1/10,455-1/29,330	P<0.0005

Samples	Secondary SRC frequency per initial injected CD34+ cell	95% Confidence Interval	P-value
Untreated	1/214,849	1/93,542-1/493,467	
Blebbistatin	1/44,615	1/20,929-1/95,108	P<0.01

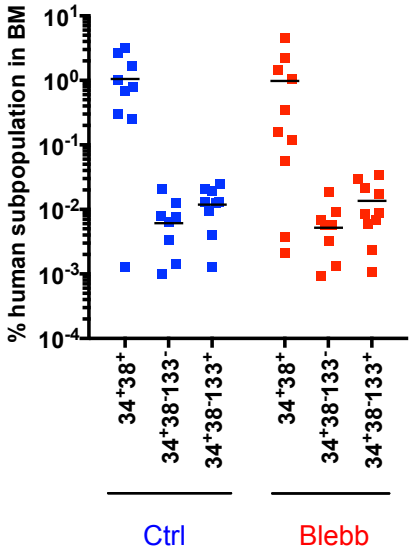

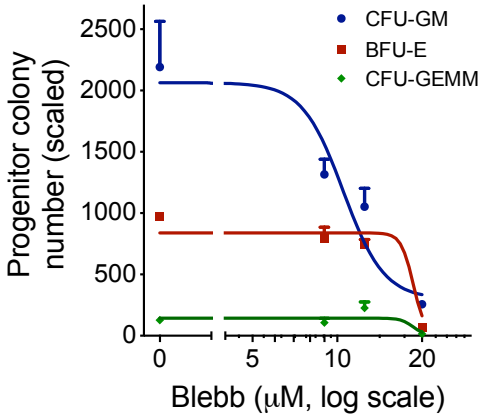

Figure 2.S4. Details of primary and secondary transplants following blebbistatin treatment – (*CSC 2014)*

(**A**) Representative plot showing that most $hCD45^+$ cells from BM are $hCD47^+$ (~97%) in NSG mice 16-wk after transplantation of human $CD34^+$ cells. **(B)** (Top) Summary of primary and secondary NSG transplantation data. (Bottom) Estimation of human SRC frequency in NSG mice by extreme limiting dilution analysis (ELDA) (Hu and Smyth, 2009). **(C)** Quantification of human BM $CD34^+CD38^+$, $CD34^+CD38^-CD133^-$, and $CD34^+CD38^-CD133^+$ subpopulations from NSG mice xenografted with human $CD34^+$ cells, showing no difference between control and blebbistatin-exposed. **(D)** Colony forming assays demonstrate reduced progenitor numbers by MII inhibition. CFU-GM IC50 = ~10.5 μM, Hill coefficient = -6; BFU-E IC50 = 18.6 μM, Hill coefficient = -20 ($n \geq 3$ donors, $\pm$ SEM). Note that BFU-E and CFU-GEMM numbers are not changed under ~15 μM, while CFU-GM number is significantly reduced.

CHAPTER 3: REGULATION OF MYOSIN IIA ACTIVITY IS CRITICAL FOR NORMAL THROMBOPOIESIS AND THE MECHANISMS OF *MYH9*-RD

This chapter appeared as the manuscript currently submitted to Blood and in revision – Myosin-IIA repression favors fragmentation to pre/pro-platelets, but its activation by shear facilitates division to platelets and fails in macro-thrombocytopenia. Spinler KR, Shin JW, Lambert MP, and Discher DE.

Dr. Jae-Won Shin contributed to experiment design. Dr. Michele Lambert provided access to MYH9-RD patient samples and contributed hematological insight.

ABSTRACT

The ploidy of cultured megakaryocytes and the generation of pre/pro-platelets from megakaryocytes are both increased by pharmacological inhibition of MII, but mutations in non-muscle myosin-IIA (MIIA) cause *MYH9*-related diseases (*MYH9*-RD) that adversely affect platelets. In bone marrow, megakaryocytes extend projections into the microcirculation where shear facilitates fragmentation to large pre/pro-platelets, suggesting that fluid stresses and MII activity might couple in platelet biogenesis. Here, in bulk shear, platelet-like-particles generated from megakaryocytes are maximized at a shear stress typical of that in the microcirculation and after treatment with the MII inhibitor blebbistatin. MIIA activity in static megakaryocytes is naturally repressed through phosphorylation at S1943, but shear decreases phosphorylation, consistent with MIIA activation and localization to platelet cortex. Micropipette aspiration of single megakaryocytes shows MII inhibition facilitates generation of $CD41^{+}$ fragments similar in size to pre/pro-platelets, and *MYH9*-RD mutants phenocopy MII inhibition in a dominant negative effect. Blood from a *MYH9*-RD patient with prototypical macro-thrombocytopenia shows diffuse MIIA in large platelets, while normal pre/pro-platelets treated with blebbistatin exhibit diffuse MIIA and fail to divide to small platelets. The findings explain the large platelets in *MYH9*-RD but underscore *a near-normal thrombocrit* in terms of platelet mass. Myosin-II regulation thus controls platelet size and number.

3.1 INTRODUCTION

Intravital imaging of mouse bone marrow has shown that polyploid MKs extend large and flexible proplatelet projections across the fenestrated endothelium into the bloodstream where proplatelets are fragmented by fluid shear (Junt et al., 2007). In vitro studies of mouse MKs have also shown proplatelet extensions can be increased 2~3 fold in length with inhibition of MII by the drug blebbistatin (Chen et al., 2007; Eckly et al., 2010). We showed human MKs treated with the same drug for 3 days increased both MK ploidy and proplatelet numbers, yielding up to 4-fold more functional platelets *in vivo* and *in vitro* (Shin et al., 2011). Drug washout proved essential in the latter studies because normal platelets rely on the A-type isoform, MIIA, to contract wounds and clots (Lam et al., 2011; Maupin et al., 1994). Myosin-II normally contributes to cytokinesis, membrane rigidity, and contraction of matrix, and so its transient inhibition explains both high ploidy MKs and increased proplatelets (Franke et al., 2005). These pharmacological findings and the fact that MIIA is expressed throughout hematopoiesis (Shin et al., 2014) lead us to hypothesize that normal MK-platelet physiology also involves an initial suppression of MIIA activity. This hypothesis brings into focus the cell function(s) that are dysregulated when MIIA (*MYH9)* is mutated in *MYH9*-Related Diseases (*MYH9*-RD). Patients who had previously been diagnosed with May-Hegglin anomaly, Epstein syndrome, or Fechtner syndrome all have autosomal dominant *MYH9*-RD mutations (Seri et al., 2003) with large platelets in reduced numbers (macrothrombocytopenia) and leukocyte inclusions at birth as well as increasing risks with age of developing nephropathy, deafness and cataracts (Balduini et al., 2011).

Myosin-II inclusions suggest dysfunctional protein (Balduini et al., 2011; Eckly et al., 2009; Godwin and Ginsburg, 1974; Kelley et al., 2000; Pecci et al., 2005; Savoia et al., 2010; Seri et al., 2000). However, mice with MK-specific MIIA knockout show a *higher percentage* of MKs with proplatelet buds and larger proplatelets even though there are up to 70% fewer platelets in PB (Eckly et al., 2009). Similar phenotypes are evident in mice expressing *MYH9*-RD mutations D1424N or E1841K that occur in the filament forming tail of MIIA (Zhang et al., 2012). These mutations among others impede filament assembly (Franke et al., 2005), which is necessary for MII contractility. Why such mutants are not phenocopied by blebbistatin inhibition of MII seems paradoxical, especially if our hypothesis is correct that normal MK-platelet physiology initially suppresses MIIA. Here we resolve this apparent paradox with evidence of transient physiological suppression of MIIA in normal MKs. The important effects of shear fragmentation in bulk are clarified first followed by biophysical, pharmacological, and mutagenesis studies of single cells and platelets. Together with comparisons to *MYH9*-RD patient samples, we ultimately provide evidence that in *normal* MKs, MIIA is down-regulated by reversible phosphorylation of MIIA until shear fragmentation to proplatelets. Subsequently, MIIA is normally activated for cleavage of proplatelets to small, contractile-competent platelets – but *MYH9*-RD proplatelets cannot complete the final cleavage.

3.2 MATERIALS AND METHODS

All blood from patients and controls was collected after informed consent with Internal Revue Board (IRB) approval at the Children's Hospital of Philadelphia and the University of Pennsylvania. This study was conducted in accordance with the Declaration of Helsinki.

Materials

For washing or antibody staining of cells, Phosphate Buffered Saline (PBS) without Ca^{2+} or Mg^{2+} (Invitrogen) was supplemented with 1% bovine serum albumin (BSA) (Sigma-Aldrich). For cell culture, RPMI-1640, penicillin-streptomycin, and fetal bovine serum (FBS) were all purchased from Invitrogen. For Western analysis, protease inhibitor mixture was purchased from Sigma. For flow cytometry, 7-Amino-actinomycin D (7-AAD) was purchased from Sigma and Hoeschst 33342 was purchased from Invitrogen. The (±)-blebbistatin was purchased from EMD Biosciences. Prostaglandin E1 was purchased from Sigma.

Antibodies

Primary antibodies used for flow cytometry, Western blotting, and imaging include anti-human CD41-PE or –APC (eBioscience), anti-Annexin V-PE (BD Biosciences), non-muscle myosin-II (MIIA) (Sigma), phosphorylated S1943 MIIA (pS1943 MIIA) (Cell Signaling), β-actin (Santa Cruz). Secondary antibodies include donkey anti-rabbit Alexa 488 (Invitrogen), donkey anti-rabbit Alexa 647 (Invitrogen), and anti-mouse or anti-rabbit HRP-conjugated IgG (GE Healthcare).

Cell Culture and Transient Transfection

MEG-01 cells were obtained from ATCC and maintained in RPMI-1640 supplemented with 10% FBS and 1% antibiotics. Cells were transfected using an Amaxa Nucleofector kit according to the manufacturer's instructions (Lonza). Briefly, 10^6 cells were resuspended in the nucleofector solution and supplement provided in the kit. DNA was added and the sample was placed in the Nucleofector Device and run on the preset program X-005. Cells were then incubated at room temperature for no more than five minutes followed by addition of 1 mL of pre-warmed RPMI-1640 medium and transfer to 6 well plates containing 1 mL of pre-warmed RPMI-1640 per well. Medium was exchanged two times 24 hours after nucleofection. Transfected cells were viable for 2-3 days as confirmed by exclusion of 7AAD staining. Transfection efficiency was ~5% to ~10% for GFP-tagged MIIA constructs (WT, S1943D, S1943A, S1114P, D1424N, E1841K).

For experiments using primary cells, $CD34^+$ bone marrow derived cells were obtained from the University of Pennsylvania Stem Cell and Xenograft Core. Cells were cultured for 3-4 days in the presence of SCF and Tpo (R&D Systems) in Stem Span SFEM II (Stem Cell Technologies) supplemented with 1% antibiotics. After this brief cytokine culture, cells were used as described throughout for MEG-01.

Rheometry and Platelet-Like-Particle Generation

MEG-01 cells treated with DMSO or 20 μM blebbistatin (72 hrs) were washed, resuspended in Ca^{2+}-free Tyrode's + 1:1000 PGE1, and loaded onto a rheometer (Bohlin-

Gemini). After 15 minutes of shear, samples were collected, labeled per Table S1, and analyzed by flow cytometry (LSR-II; BD Biosciences).

Functional Characterization of MEG-01 Derived Platelet-Like-Particles (PLPs)

PLP activity was determined by collagen-I stimulation (100 μg/mL). Sheared samples as described above were labeled per Table 3.S1 and analyzed by flow cytometry.

Micropipette Aspiration

For fragmentation studies, MEG-01 cells were treated +/- 20μM blebbistatin for 72 hrs followed, washed, and stained per Table 3.S1. For mutagenesis studies, transiently nucleofected MEG-01 cells were assayed within 48 hours of nucleofection. For cells treated with blebbistatin, cells were incubated at 37°C with 20 μM blebbistatin for 4 5min, washed, and stained, per Table 3.S1. Capillary tubes of 1.0mm I.D. (World Precision Instruments) were pulled into micropipettes using a Flaming-Brown Micropipette Puller (Sutter Instrument) and cut further using a deFonbrune-type microforge (Vibratome) (<D>~3μm). A micropipette was attached to a dual-stage water manometer with reservoirs of adjustable height. Suction was applied by syringe, and the corresponding pressure was measured by a pressure transducer (Validyne) calibrated by a mercury U-tube manometer. Pressures for different experiments ranged from 0.5 to 20 kPa. Images were acquired using a Nikon Eclipse TE300 inverted microscope using a 40x objective and a Cascade CCD camera (Roper Scientific). Further image analysis was done using ImageJ (National Institutes of Health).

Proplatelet Enrichment, Treatment, and Imaging

Human PB was obtained by venipuncture collected into 10% (v/v) AJ buffer (85 mM sodium citrate, 69 mM citric acid, 20 mg/ml glucose). Proplatelet fractions were enriched and treated as previously described (Thon et al., 2010, 2012). Briefly, PB samples were centrifuged for 20 min at 180g. Buffy and PRP was transferred to a new tube and spun for 15 min at 180g. Buffy and PRP was transferred to a new tube and spun for 15 min at 1000g. The pellet was resuspended in Tyrode's Buffer and treated for 1-6 hrs with DMSO, 10 μM blebbistatin, or 5 μM nocodazole at 37°C. After treatment, samples were seeded onto poly-L-lysine (1μg/ml) coated coverslips, allowed to adhere for 15 min at RT, and fixed with 4% paraformaldehyde. Antibody incubation was done per Table 3.S1.

Proplatelet Flow Cytometry

Human PB collected as described above was immediately fixed with 4% paraformaldehyde and RBCs lysed with 2 volume equivalents RBC Lysis Buffer (Sigma) for 10 minutes at 37°C. For drug treatment, whole blood was treated with DMSO, 10μM blebbistatin, or 5 μM nocodazole at 37°C before fixation/lysis. Fixed and lysed samples were washed twice, resuspended in Tyrode's buffer for and antibody incubated per Table 3.S1 and run on a BD LSRII.

***MYH9*-RD Transfection and Immunofluorescence**

A549 cells were used as they are easily transfected and adherent, which simplifies imaging. Cells were seeded on 18 mm^2 circular microscope cover slips in a 6 well plate and allowed to adhere overnight in F-12 growth media (Life Technologies) supplemented

with 10% fetal bovine serum (FBS) and 1% penicillin-streptomycin. *MYH9*-RD constructs were introduced via transfection using Lipofectamine 2000 (Life Technologies) as per the manufactures protocol. Briefly, media was removed from cells and replaced with 800 μL Opti-MEM (Life Technologies) per well. Two cocktails were prepared for each reaction. Cocktail A consisted of 7 μL Lipofectamine 2000 + 93 μL Opti-MEM. Cocktail B consisted of 3 μg DNA + Opti-MEM to bring total volume to 100 μL. A and B were combined and after 5 mins were added dropwise to each well. Cells were incubated for ~5 hours at 37°, 5% CO_2 after which media was replaced with F-12 growth media and allowed to incubate overnight.

The following protocol was followed for visualizing *MYH9*-RD induced MII aggregates as well as MII expression in *MYH9*-RD patient platelets. Cells were briefly fixed with 4% paraformaldehyde followed by three PBS washes. Next, cells were permeabilized with 0.5% Triton X-100 then blocked using 3% BSA + 0.05% Tween-20. Either total MII or pS1943 MII primary antibody was added at 1:100 by dilution with blocking buffer and incubated for 5-6 hours at room temperature. Cells were washed three times with PBS and either Alexa 488 or Alexa 647 secondary antibody was added at 1:400 diluted with PBS. For patient platelet experiments, CD47-APC was added at 1:100. After incubation at room temperature for 60 minutes, cells were washed twice followed by addition of Hoescht 33342 1:10,000, incubation at room temperature for 5 minutes, and another two PBS washes. Cover slips were then mounted on slides using ProLong Gold Antifade Reagent (Life Technologies), sealed with nail polish, and cured for 24 hours before imaging. Images were acquired using an Olympus IX71 inverted microscope with a

300W Xenon lamp illumination using 40x, 60x, or 150x objectives with or without 1.6x multiplication. Further image analysis was done using ImageJ.

Western Blotting

In general, cells were washed with ice-cold PBS and lysed on ice with lysis buffer (150 mM sodium chloride, 1% Nonidet P-40, 1% protease inhibitor mixture, 1 mM activated sodium orthovanadate, 50 mM Tris at pH 8.0) for 30 mins. Whole lysates were separated on 3%-8% sodium-dodecyl sulfate polyacrylamide gel electrophoresis (SDS/PAGE) gels (NuPAGE 3-8% Tris-Acetate, Invitrogen). The proteins were then transferred to a polyvinylidene fluoride (PVDF) membrane with an iBlot Gel Transfer Device (Invitrogen), followed by blocking with 5% nonfat dry milk solution for 1 hr. Incubation with primary antibodies was done at 4°C overnight with 1:1000 β-actin or 1:1000 HSP90, and 1:1000 MIIA or pS1943 MIIA antibodies. After washing, the membrane was incubated with 1:2500 anti-rabbit and 1:2500 anti-mouse HRP-conjugated IgG antibodies at room temperature for 1 hr. The blot was developed with ChromoSensor (GenScript) for 5 mins, followed by digital scanning to perform densitometry analysis by ImageJ.

Statistical Analysis

All statistical analyses were performed using GraphPad Prism 4. Unless otherwise noted, all statistical comparisons were made by unpaired two-tailed Student *t* test and were considered significant if $P < 0.05$.

3.3 RESULTS

Optimal shear stress for platelet-like-particle generation is maximized by MII inhibition

As an initial cell type to explore MII's role in platelet generation, we used the human megakaryocytic cell line MEG-01 which has been used by others as a model for both human MK and platelet generation (O'Brien et al., 2008; Takeuchi et al., 1998). A cone-and-plate rheometer mimics *in vitro* the shear stress applied to MK projections *in vivo* (**Fig. 3.1A**), with a narrow gap size (60 μm) and controlled temperature (37ºC). Compared to unsheared MKs, an optimal shear stress of ~2 Pascal (Pa) generates up to 2-fold more $CD41^+$ PLPs (platelet-like particles), and MKs pretreated for 3 days with blebbistatin to increase MEG-01 ploidy (**Fig. 3.S1**) produce >4-fold more PLPs (**Fig. 3.1B**). The optimal shear coincides with arterial vessel shear stress (1.5 – 3.0 Pa) (Schubert et al., 2000), and higher shear stresses suppress fragmentation to $CD41^+$ PLPs. Importantly, shear and blebbistatin have similar effects on primary human MKs. Bone marrow derived $CD34^+$ cells were cultured for 3-4 days in the presence of SCF and Tpo to direct differentiation towards MKs, and an additional 3 days of culture with blebbistatin promoted polyploidy and MK maturation per our recent studies (Shin et al., 2011). Shearing the treated cells indeed results in ~5-fold more $CD41^+$ PLPs relative to static untreated culture (**Fig. 3.1C**).

To assay PLP functionality, collagen-I activated aggregation was measured. Sheared cell suspensions were stimulated with 100 μg/mL collagen-I in the presence of 1 mM $CaCl_2$ followed by flow cytometry analyses (**Fig. 3.1D**). Activation was determined for the Annexin-V^+, 7-AAD^-, $CD41^+$ aggregated population with aggregation revealed by

high side scatter as reported by others (O'Brien et al., 2008). In the absence of collagen-I, activated aggregation was always low (<2%) but was also 2-3 fold higher at the highest shear compared to static or optimal shear. Such shear activation (Lu et al., 2013) might also underlie the decrease in PLP numbers at high shear (**Fig. 3.1B**) – as examined in a related context in the next section. Collagen-I stimulation of MEG-01 derived PLPs shows ~12% activated PLPs from static, untreated cultures and ~12-20% activated PLPs from blebbistatin treated, sheared cultures (**Fig. 3.1D**). Neither shear stress nor blebbistatin impacts fragment activation. Stimulation of primary human MK derived PLPs shows ~70% activation regardless of MII inhibition, and this level of activation is observed for either static or 2 Pa sheared samples (**Fig. 2.1E**).

Scaling the absolute number of MEG-01 derived PLPs generated (**Fig. 3.1B**) by the activation results (**Fig. 3.1D**) provides a more accurate accounting of functional PLPs (**Fig. 3.1F**). An optimum at 2 Pa shear emerges for 20 μM blebbistatin, with an ~8-fold increase in functional PLPs compared to those from static, untreated MEG-01 cultures. Whether the optimum results from loss of functionality at high shear or else high shear affecting fragmentation itself is addressed by investigating the MK's response to shear stress.

Myosin-IIA heavy chain is stress activated

Contractility of platelets is important to wound closure (Lam et al., 2011), and we have found recently that primary hematopoietic stem cells maintain a high level of MIIA phosphorylated on S1943 (pS1943) that tends to deactivate MIIA (**Fig. 3.2A, sketch**) and this phosphorylation generally decreases through differentiation (Shin et al., 2011).

Dephosphorylation is known to shift the equilibrium from soluble, cytoplasmic dimers toward assembled bipolar filaments (Alberts et al., 2007) that interact with actin filaments in contributing to cell division, membrane rigidity, and strong adhesion to rigid matrices. Our previous studies also showed late MKs relative to fresh platelets have ~3-fold higher pS1943 per MIIA (Shin et al., 2011). Here, increasing shear stress on MEG-01 cells (**per Fig. 3.1A**) decreases pS1943 per MIIA in a physically reasonable exponential form to ~3-fold lower levels relative to static culture (**Fig. 3.2A, plot**). Shear activation of pS1943 by dephosphorylation as measured by single cell flow cytometry (**Fig. 3.2A**) decays to a minimum by ~4-6 Pa, as confirmed by immunoblot (**Fig. 3.2A, inset**), which might explain the decrease in PLP generation at shear stresses >2 Pa. Importantly, fresh human platelets exhibit the same low level of pS1943 (**Fig. 3.2A star & Fig. 3.S2**). Mature MKs in bone marrow are certainly shielded from fluid shear and should in principle maintain a high level of pS1943 to enhance polyploidization (mimicked *in vitro* by blebbistatin) and to suppress cortical rigidity during proplatelet extension and fragmentation (**Fig. 3.2B**). Prolonged exposure to shear stress would deplete pS1943 and thereby remove the block on MIIA activity to obtain a contractile phenotype *only* in circulating platelets. Such a post-translational activation would be consistent with previous interpretations of the MIIA gene in mice, *Myh9*, as a negative regulator of platelet generation (Chen et al., 2007), for which complete knockout causes defects in proplatelets and MK viability (Eckly et al., 2010).

One prediction of the shear stress activation model is that wild-type MII should localize at the appropriate place and time with stress, and so micropipette aspiration was used to apply local stresses to proplatelet-like projections of MEG-01 cells while imaging

GFP-MIIA constructs (**Fig. 3.3A, sketch**). WT MIIA indeed accumulates over minutes toward the highly stressed tip of the membrane projection (**Fig. 3.3A**, upper image), consistent with a mechanosensitive response seen first for *dictyostelium* MII (Ren et al., 2009). Intravital imaging (Junt et al., 2007) has suggested MKs extend proplatelet pseudopods into blood in <15 min with fragmentation in ~30 min, although *in vivo* stresses are unknown. A phospho-mimetic S1943D mutant of MIIA proves unresponsive as it distributes uniformly along the aspirated length, and a non-phosphorylatable S1943A mutant remains more in the cell body and is depleted along the aspirated length (**Fig. 3.S3**). Treating the nucleofected cells with blebbistatin for 30 min prior to aspiration suppresses the mechanosensitive response of WT as well as S1943A's decay along the aspirated projection, producing a more uniform S1943D phenotype for all. Projections of aspirated membrane for the S1943D mutant and for blebbistatin treated cells were also softer in distending more under high aspiration stress than for WT or S1943A (**Fig. 3.S3**). The results thus suggest a high level of pS1943 favors proplatelet extension to facilitate fragmentation into the bloodstream (**per Fig. 3.2B**) while also ensuring that the resulting platelet population has relatively homogeneous MII levels among fragmented proplatelets.

Consistent with phosphorylation-induced repression of MII during platelet biogenesis, micropipettes with diameters similar to small human capillaries (~3 μm) show that blebbistatin facilitates generation of $CD41^+$ fragments (**Fig. 3.3A**, right micrograph) in greater numbers than without inhibition (Fig. 3B). Larger diameter micropipettes also cause fragmentation, but blebbistatin always provides higher yields. Fragment sizes decrease with decreasing micropipette diameter but do not depend on MII

inhibition (**Fig. 3.3C, 3.S4**). The composition of similarly induced erythrocyte membrane fragments agrees well with that of microvesicles generated in processes such as reticulocyte maturation to discocytes, suggesting physiological relevance (Knowles et al., 1997). Here, $CD41^+$ fragments are similar in size to normal human preplatelets (**Fig. 3.3C, 3.S4** shaded regions), and we showed previously that membrane projections and fragments in micropipette aspiration have taxol-staining microtubules (Shin et al., 2011) similar to those seen in MK proplatelets and platelets (Italiano et al., 1999). The results thus indicate that down-regulation of MII activity facilitates formation and fragmentation of MK projections, but size of $CD41^+$ fragments depends on capillary diameter.

***MYH9*-RD mutants are not activated by stress**

Mutations in the tail of MIIA can cause *MYH9*-RD, with mutants S1114P, D1424N, and E1841K studied here all blocking myofilament assembly (Balduini et al., 2011) even when mixed with WT MIIA, suggesting dominant negative phenotypes (Franke et al., 2005). Patients expressing the E1841K mutation have macro-thrombocytopenia with normal platelet aggregation but no change in platelet shape (Canobbio et al., 2005). Here, PB samples from a patient with a D1424N mutation showed macro-thrombocytopenia with increased platelet size and a reduced platelet count of 21.8 fL and 90,000/μL, respectively. Immunofluorescence imaging of MIIA and pS1943 in platelets that were allowed to spread on glass coverslips (**Fig. 3.4A**) shows an absence of normal peripheral MIIA localization in patient platelets (**Fig. 3.4B**). In contrast, pS1943 distribution remains diffuse in both normal and patient platelets, consistent with the imaging of the synthetic S1943D mutant. MIIA density is also decreased in patient platelets compared to

normals (**Fig. 3.4C**), which is consistent with previous studies of *MYH9*-RD showing up to 50% deficiency in total MIIA (Deutsch et al., 2003); in contrast, pS1943 densities are similar for normal and patient (**Fig. 3.4D**). The diffuseness of the patient's total MIIA is thus consistent with a significant fraction of MIIA being inactive.

Mean projected areas of platelets are larger for the patient as expected, with an increase from 6.9 μm^2 for normals to 19 μm^2 for D1424N patient, which is about half the size of mature RBCs (**Fig. 3.4E**). Platelet perimeters and calculated circularity (Thon et al., 2010) for normals show a mixture of high circularity, small perimeter normal platelets with dumbbell-shaped, large perimeter proplatelets and high circularity, large perimeter preplatelets (**Fig. 3.4F**). Platelets from the *MYH9*-RD patient were predominately high circularity and large perimeter, corresponding to preplatelets (**Fig. 3.4F**), consistent with previously noted effects of EDTA anticoagulant on repressing the dumbbell-shaped proplatelets (Thon et al., 2012). Past observations of a cleavage furrow (Schwertz et al., 2010) and a "snapping" back of the membrane following proplatelet fission (Thon et al., 2010) thus suggest a role for *active* MII similar to that in cytokinesis of MK progenitors (Shin et al., 2011).

A plot of normal peripheral thrombocrits from platelet count and size data of Thompson *et al* (Thompson and Jakubowski, 1988) shows that our D1424N patient has a peripheral thrombocrit in the normal range (**Fig. 3.4G**). Mouse models with the D1424N mutation have approximately two-fold more MKs in the marrow than normal mice (Zhang et al., 2012), and if such compensation also occurred in humans, the patient thrombocrit per MK approaches a linear fit of the normal data. These findings support a hypothesis for *MYH9*-RD defects in terminal platelet processing (**Fig. 3.4H**), consistent

with normal biogenesis of platelets in which pS1943 deactivates MIIA in earlier steps (**Fig. 3.2B**). Thus, in normal platelet generation, large pre/pro-platelets sheared from the pS1943-rich processes that are extended by MKs can reversibly convert between proplatelets and preplatelets, but the pinching and subsequent fission to properly sized platelets is driven by MIIA. The conclusion that pre-/pro-platelets in *MYH9*-RD patients can be readily generated but cannot undergo fission helps to explain the increased MPV and decreased platelet count with reasonable maintenance of peripheral thrombocrit. Two key aspects of this model are examined next: 1) *MYH9*-RD mutants act as dominant negatives in stress-induced membrane fragmentation, and 2) normal MII activity is ultimately needed for cyto-fission to platelets.

***MYH9*-RD mutants exert dominant negative effect in fragmentation of projections**

In micropipette aspiration of MEG-01 cells expressing *MYH9*-RD mutants as GFP fusions, the fluorescence on the aspirated projection appeared nearly flat and time-independent as did blebbistatin-treated cells expressing the wild-type GFP-MIIA (**Fig. 3.5A**). Fragments generated per cell were likewise similar for *MYH9*-RD mutants and for blebbistatin treated MEG-01's (non-transfected), and all were significantly higher than DMSO treated control while they were *zero* for wild-type GFP-MIIA expressing cells (**Fig. 3.5B**). The transfected cell results thus reveal a dominant negative effect of *MYH9*-RD on fragmentation since the constructs are overexpressed to mimic the stoichiometry of a heterozygous state (with immunostaining of total MIIA being 60% higher in GFP expressing cells than non-expressing cells, **Fig. 3.S5**). Consistent with past reports for granulocytes (Deutsch et al., 2003; Pecci et al., 2005; Savoia et al., 2010) and and in

contrast to wild-type GFP-MIIA that appeared cortical (**Fig. 3.3A**), the *MYH9*-RD mutants expressed in MEG-01 cells showed more GFP aggregates against a diffuse GFP signal – which we quantified in well-spread cells (Fig. S5). Additionally, in micropipette aspiration of MEG-01's, the mutants did not affect fragment size (**Fig. 3.S4**), consistent with the above noted lack of size difference between fragments from blebbistatin treated and control cells (**Fig. 3.3C**). Cells overexpressing *MYH9*-RD mutants were slightly larger than cells overexpressing WT MIIA despite similar GFP intensities (**Fig. 3.5C**); however, DMSO control treated MEG-01's were larger than transfected cells, while blebbistatin treated cells were the largest (**Fig. 3.5C**), consistent with their higher ploidy (**Fig. 3.1A, 3.S1**). Since MK size relates to maturity (Mattia et al., 2002) (ploidy, proplatelet extension, and platelet release), overexpression of normal MIIA tends to suppress size/maturity whereas *MYH9*-RD mutants slightly increase MK size/maturity and disproportionately increase fragmentability (*vs* DMSO, **Fig. 3.5B**).

Myosin-IIA activity is critical to pre-/pro-platelet fission to platelets

To determine whether normal MIIA activity is necessary for final fission to platelets, which seems defective in *MYH9*-RD, PB from healthy anonymous donors collected into buffer was enriched for proplatelets as described by others (Thon et al., 2012). Cultures at 37°C were treated for 1 or 6 hrs with blebbistatin or nocodazole to respectively inhibit MII or depolymerize microtubules. Immunostaining for MIIA reveals that the normal peripheral distribution is made diffuse by blebbistatin but not by nocodazole (**Fig. 3.6A,B**). Additionally, MIIA localizes to the cleavage furrow of proplatelets, and immunostaining for the other hematopoietic isoform (Shin et al., 2014), MIIB, indicated a

relative intensity of MIIA:MIIB ~ 250 that confirms MIIA as the relevant isoform. Quantitation of circularity and perimeter per recent studies (Thon et al., 2012) suggests small perimeter platelet populations always dominate, but both drug treatments enrich for the large discoidal preplatelet populations compared with DMSO controls (**Fig. 3.6C**). Relative to the barbell-shaped proplatelets, the preplatelets shift from ~1:3 for DMSO control cultures to ~40:1 for blebbistatin treatment and ~8:1 for nocodazole treatment (**Fig. 3.6C**). No significant difference between 1 and 6 hrs suggests that the transition takes 10's of min or less, which is consistent with the mechano-activation kinetics of MIIA (**Fig. 3.S3**) and also with cytokinesis in mitosis (Shin et al., 2011). While both MIIA and microtubule activity drive these conversions, inhibition of MIIA alone generates large platelets with diffuse MIIA that appear similar to *MYH9*-RD platelets (compare **Fig. 3.6A,B** with **Fig. 3.4A**).

Flow cytometry was done on whole blood samples after treating for 1 hr with DMSO, blebbistatin, or nocodazole. Samples were fixed following drug treatment, and RBCs lysed prior to incubation with antibodies. Populations were determined from scatter of normal human platelets and calibration beads, and platelets were gated as $CD41^{+}$, $Hoechst^{-}$, GPA^{-}. In agreement with immunofluorescence, drug treatment compared to control showed a significant increase in the ratio of preplatelets to proplatelets resulting from an increase in preplatelets at the expense of proplatelets (**Fig. 3.6D**).

Figure 3.1 Shear stress and pharmacological inhibition of myosin synergistically enhance platelet-like-particle generation *in vitro*

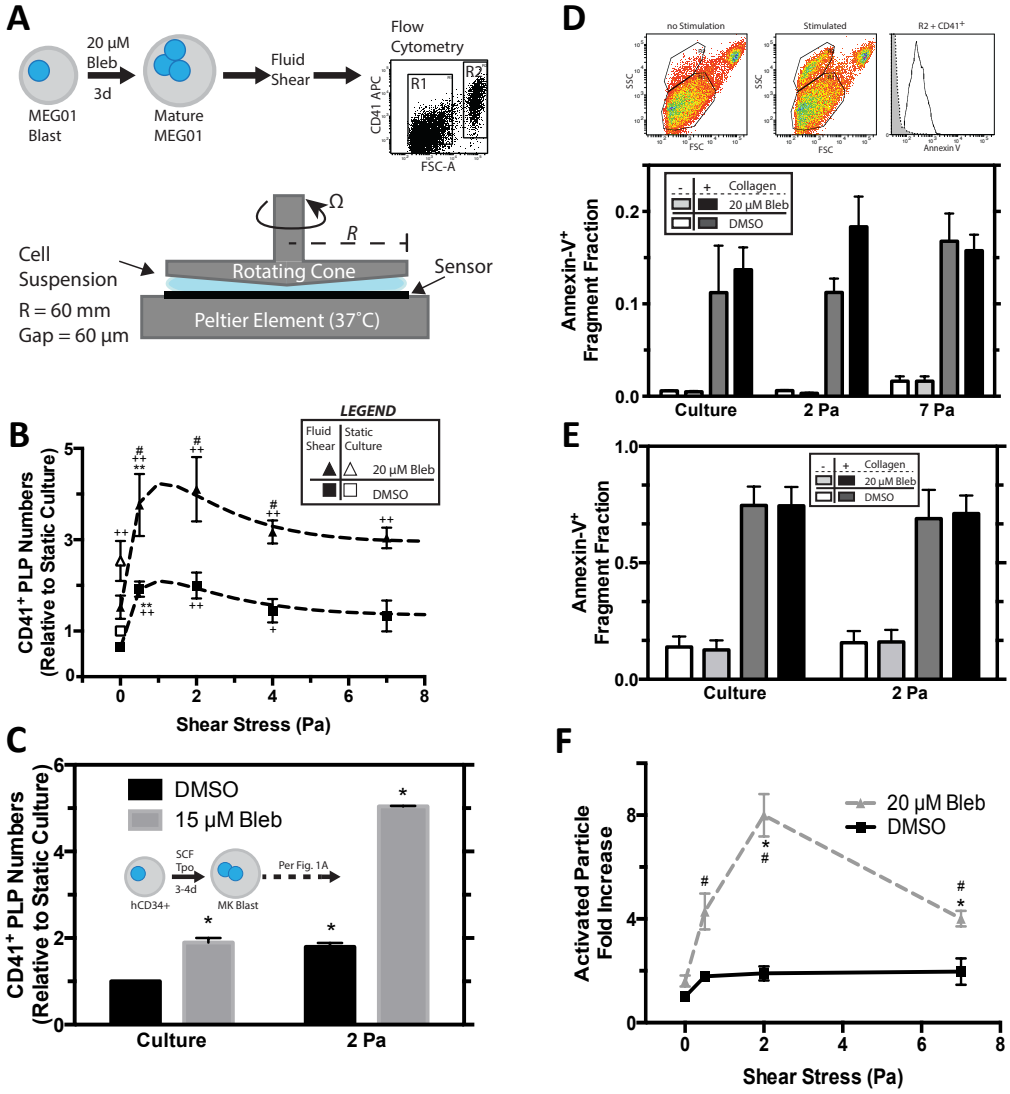

Figure 3.1 Shear stress and pharmacological inhibition of myosin synergistically enhance platelet-like-particle generation *in vitro*

(**A**) Myosin inhibition scheme and schematic of cone and plate rheometer. MEG-01 cells were cultured for 3 days with 20 μM blebbistatin ($IC_{50} \approx 5$ μM). PLP generation is assayed on the third day of culture. Cell suspensions placed on the rheometer are subjected to controlled temperature, shear stress, stress duration, and gap size. Samples collected from the rheometer are analyzed by flow cytometry to quantify PLP (R1) and nucleated cell (R2) fractions. (**B**) Quantitation of PLP generation following cone and plate imparted shear stress (n=6, ±SEM, *, +, # $P<0.05$, **, ++ $P<0.005$. + significant from DMSO culture, # significant from blebbistatin culture, * significant from previous shear stress condition). The data is fit with a combination of a one phase exponential decay and a one site-specific binding model. DMSO fit: y=[2+4.0*exp(-0.62*x)]*[0.10+(0.66/(0.65+x))], R^2=0.97). Bleb fit: y=[2+4.0*exp(-0.62*x)]*[0.26+(1.5x/(0.94+x))], R^2=0.98). (**C**) Primary human $CD34^+$ bone marrow derived cells were cultured for 3-4 days in the presence of SCF and Tpo to drive differentiation towards MKs followed by an additional 3 days of culture in the presence of 15 μM blebbistatin to promote polyploidy and MK maturation. PLP generation is quantified following cone and plate rheometry. Values are relative to unsheared, untreated cell culture (n=3, ±SEM, * $P<0.05$). (**D**) MEG-01 cell suspension stimulated by 100 μg/mL collagen-I and 1 mM $CaCl_2$. Activation determined by shift in side scatter and Annexin-V^+CD41^+. Stimulation activates up to ~12% of unsheared PLPs, and ~12-20% of shear generated PLPs (n=3, ±SEM). (**E**) Primary human MKs stimulated with collagen, similar to in panel D, following cone and plate imparted shear stress (n=2,

±SEM). (**F**) Considering the increased number of PLPs generated from shear panel B, shear results in an ~8x net increase in functional PLPs compared to unsheared, untreated MEG-01 from culture (n=5, ±SEM, *, + $P<0.05$. # significant from untreated condition, * significant from previous shear stress condition).

Figure 3.2 Shear stress modulates megakaryocyte myosin activity

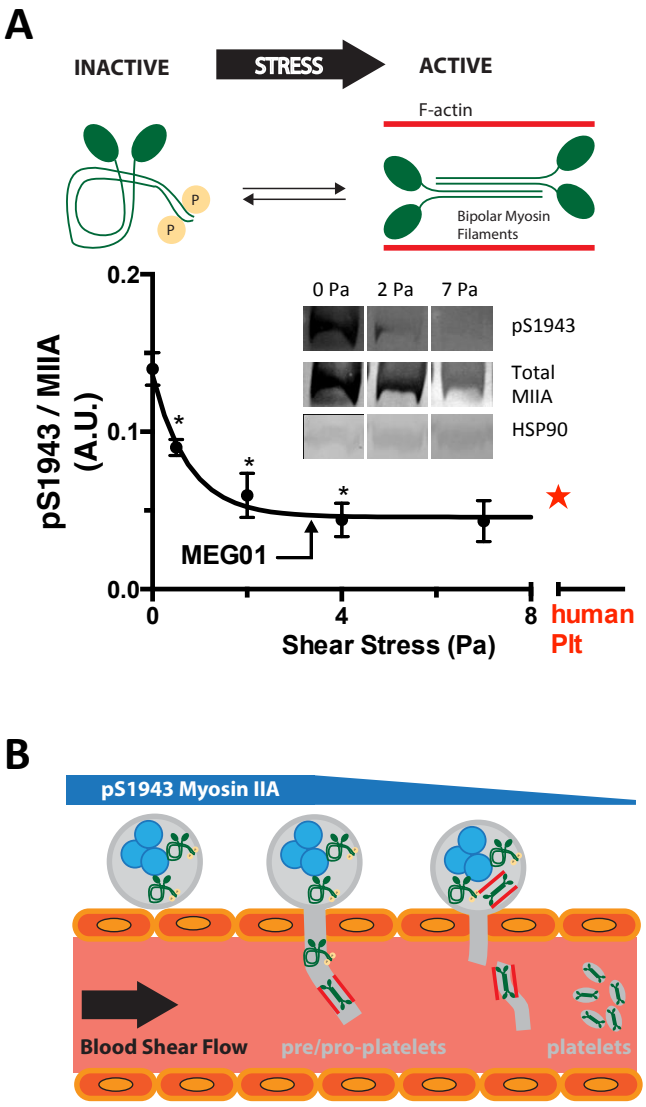

Figure 3.2 Shear stress modulates megakaryocyte myosin activity

(**A**) Cartoon of the location of S1943, the site examined in this work and implicated in MII filament formation. S1943 phosphorylation leads to MIIA inhibition and less contractile cells. Quantification of MEG-01 pS1943 shows shear dependence. After shear, cells are collected, fixed, permeabilized, and stained for analysis by flow cytometry (n=4, ±SEM). The fit is: $y=0.046+0.093*\exp(-1.32x)$ ($R^2=0.98$, $*P<0.05$). The star is quantification resulting from flow cytometry of resting fresh human platelets. (**A**, **inset**) Western blot shows agreement with flow data. Namely, phosphorylation of non-muscle MIIA S1943 decreases in a shear stress dependent manner. Original blot was cropped to economize figure size. No further manipulation was performed. (**B**) High ploidy mature megakaryocytes transmigrate to the perivascular niche where they extend membrane extensions into the vasculature. These extensions are then fragmented by shear imparted by the blood flow. While these initial fragments may be large in size and heterogeneous in size distribution additional exposure to blood flow fragments these further to normal sized human platelets. This process is dependent on MII activity, which is sensitive to shear stress through phosphorylation of S1943.

Figure 3.3 Myosin IIA inhibition is necessary to generate fragments similar in size to normal human platelets from *in vitro* micropipette aspiration

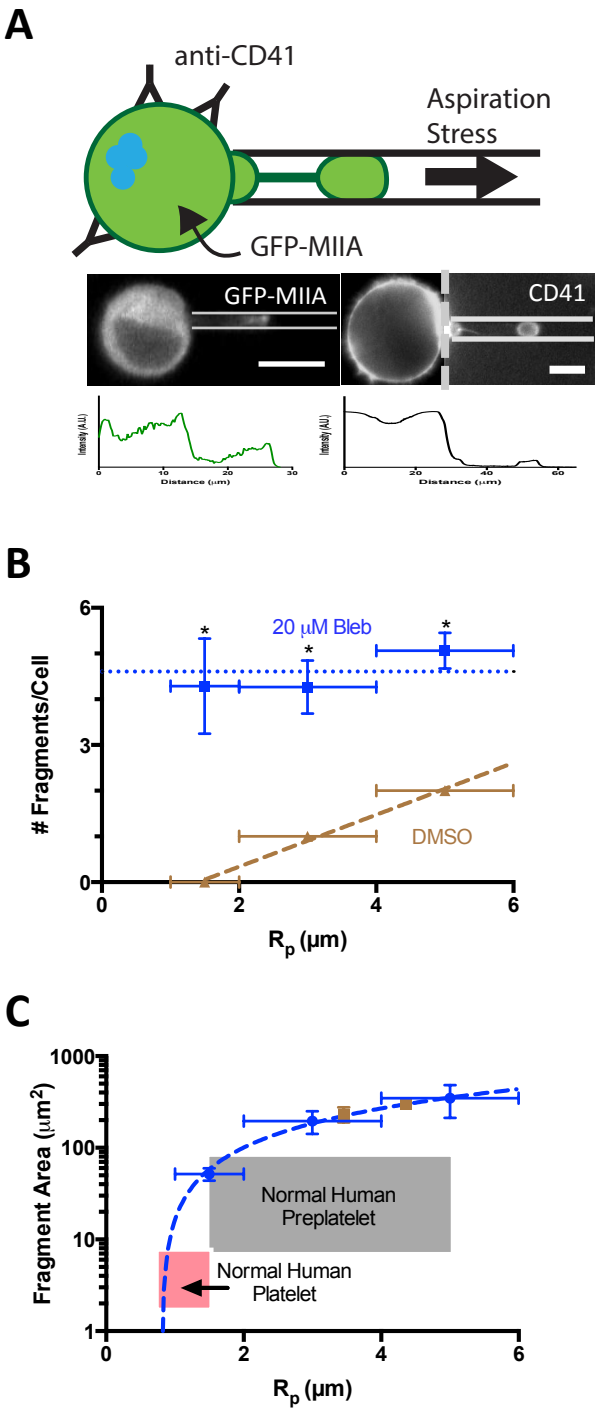

Figure 3.3 Myosin IIA inhibition is necessary to generate fragments similar in size to normal human platelets from *in vitro* micropipette aspiration

(**A**) MEG-01 cells are nucleofected with GFP-MIIA or else labeled with fluorescent anti-CD41. Representative fluorescent images of GFP-MIIA or else CD41-PE labeled MEG-01 undergoing fragmentation induced by micropipette aspiration (scale bar = 5 μm). Intensity of cell body has been adjusted to aid in visualization of aspirated fragment. True intensity of the CD41 labeled MEG-01 is plotted below micrograph. (**B**) Blebbistatin treatment increases the number of fragments per cell as well as permission of fragmentation at smaller radius pipettes. Shaded region indicates range of reported normal human platelet size. Linear fit of DMSO: $y=0.57x-0.8$, $R^2=0.99$, n=2, ±SEM. 20 μM blebbistatin: n>15, ±SEM. Statistical significance determined between DMSO and 20 μM blebbistatin for a given R_p, *P<0.05. (**C**) Fragment area is not affected by blebbistatin; however, blebbistatin treatment facilitates fragmentation of smaller fragments from smaller radius pipettes. Linear fit of 20 μM blebbistatin: $y=138x-187$ ($R^2=0.99$, n<40, ±SEM). DMSO: n>6, ±SEM. Pink shaded region denotes calculated range of area from reported normal human platelet diameters. Gray shaded region denotes estimations from reported preplatelet diameters (Thon et al., 2012).

Figure 3.4 Characterization of abnormalities in *MYH9*-RD patient platelets

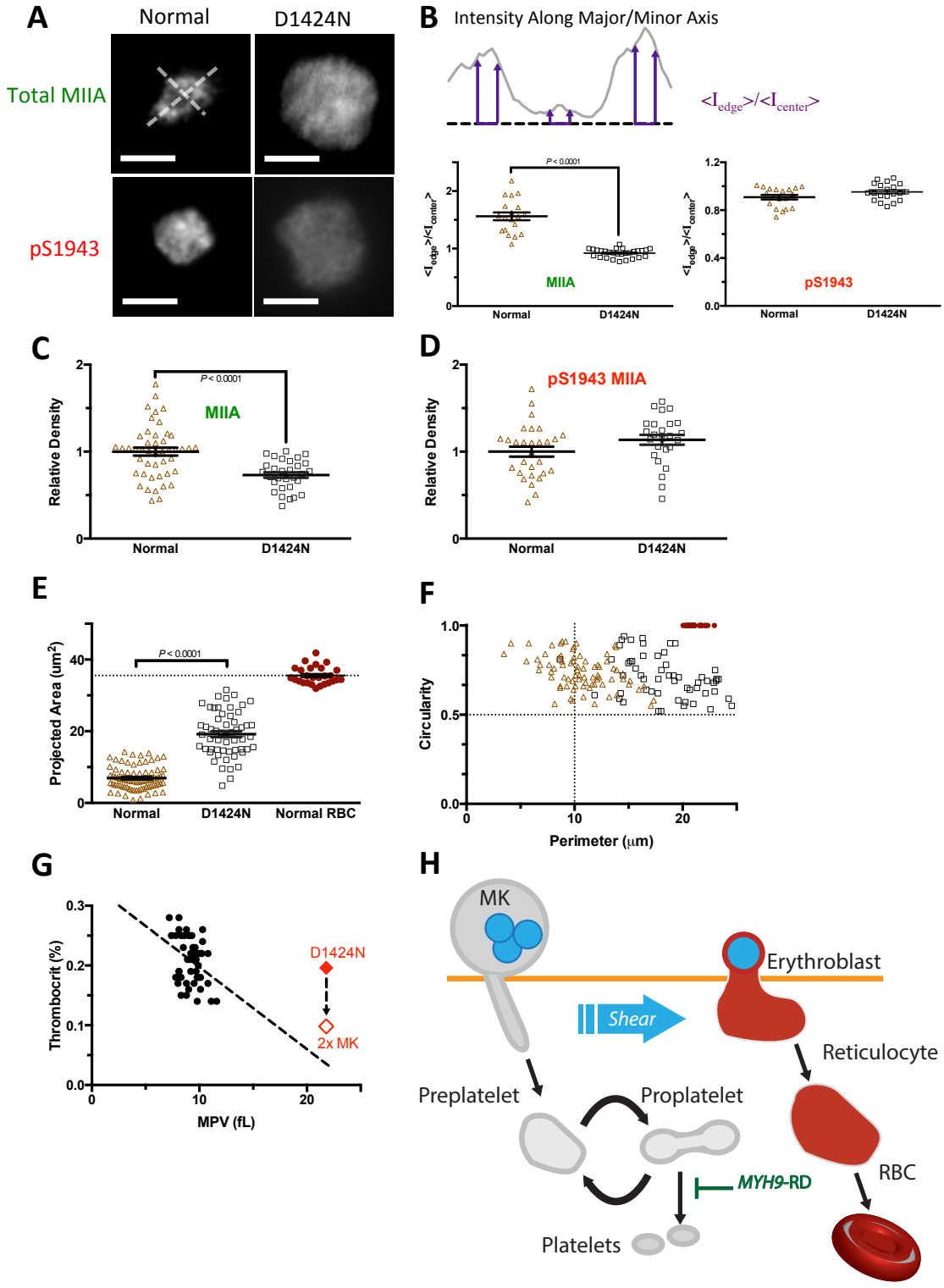

Figure 3.4 Characterization of abnormalities in *MYH9*-RD patient platelets

(**A**) Peripheral blood was obtained from a patient expressing the c.4270G>A (D1424N) *MYH9*-RD mutation was collected in EDTA. Buffy coat was incubated with CD41-APC, total or pS1943 MIIA antibodies, and Hoescht 33342. Platelets were identified as $CD41^{+}Hoescht^{-}$ expression (scale bar = 5 μm). (**B**) Peripheral MIIA is disrupted in platelets containing the *MYH9*-RD mutation. Intensity line scans were made along perpendicular major and minor axes as shown in (A). Myosin distribution is quantified by the ratio of average peripheral intensity to average center intensity. Total MIIA is peripheral in normal platelets while diffuse in mutant platelets while phospho-MIIA is diffuse in both cases. *MYH9*-RD mutation results in a decrease in total MIIA (**C**) but not pS1943 MIIA expression (**D**). (**E**) Patient platelets show an increase in projected area. (**F**) *MYH9*-RD mutation has a dramatic effect on observed platelet shape. (Normal: n=83; D1424: n=78; RBC: n=32). Red blood cells from a normal donor were used as an internal calibration control for size and shape in E and F. (**G**) Thrombocrit values calculated from MPV and platelet count data published in Thompson Blood 1988 show a weak dependence on MPV (Linear Regression: Thrombocrit = -0.01 * MPV + 0.33, R^2=0.12, n=49) (Thompson and Jakubowski, 1988). The red diamond is the value for the D1424N patient used throughout this paper. Assuming a compensatory mechanism of increased MK number as demonstrated in mouse, (Zhang et al., 2012) the *MYH9*-RD patients thrombocrit could fit the trend of normal thrombocrit. (**H**) Proposed model of platelet generation accounting for *MYH9*-RD induced macrothrombocytopenia. MK shedding of preplatelets is an analogous process to erythroblast enucleation. The circulating reticulocyte becomes a terminal RBC through the aid of hydrodynamic shear

force, however the absence of MIIA prevents further fission events. Similarly, the blood shear forces assist the transition from preplatelet to proplatelet, but the presence of MIIA allows for cleavage furrow formation and fission resulting in normal platelets. *MYH9*-RD mutations abrogate normal MIIA activity preventing cleavage furrow formation and platelet fission. This results in an increase in circulating preplatelets and the phenotypic large platelets.

Figure 3.5 Myosin localization and MK fragmentation altered by *MYH9*-RD

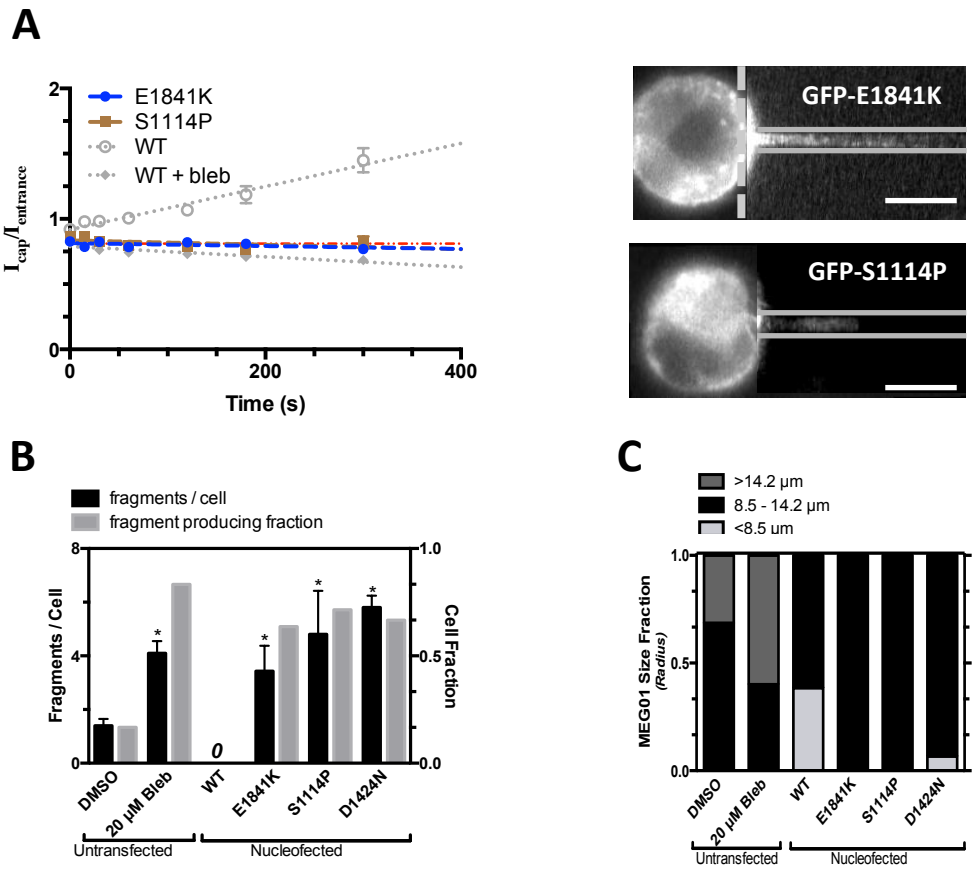

Figure 3.5 Myosin localization and MK fragmentation altered by *MYH9*-RD

GFP-MIIA mutation associated with *MYH9*-RD, S1114P, D1424N, or E1841K specifically, were introduced into MEG-01 cells. (**A**) Upon application of stress, GFP-MIIA is seen evenly distributed throughout the aspirated length in a manner similar to either S1943D MIIA or blebbistatin treated cells (gray dotted line). S1114P: ($y=1.7*10^{-4}x+0.84$, $R^2=0.26$, n=6, ±SEM). E1841K: ($y=1.1*10^{-4}x+0.81$, $R^2=0.27$, n=10, ±SEM). Representative fluorescent micrographs showing uniform GFP distribution from a GFP-E1841K MIIA and fragment shedding from a GFP-S1114P mutant (scale bar = 5 μm). (**B**) These cells showed an enhanced propensity to produce fragments similar to that of blebbistatin treatment (n>8, ±SEM, *P<0.05, significant from untransfected-DMSO). (**C**) Quantification of MEG-01 size for each of the cell types used for micropipette aspiration. The *MYH9*-RD mutant cells, which produced fragments, show a higher distribution of larger cells compared to the phospho-mutants that did not fragment.

Figure 3.6 Myosin IIA activity controls conversion to proplatelets and cleavage of normal platelets

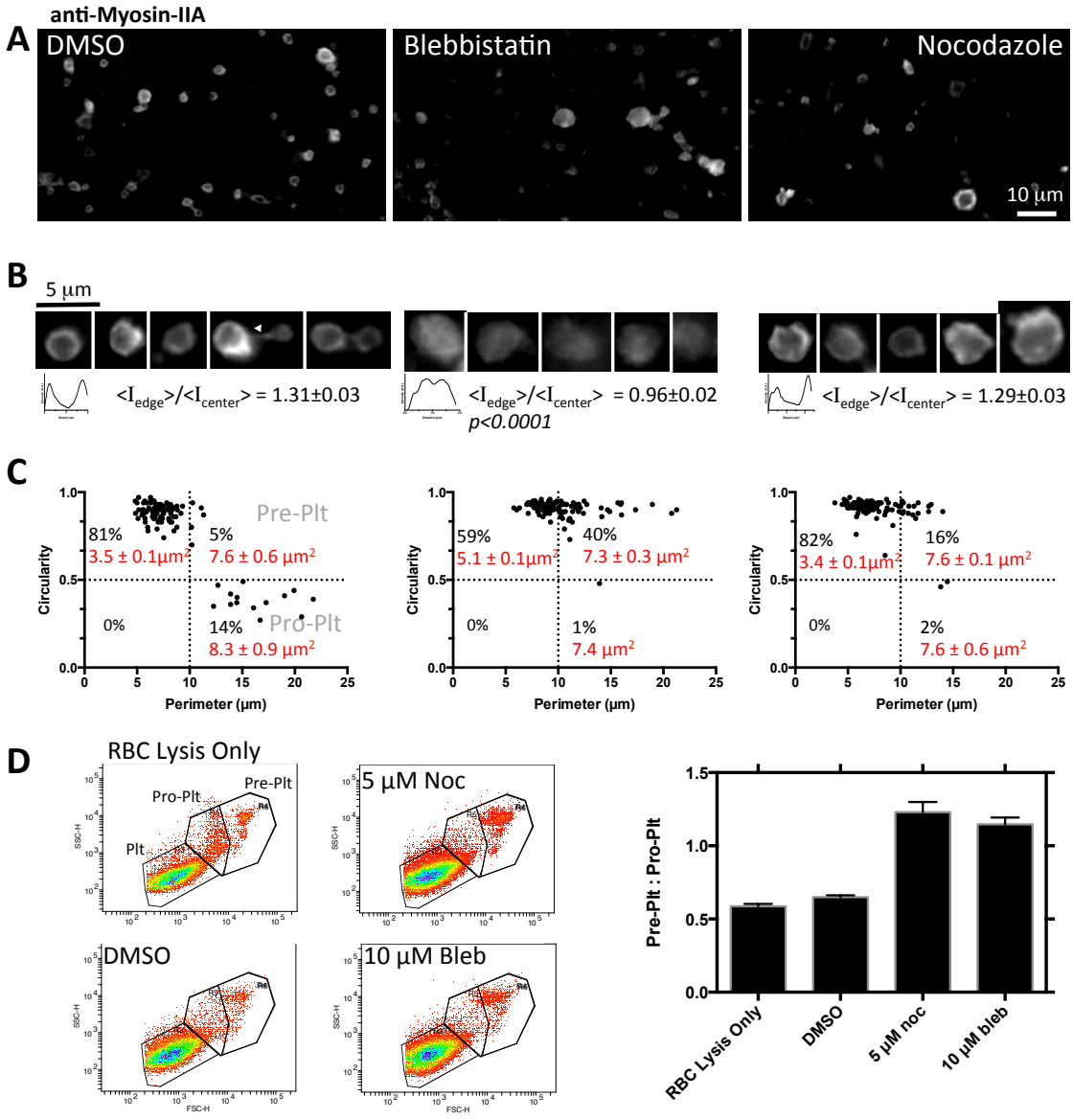

Figure 3.6 Myosin IIA activity controls conversion to proplatelets and cleavage of normal platelets

Proplatelet-enriched fractions from PB collected in AJ buffer were incubated with DMSO, 10 μM blebbistatin, or 5 μM nocodazole for 6 hours at 37°C. (**A**) Representative images of cultures after drug treatment. (**B**) High magnification (240x) of culture presented in (A) to demonstrate MIIA distribution and morphology after each treatment. Line scans and surface plots demonstrate MII localization at the periphery observed for DMSO and nocodazole treatment is disrupted by blebbistatin treatment. Staining for MIIB was done in parallel using the same secondary antibody, which indicated intensity/area, on average, MIIA:MIIB=250 (N=25 across 5 fields of view each isoform). (**C**) Quantification of immunofluorescence of 6 hr treated proplatelet-enriched fractions shows a shift toward preplatelets at the expense of proplatelets following blebbistatin or nocodazole incubation. 1 hr treatments were done in parallel. Population breakdown enumerated in black font, mean±SEM population projected area in red font. Gates are set based on previously published values (Thon et al., 2012). (**D**) Representative flow cytometry scatter plots. Platelet populations were determined based on scatter, then gated on $CD41^+$, $Hoescht^-$, GPA^-. Results of flow cytometry analyses.

3.4 DISCUSSION

The results here first suggest that normal MKs suppress MIIA activity via tail phosphorylation (pS1943) to increase ploidy and to be sufficiently pliable to fragment readily under shear as is relevant to pre-/pro-platelet generation (Fig. 3.2B). Secondly, the results suggest that *MYH9*-RD mutations (at least in the tail) likewise favor pliability and fragmentation, but the re-activation of MIIA that normally occurs in human platelets is insufficient for *MYH9*-RD pre-/pro-platelets. For normal pre-/pro-platelets, this re-activation drives fission to small and abundant normal platelets but *MYH9*-RD pre-/pro-platelets do not (Fig. 3.4H). Evidently, flow stresses are optimized (Fig. 3.1) for initial fragmentation of MK projections *in vivo* (Junt et al., 2007), but flow stresses do not fragment pre-/pro-platelets, which is a process made efficient in normals by MIIA-mediated cyto-fission.

The results thus provide a novel outside-in regulatory mechanism for thrombopoiesis. While MIIA activity has already been established as a negative regulator of platelet generation (Chen et al., 2007), MIIA exhibits more regulated activity. Specifically, shear stress provides the external cue that impacts MII activity by reducing MIIA phosphorylation at S1943. Exposure to high stress activates MIIA locally (Fig. 3.S3), which leads to a tensed and stiff cell that is much less likely to fragment in micropipette aspiration (Fig. 3B, 5B). Inhibition of MIIA softens the membrane to favor fragmentation to sizes similar to normal human pre-/pro-platelets (Fig. 3.3B). Altogether the results suggest kinetics that strikes a balance between MK fragmentation and MK contractility. If MK proplatelet processes were to grow abnormally long and spend too much time extended into the vasculature prior to fragmentation, then the proplatelets will

likely have heterogeneous protein distributions (especially mechanosenstive MII) and therefore have variable function.

Previous work demonstrated that microtubule stabilization or destabilization by taxol or nocodazole respectively favors proplatelets or preplatelets (Thon et al., 2012). However, tubulin expression is not affected by the *MYH9*-RD mutation D1424N (Deutsch et al., 2003). The formation of a cleavage furrow and the lack of proplatelets in this *MYH9*-RD mutant sample suggest roles for MIIA in facilitating pre-/pro-platelet transition as well as cytofission. Combined with the noted fragmentability of the MEG-01 cells expressing the *MYH9*-RD mutants, macrothrombocytopenia is understandable in spite of the reasonable PB thrombocrit (Fig. 3.4G). Eckly *et al*. likewise reported in lineage-specific *Myh9* knockout mice a higher percentage of MKs that extend proplatelets which were also larger than normal MKs despite a cytopenia in the knockout mice (Eckly et al., 2009). Furthermore, Zhang *et al*.'s transgenic mice expressing D1424N or E1841K mutations exhibit macrothrombocytopenia and a slight elevation in peripheral thrombocrit (Zhang et al., 2012). Our results support these data and provide credence to a model wherein switchable MIIA activity is critical to normal platelet biogenesis.

In summary, this seems the first study to demonstrate a regulated synergy between MIIA activity and shear stress in platelet generation in both normal and *MYH9*-RD. Importantly, shear stress enhances MIIA activity by reduction of phosphorylation of S1943. The detailed outside-in signal has yet to be elucidated, but MK fragment size and fragment number are clearly enhanced by repressing MII activity. Subsequently, MIIA activity is critical to the transition from preplatelet to proplatelet with cleavage furrow

ingression and cytofission to platelets. This process is necessary for production of normal sized platelets and is disrupted by either pharmacological inhibition with blebbistatin or *MYH9*-RD mutation. Previous work on MK lines (Apostolidis et al., 2012) has also shown *MYH9* to be downstream of the p53 that seems normally repressed to permit ploidy; indeed, p53 knockdown downregulates *MYH9, ACTA2, and FLNA* all of which are cytoskeletal contributors to actomyosin forces. Platelet size abnormalities might thus result from p53 defects. Myosin-II activity in early MKs with and without *MYH9*-RD mutation could also be very different, as suggested by studies of MK adhesion forces (Chen et al., 2013) and from the fact that MIIB is high normally in early MKs but dysregulated in some diseases (Bluteau et al., 2012; Shin et al., 2014). Furthering our work with pharmacological MII inhibition using blebbistatin, perhaps an intravital microscopy study of *Myh9* conditional knockout mice could further elucidate the critical role of MIIA in proplatelet fission *in vivo*. The present results suggest a spatio-temporal mechanism of platelet production, which ties together mechano-responsive MK contractility and fragmentation, and most strikingly, preplatelet to proplatelet conversion followed by proplatelet fission.

Table 3.S1. List of antibodies used in Chapter 3 Methods

Experiment	Buffer	Antibody	Dye/ Conjugate	Time (min)/ Temp (°C)	Dilution	Manufacturer
Rheometry & PLP Generation	Tyrode's + PGE1 (1:1000)	-	7-AAD	60 / 20	1:1000	Sigma
		-	Hoescht 33342	60 / 37	1:2500	Invitrogen
		anti-hu CD41	APC	60 / 37	1:20	Biolegend
		pS1943 MIIA	-	120 / 20	1:100	Cell Signaling
		anti-hu MIIA	-	120 / 20	1:100	Cell Signaling
		donkey anti-rb	Alexa 488	60 / 20	1:400	Invitrogen
Functional Characterization of MEG-01 Derived PLPs	Tyrode's + PGE1 (1:1000) + Ca^{2+} (1mM)	-	7-AAD	60 / 20	1:1000	Sigma
		anti-hu CD41	APC	60 / 37	1:20	Biolegend
		Annexin V	PE	60 / 20	1:10	BD Biosciences
Micropipette Aspiration	1% BSA	-	Hoescht 33342	45 / 37	1:1000	Invitrogen
		anti-hu CD41	PE	45 / 37	1:10	eBioscience
Proplatelet Imaging	3% BSA + 0.05% Tween-20	pS1943 MIIA	-	4 / ~16	1:100	Cell Signaling
		anti-hu MIIA	-	4 / ~16	1:100	Cell Signaling
		anti-hu MIIB	-	4 / ~16	1:100	Sigma
		donkey anti-rb	Alexa 488	60 / 20	1:400	Invitrogen
		anti-hu CD41	APC	60 / 20	1:100	Biolegend
		-	Hoescht 33342	5 / 20	1:10000	Invitrogen
Proplatelet Flow Cytometry	Tyrode's	anti-hu CD41	APC	45 / 20	1:20	Biolegend
		Glycophorin A	PE	45 / 20	1:20	Biolegend
		-	Hoescht 33342	45 / 20	1:2500	Invitrogen

Table 3.S1. List of antibodies used in Chapter 3 Methods

Description of antibodies and incubation protocols employed for the noted experiments.

Figure 3.S1. Pharmacological inhibition of myosin increases megakaryocyte ploidy

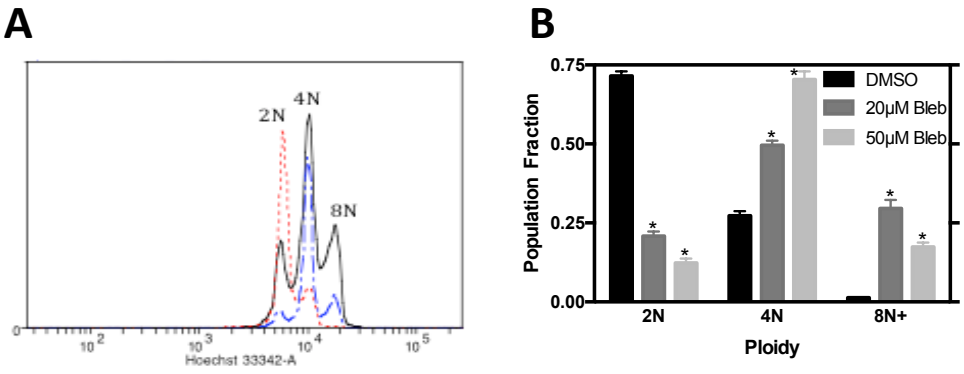

Figure 3.S1. Pharmacological inhibition of myosin increases megakaryocyte ploidy

(**A**) Increased ploidy of MEG-01 cells by blebbistatin treatment. Cells were treated with DMSO, 20 μM, or 50 μM blebbistatin for 72 hrs followed by staining with Hoescht 33342 and analysis by flow cytometry. Raw data *(left)* is characterized by the histogram *(right)*. Blebbistatin results in ~3 fold increase in 4n cells and >20 fold increase in higher ploidy (≥8n) cells (n=15, *P<0.005). Since MII activities affect cytokinesis, we proposed a scheme in which MII inhibition by blebbistatin would increase higher ploidy MKs. When MEG-01 cells were treated with blebbistatin for 72 hours we observed 4N and ≥8N populations increased at the expense of the 2N population without effecting total MK numbers in a dose dependent manner as seen by flow cytometry (Figure S1A). Quantitatively, 4N populations increased ~3-fold while 8N populations increased >20 fold (Figure 3.S1B). These results are in agreement with those we previously shown with blebbistatin treatment of $CD34^+$ derived cultures (Shin, 2011).

Figure 3.S2. Phosphorylation of resting fresh human platelets

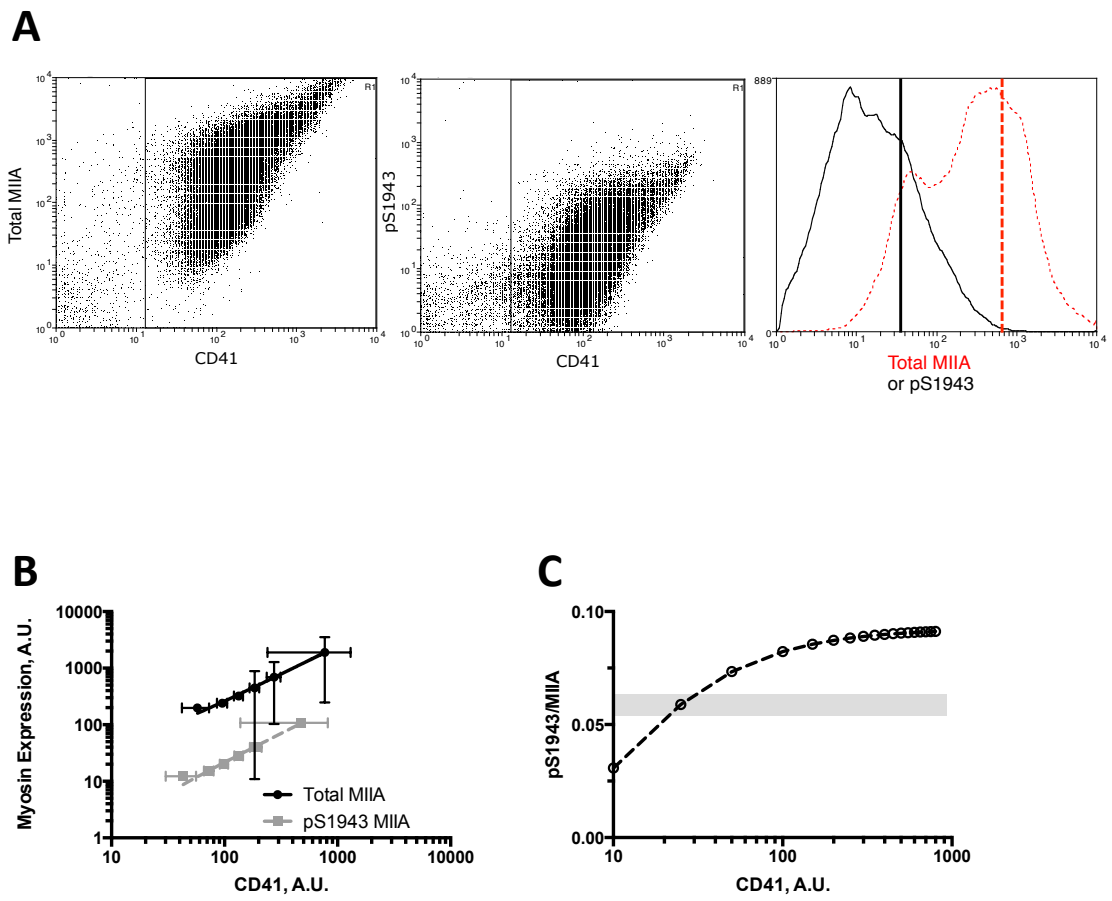

Figure 3.S2. Phosphorylation of resting fresh human platelets

(**A**) Fresh human platelets were analyzed with flow cytometry and gated on CD41 for either total MIIA (*left*), or pS1943 MIIA (*middle*). The histogram illustrates the resultant distribution of total MIIA or pS1943 MIIA and the mean of each distribution is captured by the vertical lines (A, *right*). (**B**) Individual events were analyzed. Bins were created to include equal number of events per bin. The linear fit of total MIIA: $y=2.4x+19$, $R^2=0.99$. Linear fit of pS1943 MIIA: $y=0.2x-0.9$, $R^2=0.99$. (**C**) The ratio of pS1943 to total MIIA was calculated by dividing the linear fits from panel B. The fit: $y=[0.1x/(8+x)]-0.05$, $R^2=0.99$, $\langle pS1943/MIIA \rangle = 0.06$.

Figure 3.S3. MIIA activity impacts localization and MEG-01 membrane stiffness

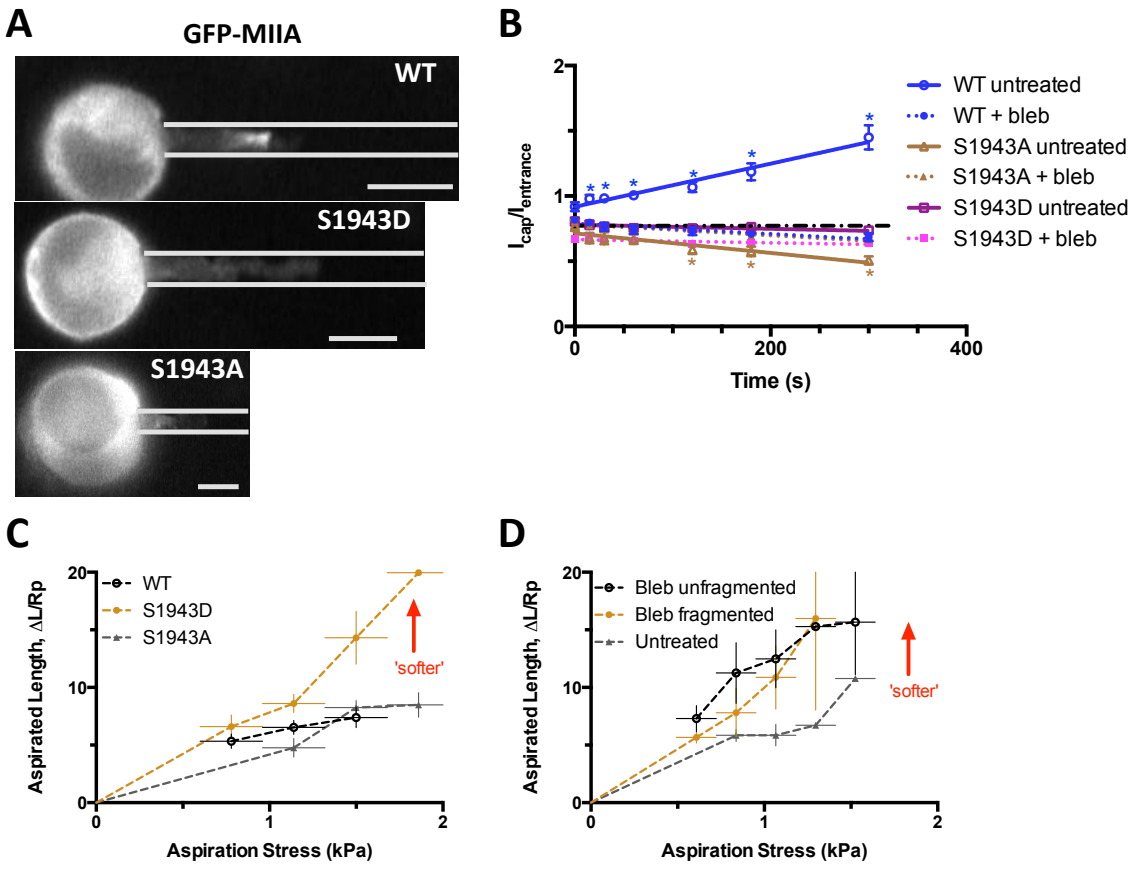

Figure 3.S3. MIIA activity impacts localization and MEG-01 membrane stiffness

(**A**) Representative fluorescent micrographs of nucleofected MEG-01 cells during micropipette aspiration. All scale bars = 10 μm. GFP-WT MIIA shows accumulation at the tip, GFP-S1943D MIIA shows uniform distribution along the aspirated length, GFP-S1943A MIIA shows depletion at the tip. (**B**) Treatment with blebbistatin recovers a uniform distribution regardless of construct ($n>10$, ±SEM, $^*P<0.05$, statistical significance determined between ±blebbistatin for a given construct at a given time point). (**C**) MEG-01 membrane stiffness is affected by introduction of GFP tagged MIIA constructs by nucleofection. Cells phosphomimetic introduced with the phosphomimetic S1943D mutant show a similar membrane softening as is seen by pharmacological treatment of untransfected cells with blebbistatin (**D**) ($N>25$ cells, ±SEM).

Figure 3.S4. Effect of *MYH9*-RD on fragmentation size

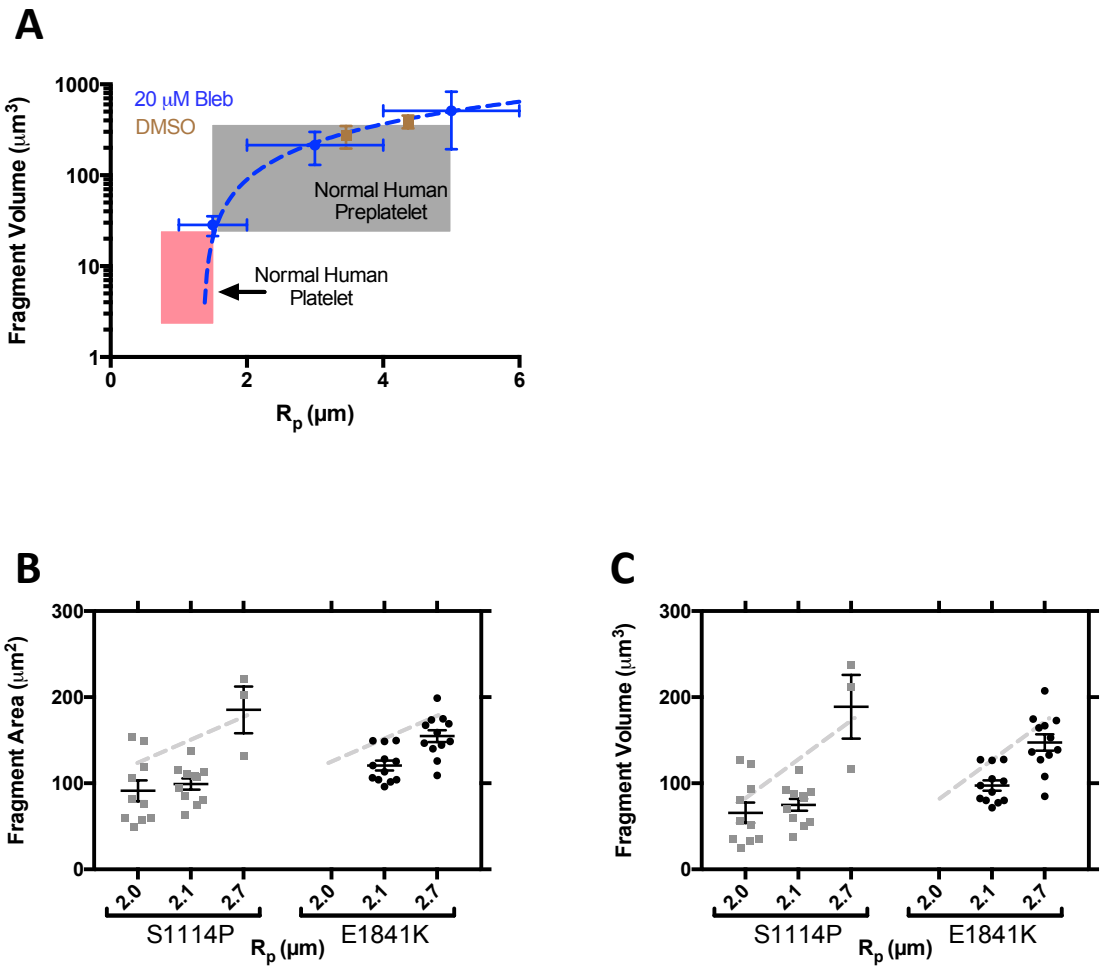

Figure 3.S4. Effect of *MYH9*-RD on fragmentation size

(**A**) Fragment volume is not affected by blebbistatin; however, blebbistatin treatment facilitates fragmentation of smaller fragments from smaller radius pipettes. Pink shaded region denotes calculated range of volume from reported normal human platelet diameters. Gray shaded region denotes calculated range of volume from reported preplatelet diameters (Thon et al., 2012). Both shaded regions calculated using reported diameters and assuming ellipsoid shape. Linear fit of 20 μM Blebbistatin: y=84x-68 (R^2=0.9956, n<40, ±SEM). DMSO: n>6, ±SEM. (B) Fragmentation of MEG-01 cells following introduction of either S1114P or E1841K GFP-MIIA. *MYH9*-RD mutation does not significantly impact either fragment area (**B**) nor fragment volume (**C**) compared to DMSO treated MEG-01 (dashed line) (N≥10, ±SEM).

Figure 3.S5. Visualization of *MYH9*-RD induced myosin aggregates

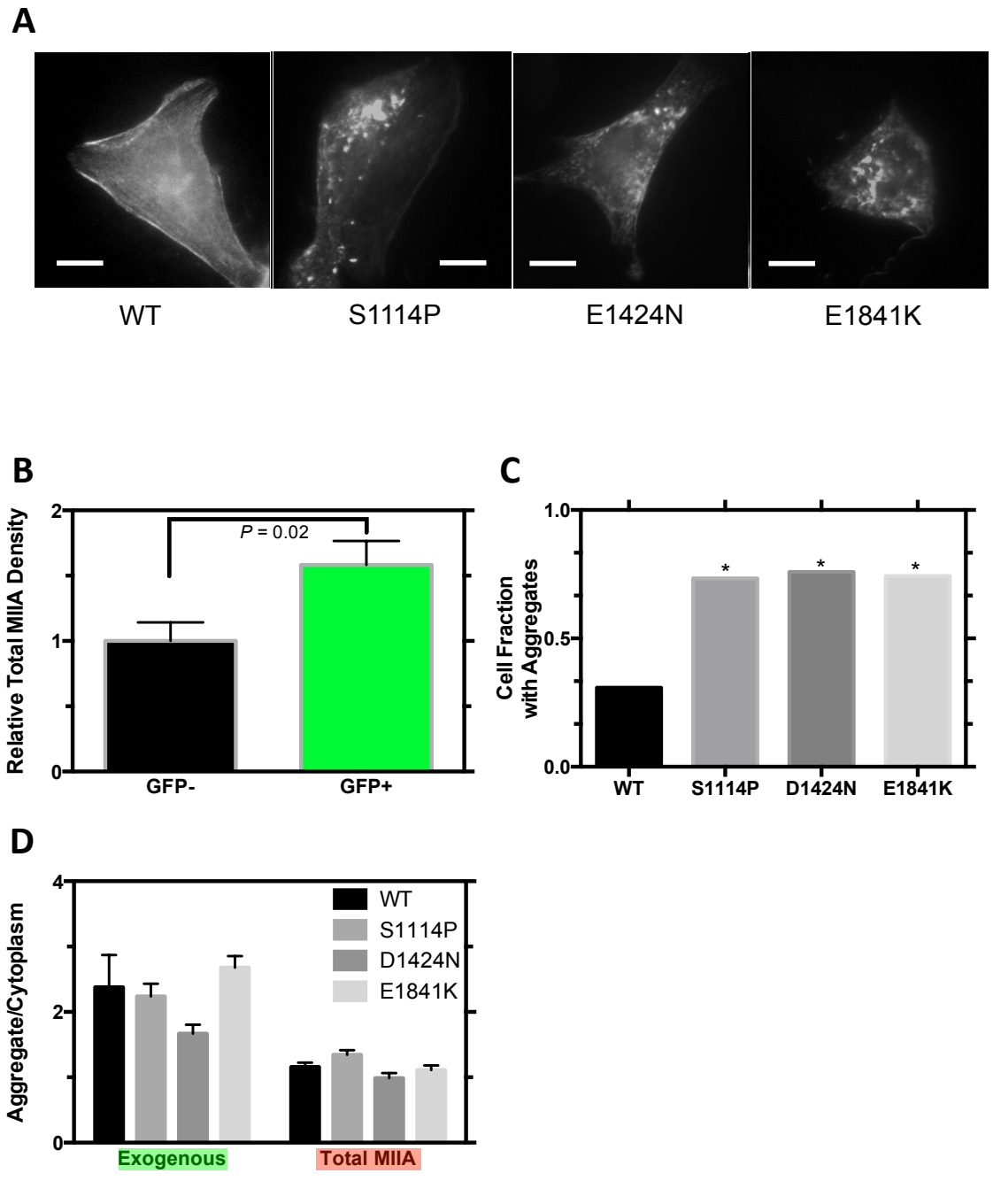

Figure 3.S5. Visualization of *MYH9*-RD induced myosin aggregates

(**A**) Nucleofection was used to introduce GFP-MIIA constructs in A549 cells. These cells were used for imaging instead of spherical MEG-01 because the highly adherent A549 cells are generally well spread and thus easier to focus on all aggregates for quantitation. Immunofluorescence reveals abnormal MII aggregates that are enriched in exogenous MII compared to surrounding cytoplasm (scale bar = 10 μm). (**B**) Total MIIA overexpression in GFP^+ is ~1.7x relative to GFP^- cells (N=15, ±SEM). (**C**) Quantitation of cells displaying MII aggregates (N≥30, *P<0.05). (**D**) Exogenous MII is seen to accumulate in aggregates compared to the surrounding cytoplasm while total MII (exogenous + endogenous) is similarly present in both aggregates and cytoplasm (N≥65, ±SEM, *P<0.05).

CHAPTER 4: IgG TREATMENT TO STIMULATE PHAGOCYTOSIS OF CD47^{LOW} SOLID TUMORS

This chapter represents work included in the manuscript – Selective phagocytosis of CD47^{low} human cells in solid tumors following systemic injection of anti-human IgGs. (Spinler KR, Tewari M, Athirasala A, Nair P, and Discher DE. 2014, in preparation).

Manorama Tewari and Avathamsa Athirasala both contributed to cell line generation. Praful Nair generated paclitaxel loaded polymer worms and assayed *in vitro* cytotoxicity.

ABSTRACT

CD47 is expressed to varying extent on all viable human cells and interacts with phagocytes to provide a "don't eat me" signal that is now being explored in numerous cancer contexts. We studied human-CD47 (hCD47) knockdown cells that stably express tdTomato in solid tumor xenografts in NSG mice. NSG macrophages are known to recognize hCD47 as 'self'. While partial knockdown had no effect on tumor growth, deep knockdown increased growth except when knockdown cells were grafted as mosaic tumors with a minor fraction of wildtype GFP^+ tumor cells. All tumors containing knockdown cells shrunk significantly after systemic injection of IgG that was broadly generated against human molecules. Importantly, IgG treatments selectively cleared knockdown cells based on flow cytometry analyses of excised tumors. When treatment was stopped, tumors re-grew unless treated again. Shrinkage proved similar in kinetics and extent to that achieved with paclitaxel chemotherapy, and co-administration of IgG and drug showed little to no synergy. Injected antibody did not cause significant anemia, thrombocytopenia, nor weight loss, and levels of hCD47 on tumor periphery or core subpopulations were unaffected. While injected IgG was detected on both human and mouse cells from the tumors – including macrophages – circulating cells were not opsonized. Importantly, a significant fraction of the IgG^+ macrophages from hCD47-knockdown tumors were also $tdTomato^+$, consistent with phagocytosis of tumor cells or fragments. Besides implications for therapy, the results suggest a selective pressure against $hCD47^{low}$ cells that could account for the oft-reported upregulation of hCD47 in cancer.

3.1 INTRODUCTION

CD47 is a cell surface glycoprotein that was originally described as a highly expressed ovarian carcinoma antigen (OA3) (Campbell et al., 1992). It is now known to interact with SIRPα on phagocytes to provide a "don't eat me" signal and thus act as a "marker of self" (Oldenborg, 2000). The CD47-SIRPα interaction leads to tyrosine phosphatase activation and inhibition of MII accumulation at the phagocytic synapse (Tsai and Discher, 2008). Red blood cells (RBCs) from CD47 knockout mice injected into control mice are cleared within hours by macrophages compared to weeks for normal RBCs (Oldenborg, 2000). Conversely, we have recently demonstrated that a minimal peptide designed from human CD47 delays phagocytic-mediated clearance from murine circulation when attached to a range of nanosized particles (Rodriguez et al., 2013). Macrophages from non-obese diabetic/severe combined immunodeficient (NOD/SCID) mouse strains express a SIRPα variant that is capable of cross-reacting with human CD47. This cross-reactivity explains the success of human hematopoietic grafts in such mice compared to other strains (Strowig et al., 2011; Takenaka et al., 2007). While CD47 is nearly ubiquitously expressed on human cells (Reinhold et al., 1995), it has shown to be expressed at elevated levels in circulating stem cells (Jaiswal et al., 2009), liquid (Chao et al., 2010a, 2011a; Majeti et al., 2009), and solid tumors (Willingham et al., 2012). In fact, increased CD47 mRNA expression has shown a correlation with a poor clinical prognosis in patients with acute myeloid leukemia (AML), non-Hodgkin's lymphoma (NHL) (Chao et al., 2010a; Majeti et al., 2009), ovarian cancer, gliomas, and glioblastomas (Willingham et al., 2012).

Targeting the CD47-SIRPα pathway has currently been an active area of research. Murine models of leukemias (Chao et al., 2010a, 2011a; Majeti et al., 2009), myeloma (Kikuchi et al., 2005), and breast cancer (Manna and Frazier, 2004) have been successfully treated with anti-CD47 antibody. Since CD47 is expressed on nearly all cells, any treatment that involves an anti-CD47 antibody will not only opsonize cancer cells, but normal cells as well. Despite the potential for adverse side effects, mice engrafted with AML leukemic stem cells and treated with anti-CD47 (B6H12) antibody showed selective elimination of AML cells while sparing normal stem cells and did not show any abnormality in blood counts other than a slight neutropenia (Majeti et al., 2009). Other CD47 targeting strategies have used liposome-protamine-hyaluronic acid (LPH) nanoparticles loaded with siRNA against CD47 (LPH(CD47)) to inhibit tumor growth and metastasis without hematopoietic toxicity (Wang et al., 2013). Use of liposomal clodronate to deplete macrophages resulted in significant diminishing of treatment efficacy implicating phagocytosis by macrophages as the process of tumor clearance in each of the preceding methods (Majeti et al., 2009; Wang et al., 2013). The selectivity of CD47-SIRPα interaction led to the observation that cancer cells express calreticulin (CRT), a pro-phagocytic signal (Gardai et al., 2005), while normal cells do not (Chao et al., 2010b). Thus, it seems that in addition to blocking the "don't eat me" signal by disrupting the CD47-SIRPα interaction, an "eat me" signal is also needed to stimulate macrophages to eat. Others have approached the CD47-SIRPα interaction from the opposite end, by engineering a high-affinity SIRPα variant to out compete native SIRPα for CD47 binding (Weiskopf et al., 2013).

Recent advances in clinical cancer treatment have seen the development of new treatment strategies centered on co-administration of traditional chemotherapeutic drugs with cancer specific-monoclonal antibodies. The efficacy of treatment of hematopoietic malignancies have particularly been improved (Dougan and Dranoff, 2009) including the addition of the anti-CD20 antibody (rituximab) to chemotherapy to improve long-term prognosis of B cell lymphomas (Molina, 2008), NHL (Coiffier et al., 2002; Hallek et al., 2010), and chronic lymphocytic leukemia (CLL) (Wendtner et al., 2004). The improvement in efficacy of treatment is a result of tumor opsonized antibody engagement of the Fc-receptor (FcR) of NK cells (Clynes et al., 2000) or macrophages (Minard-Colin et al., 2008) in a process known as antibody-dependent cell-mediated cytotoxicity (ADCC). A recent study using an inducible mouse model of B cell lymphoma has demonstrated that treatment with the anti-CD52 antibody, alemtuzumab, is efficacious only when administrated as the full length antibody and not as a $F(ab')_2$ fragment which lacks its Fc portion (Pallasch et al., 2014). This study confirms that alemtuzumab, in particular, and immunotherapeutic monoclonal antibodies in general, exert an antitumor activity not by binding to the cancer cell, but by recruiting effector cells that possess the FcR.

These chemo-immunotherapy strategies have also been combined with CD47 therapy to block a negative phagocytic signal while simultaneously delivering a prophagocytic signal. A combination of anti-CD47 antibody plus rituximab has shown synergistic elimination in NHL xenografts in mice (Chao et al., 2010a). The anti-Her2/Neu antibody trastuzumab has been used in combination with a high affinity SIRPα variant to show dramatic shrinking of human breast tumors xenografts in mice (Weiskopf

et al., 2013). Additionally, CD47 blocking plus administration of macrophage stimulating cytokines, M-CSF and GM-CSF, has shown anti-tumor activity in a variety of tumor settings (Hernandez-Ilizaliturri et al., 2005; Sanda et al., 1992; Stockmeyer et al., 1997; Valerius et al., 1993). Finally, co-administration of anti-CD47 strategies with chemo-radiation therapy has shown to increase infiltrating macrophages at tumor sites (Funada et al., 2003; Le et al., 2007; Welsh et al., 2005).

Our recent work using a minimal peptide designed from human CD47 demonstrating the abrogation of phagocytosis has led to the current investigation. Here we solid tumor model displaying a stable, near complete knockdown of CD47. Xenografts of CD47 kd tumors in NSG mice show responsiveness to treatment with polyclonal antibodies while tumors displaying normal CD47 levels do not respond to treatment. We also demonstrate that antibody treatment stimulates macrophage clearance of low CD47 expressing cells, but treatment does not significantly alter CD47 expression of tumor cells. Furthermore, combined treatment with antibody and paclitaxel shows similar tumor shrinking.

4.2 MATERIALS AND METHODS

Materials For washing or antibody staining of cells, PBS without Ca^{2+} or Mg^{2+} (Invitrogen) was supplemented with 2% FBS (Invitrogen). For cell culture, Ham's F-12 growth media, penicillin-streptomycin, and FBS were all purchased from Invitrogen. For flow cytometry, 7-Amino-actinomycin D (7-AAD) was purchased from Sigma and Hoeschst 33342 was purchased from Invitrogen.

Antibodies Primary antibodies used for flow cytometry, and imaging include anti-human CD41-FITC (Biolegend), CD47(B6H12)-APC (Biolegend), CD47(B6H12)-AF647 (BD Pharmingen), CD235a-PE (Biolegend). Primary anti-mouse F4/80-APC/Cy7 (Biolegend), CD11b-PE/Cy7 (Biolegend). Secondary antibodies include donkey anti-rabbit Alexa 488 (Invitrogen), or donkey anti-rabbit Alexa 647 (Invitrogen).

Development of Human CD47-KD Cell Lines A549 cells originally obtained from ATCC were previously made to stably express tdTomato (Harada et al., 2014) and cultured in Ham's F-12 growth media supplemented with 10% FBS and 1% penicillin-streptomycin. Stable CD47-KD cell lines were established using a standard transduction protocol. Briefly, human CD47 short-hairpin RNA (shRNA) lentiviral transduction particles (#NM_00177) were purchased from Sigma. tdTomato-A549 cells were transduced with viral particles and stable clones were generated by puromycin selection. The CD47 knockdown efficiency was determined by antibody staining (B6H12) using flow cytometry. Two stable A549 cell lines were selected based on CD47 knockdown

efficiency. The KD^{+} cell line (#TRCN0000007837) was further refined by successive rounds of flow sorting to establish a 90% CD47 knockdown (CD47 KD^{++}). The WT Scr cell line (#TRCN0000007835) was chosen as it displayed a level of CD47 expression similar to that of untransduced cells and was thus effectively used as a WT Scramble control. WT Scr cells were further transduced with green fluorescent protein (GFP)-lentiviral particles to obtain a genetically engineered cell line stably expressing GFP (wildtype (WT) GFP (Scr)). GFP expressing cells were selected using flow sorting to obtain a highly pure population of GFP^{+} WT Scr cells.

Immunofluorescence A549 cells were seeded on 18 mm^2 circular microscope cover slips in a 6 well plate and allowed to adhere overnight in F-12 growth media supplemented with 10% FBS and 1% antibiotics. Cells were briefly fixed with 4% paraformaldehyde for 5 min at RT followed by three PBS washes. Next, cells were blocked using 3% BSA + 0.05% Tween-20 followed by antibody incubation in blocking buffer. Primary antibodies were used at 1:100 and incubated for 1 hr at RT. After incubation, cells were washed three times with PBS. All donkey secondary antibodies (Alexa Fluor 488 and 647) were stained for 1 hr at RT at 1:400 dilution in PBS. Hoescht 33342 was used to stain DNA at 1 μg/mL for 5 minutes at RT. Cover slips were washed a final three times with PBS before mounting on slides using ProLong Gold Antifade Reagent (Life Technologies), sealed with nail polish, and cured for 24 hours before imaging Images were acquired using an Olympus IX71 inverted microscope with a 300W Xenon lamp illumination using 40x, 60x, or 150x objectives with or without 1.6x

multiplication. Further image analysis was done using ImageJ (National Institutes of Health).

Flow Cytometry of *In Vitro* Cultured Cells A549 cells were dissociated using 10 mM EDTA in PBS, washed, and resuspended in 2% FBS in PBS. Antibody (B6H12-AF647 1:50) incubation was done at RT for 1 hr followed by washing and resuspension in 2% FBS. Samples were run on a BD LSRII.

Establishment of A549 tumors *In Vivo* CD47 knockdown and control cells were dissociated from tissue culture flasks using 10 mM EDTA in PBS. 10^6 cells per injection were suspended in 100 μL ice cold PBS and 25% Matrigel (BD) and injected subcutaneously in the flank of non-obese diabetic/severe combined immunodeficient (NOD/SCID) mice with null expression of interleukin-2 receptor gamma chain (NSG mice). Mice were obtained from the University of Pennsylvania Stem Cell and Xenograft Core. All animal experiments were planned and performed according to IACUC protocols.

In Vivo Tumor Imaging Mice were anesthetized via inhalation of isoflurane at 3 L/min and maintained at 1.5 L/min. Imaging was acquired using a Perkin Elmer IVIS Spectrum with excitation and emission filters set at 535 nm and 580 nm respectively optimized for tdTomato imaging. Images of each face of the sagittal were taken to capture both left and right flanks.

Antibody Treatment Mice were warmed under heat lamp prior to tail vein injection to dilate vein. Rabbit anti-human red blood cell (anti-hRBC) (Rockland Immunochemicals) was reconstituted per manufacturers direction and further diluted using sterile PBS. Mice were injected with 600 μg / animal (~20 mg/kg) twice a week. Anti-human IgG (H+L) (Sigma Aldrich) was injected at 8 μg / animal (~0.3 mg/kg) daily for one week.

Generation of Drug Loaded Polymer Worms Polyethyleneoxide (PEO) - Polybenzylcaprolactone (PBCL) diblock copolymer was obtained from Alberta Research Chemicals Inc. (ARCI), Edmonton, AB, Canada. Aggregates were formed in water by solvent evaporation of the copolymer dissolved in chloroform with the final concentration of polymer in water being 30 mg/ml. The aggregates were mixed with PKH 26 hydrophobic red dye, and morphology confirmed by imaging using an Olympus IX71 microscope with a 60x objective (oil, 1.25 NA) and Cascade CCD camera (Photometrics, Tuscon, AZ). Paclitaxel dissolved in methanol, and was added to the aggregates at a concentration of 30 μg of drug per mg of polymer in dispersion. The mixture was stirred overnight, and the unincorporated drug was removed by dialyzing using a Slide-A-Lyzer Dialysis cassette with a Molecular Weight Cut-Off (MWCO) of 3000 (Thermo Scientific). The dialyzed mixture was centrifuged at 2000 rpm for 8 minutes prior to injection. The drug loading was measured via Shimadzu prominence HPLC (High Performance Liquid Chromatography) with Pinnacle DBC18 Column (4.6x150 mm, 5 μm particles). In vitro cytotoxicity was assayed as described in Cai et al., 2007.

Ex Vivo Tumor Flow Cytometry Analysis On the day of analysis mice belonging to the treatment cohort were injected with the standard antibody dose as described above. Mice were euthanized 1.5-2 hours following injection by cervical dislocation. Tumors and spleens were removed, placed in 20% FBS, and tumor core and periphery tissue was segregated. Tumor tissue was cut into 1-3 mm pieces, transferred to 15 mL centrifuge tubes and spun to remove media. Tissue was then resuspended in 3 mL warm Dispase (STEMCELL Technologies) supplemented with 3 mg/mL Collagenase (Sigma) and 200 uL of 1 mg/mL DNAse I (Roche). Samples were pipetted for 1-3 minutes until cloudy, but not stringy. Dissociation was quenched by addition of 10 mL room temperature PBS and suspension was filtered using a 70 μm cell strainer. Filtrate was spun, supernatant discarded, and pellet resuspended in 2% FBS for antibody incubation. Spleens were prepared by mechanical dissociation, filtration, and RBC lysis using Red Cell Lysing Buffer (Sigma). Lysed samples were washed and resuspended in 2% FBS for antibody incubation.

Prior to antibody incubation samples were blocked with Fc Block (BD Pharmingen) (1:500) for at least 5 min at room temperature (RT). CD47-AF647 (1:25), donkey anti-rabbit AF488 or AF700 (1:400), F4/80 APC-Cy7 (3:50), CD11b PE-Cy7 (1:25), and Hoescht 33342 (1:1250) were incubated at RT for 1 hr. After incubation, cells were washed and resuspended in 2% FBS.

Additionally, RBC samples were prepared each day flow cytometry was done as an internal calibration and normalization standard.

4.3 RESULTS

Antibody Stimulated Tumor Shrinking is Dependent on CD47 Expression

We previously established a human lung cancer cell line expressing the fluorescent protein, tdTomato (Harada et al., 2014). Transduction and antibiotic selection resulted in both a stable "scramble" tdTomato-A549 (WT Scr) cell line and a stable CD47 knockdown tdTomato-A549 (CD47 KD) cell line. Approximately 60% knockdown was confirmed by immunofluorescence (**Fig. 4.S1A, right**). Both WT Scr and CD47 KD were used in a preliminary *in vivo* study in which subcutaneous xenograft tumors were grown on each flank of NSG mice. Tumor progression was monitored in this and all subsequent *in vivo* studies by live animal imaging to detect tdTomato fluorescence. No significant difference in tumor growth rate was observed between WT Scr and CD47 KD (**Fig. 4.S1B**). Motivated by recent work showing tumor shrinking by blocking the CD47-SIRPα interaction by injection of a high affinity SIRPα variant in combination with a chemotherapeutic antibody (Weiskopf 2014) and the well established use of Rho(D) antibodies in suppression of isoimmunization, we hypothesized that any opsonizing antibody could be used in combination with CD47-SIRPα disruption. Indeed, when mice bearing CD47 KD xenograft tumors are treated with anti-human IgG antibody, tumors shrink to ~60% of the size at treatment initiation by 7 days (**Fig. 4.S1C**). We further enriched our CD47 KD cell line by 2 rounds of cell sorting to purify for CD47 knockdown cells (CD47 KD^{+}) and confirmed by flow cytometry (**Fig. 4.S2C**). Subcutaneous xenograft tumors grown on the flank of NSG mice show no significant difference in growth rate between WT Scr and CD47 KD^{+} (**Fig. 4.1A**). To show that antibody-mediated tumor shrinking of CD47 knockdown tumors is truly independent of

one particular antibody, we treated mice with an anti-human RBC antibody (Ab) that is the purified IgG fraction from antiserum. Ab binding to A549's was confirmed by immunofluorescence (**Fig. 4.1C**). Nearly 50% reduction in tumor size was observed after 4 weeks of biweekly treatment (**Fig. 4.1B**). The highest dosage of Ab is equivalent to ~20% of serum IgG levels in fully immunocopetent C57BL/6 mice (Klein-Schneegans et al., 1989) and ~150% of serum IgG levels reported for humanized NSG mice (Rajesh et al., 2010) (**Table 4.1**). When antibody treatment is discontinued, tumors continue growing at a similar rate as observed prior to treatment and independent of CD47 expression (**Fig. 4.1A, B**). Surprisingly, after this period of uninterrupted regrowth, reapplication of antibody is again capable of shrinking CD47 KD^{+} tumors (**Fig. 4.1B**) with similar apparent kinetics as the first round of treatment.

Although the CD47 KD^{+} had been cell sorted it still contained a small subpopulation of cells expressing normal levels of CD47. To determine that it is truly the low CD47 cells that are being cleared, we furthered enriched the CD47 KD^{+} cell line by additional cell sorting (CD47 KD^{++}) and also transfected the WT Scr cell line with GFP (GFP WT Scr). Flow cytometry confirmed GFP expression and CD47 KD^{++} knockdown of 93% (**Fig. 4.S5B**). Despite multiple rounds of cell sorting, the CD47 KD^{++} cell line still contained a minor population expressing normal CD47 levels, but this was determined to be minor (~10%) and distinct (by flow cytometry) from the CD47-low "true CD47 knockdown" majority. NSG mice were split into the following 3 cohorts: 1) WT GFP Scr, 2) CD47 KD^{++}, 3) Mosaic (WT GFP Scr/CD47 KD^{++} injected 1:3). The mosaic tumors were subsequently determined to be comprised of a 1:2.7 ratio of WT GFP Scr : CD47 KD^{++} by flow cytometry (**Fig. 4.1E** and **4.S5B**). Xenografts were again

grown subcutaneously on each flank. CD47 KD^{++} tumors showed an enhanced growth rate compared to tumors containing WT CD47 expression levels (**Fig. 4.1D**) perhaps consistent with previous observation of the loss of thrombospondin-1 signaling through CD47 increasing stemness (Kaur et al., 2013). Mosaic tumors treated with Ab showed a slightly enhanced responsiveness as CD47 KD^{+} reached a 40% reduction in tumor size by 10 days following biweekly dosing (**Fig. 4.1E**). Tumors excised from euthanized mice at the termination of treatment show an inversion of GFP^{+} : GFP^{-} ratio (**Fig. 4.1F**). The initial ratio of 1:2.7 was not significantly changed in untreated mosaic tumors while the antibody treated mosaic tumor ratio was 3.3:1 indicating that tumor shrinking was due to selective clearance of GFP^{-} CD47 KD^{++} cells.

Antibody Treatment Is Not Accompanied by Adverse Hematologic Side Effects

Several previous studies disrupting the CD47- SIRPα interaction in mice by treatment with anti-CD47 antibody (see Willingham 2012) or a high affinity SIRPα variant-human IgG fusion (Weiskopf 2013) showed significant loss of RBCs and development of chronic anemia. Animals treated with Ab do not show a loss of weight, as is common with chemotherapeutic strategies, and in fact most treated animals gained weight throughout the study (**Fig. 4.2A, 4.S2F**). Contrary to these other similar approaches, our treatment strategy does not significantly affect PB cells. Platelet counts remain relatively unchanged, however, there is a slight insignificant reduction in hematocrit following antibody treatment (**Fig. 4.2B**). These trends in cell number reduction are mirrored by the tendency of antibody opsonization of RBCs and platelets (**Fig. 4.2C**). *In vitro* binding of Ab to mouse RBCs (mRBC), human RBCs (hRBCs), or MEG-01 (a human

megakaryocytic cell line) showed that the affinity of antibody for mRBC is ~300 μM (**Fig. 4.S2A,B**), which is ~10^{-4} weaker than for human cells. Despite this dramatically reduced affinity, local concentrations of Ab at the injection site could briefly approximate the affinity for mRBC, thereby opsonizing a fraction of mRBC that could explain the slight reduction in observed hematocrit.

Antibody Treatment as Efficacious as Chemotherapy in CD47 Knockdown Tumors

Recent clinical advances using a combination therapy comprised of a highly specific monoclonal antibody, such as rituximab, with chemotherapy (see for example Coiiffier 2002 or Hallek 2010) motivated the addition of the front-line chemotherapeutic paclitaxel with Ab treatment. Our group has shown that paclitaxel (Tax) loaded polymer filomicelles are capable of shrinking A549 and U251 xenograft tumors in the flank of mice (Baumann et al., 2013; Christian et al., 2009). Leveraging our polymer expertise, we generated Tax loaded filomicelles capable of killing A549 cell *in vitro* regardless of CD47 expression (**Fig. 4.3B**) as also evident by similar Hill Coefficients for each cell type (**Fig. 4.S3A**). Cytotoxicity was quantified using the MTT assay described in Cai *et al* (Cai et al., 2007). As expected, CD47 KD^{++} tumors responded to either Ab alone or Ab + Tax while normal CD47 tumors responded to combination treatment only (**Fig. 4.3A, 4.S3D**). Tumor shrinking by Tax displayed similar rate and magnitude of shrinking as we previously reported (Christian et al., 2009). While the addition of chemotherapy to antibody treatment was not synergistic, there was a slight additive effect, but this additional response was not significantly different than Ab treatment alone. HPLC quantification of Tax concentration in filomicelles revealed that the average Tax dose

delivered was ~4.4 mg/kg (**Fig. 4.S3B**). Addition of Tax to the antibody treatment resulted in further reduction in hematocrit and a slight elevation in thrombocrit (**Fig. 4.3C**) without significantly altering antibody binding (**Fig. 4.3D**). None of the mice from any treatment arm experience weight loss during the treatment period (**Fig. 4.S3C**), but a slight reduction in $CD11b^+$ leukocytes was observed upon application of Tax (**Fig. 4.3E**). These results indicate that similar tumor shrinking can be achieved by CD47-SIRPα disruption and antibody rather than a chemotherapeutic approach.

Antibody Treatment Shrinks Tumors by Macrophage Phagocytosis of CD47 Knockdown Cells

At the completion of each treatment regimen, mice were euthanized, xenograft tumors removed, and when possible, core and periphery tumor tissue kept separated, and analyzed by flow cytometry (**Fig. 4.4A**). Flow cytometry of tumor tissue showed similar CD47 expression levels regardless of antibody treatment (**Fig. 4.4B**). GFP expression in the mosaic tumors helped in determining a more granular view of CD47 expression and this strategy again revealed similar CD47 levels between untreated and Ab treated within a specific population. A closer examination of the CD47 surface density on the A549 tumor cells, reveals that each knockdown cell type displayed <200 molecules/μm^2 at the time of tumor inoculation (**Table 4.2**). Even these values are likely conservative overestimates resulting from an underestimate of A549 surface area determined by imaging well spread cells. Periphery and core tumor tissue were similarly opsonized and this level of opsonization was matched in mouse stromal cells (**Fig. 4.4D**). Likewise, mature macrophages in tumor core and periphery showed bound Ab, however the level of

Ab binding to macrophage was much higher than in either tumor or stromal tissue, and macrophages of the periphery had slightly more bound Ab than those of the core. Tissue from mice used in the mosaic tumor studies recapitulated the trends in Ab binding showing similar levels in tumor xenograft and mouse stroma accompanied by a higher level in tumor and splenic macrophages. Additionally, Ab likewise bound macrophages in the PB. These data provide evidence of a direct interaction of the antibody with macrophages and that macrophages in the circulation retain and/or bind antibody. Analysis of total macrophage numbers as a percent of total mouse cells within a given tissue reveal significantly higher numbers of mature macrophages and that neither subpopulation significantly changes by antibody treatment (**Fig. 4.4F, left**). Addition of Tax to antibody treatment showed similar macrophage numbers in CD47 KD^{++} and spleen (**Fig. 4.4F, right**) compared to CD47 KD^{+} and mosaic studies. However, the number of mature macrophages found in WT Scr tumors is elevated with Tax perhaps a response to chemotherapeutic induced tumor apoptosis.

We next wanted to see whether Ab binding to macrophage was providing a phagocytic stimulus. To do this, macrophages were analyzed by flow cytometry using a modified gating scheme (**Fig. 4.S4A**) that has been previously published (Rose et al., 2012). This method allows discrimination between immature ($CD11b^{+}$F4/80intermediate) and mature ($CD11b^{+}$F4/80hi) macrophages. In general, the immature macrophage subpopulation had much less Ab bound and was very infrequently $tdTomato^{+}$ (**Fig. 4.S4D, E, 4.S5D, E**). Mature macrophages from untreated mice were infrequently $tdTomato^{+}$, but mature macrophages from treated animals showed a drastic increase in tdTomato, treatment antibody, or both (**Fig. 4.5A**). Macrophages that were $tdTomato^{-}$

from the CD47 KD^{+} study were equally Ab bound regardless of tissue source (**Fig. 4.5B, right**), however, tdTomato^{+} macrophages showed a marked increase when bound to antibody and such macrophages were more frequent from CD47 KD^{+} tumors (**Fig. 4.5B, left**; compare bars 2 & 4 with 8 & 10). Similar trends were seen from mosaic tumors. Specifically, treatment with antibody resulted in an increase in tdTomato^{+} in antibody bound macrophages (**Fig. 4.5C**). Addition of Tax to the antibody showed similar Ab binding to macrophage in the tdTomato^{-} fraction (**Fig. 4.5D, right**; compare with Fig. 5B, right filled bars) and antibody treatment alone recapitulated the tdTomato^{+} Ab bound percentages seen in the CD47 KD^{+} study (compare Fig. 5D left, bars with black outline vs. Fig. 5B left, solid bars). Interestingly, supplementing antibody treatment with Tax resulted in an increase in tdTomato^{+} Ab bound macrophages compared to antibody alone for WT Scr and CD47 KD^{++} tumors (**Fig. 4.5D, left**; compare black outlined bars with bars without outline). The likely cause of such an increase may be due in part to an increase in CRT expression on chemotherapy induced apoptotic cells, which would provide an additional "eat me" signal. Such an increase has been reported in leukemic cells as soon as 72 hours following cyclophosphamide treatment (Pallasch et al., 2014) and shown to be sufficient to induce phagocytosis (Gardai et al., 2005). These results provide a mechanism of antibody mediated tumor clearance whereby disruption of the CD47-SIRPα, in this case by CD47 knockdown, provides a removal of the normally present "don't eat me" signal, while antibody opsonization provides a phagocytic stimulation to mature macrophages effectively delivering an "eat me" signal.

Figure 4.1 *In Vivo* tumor growth and Ab treatment

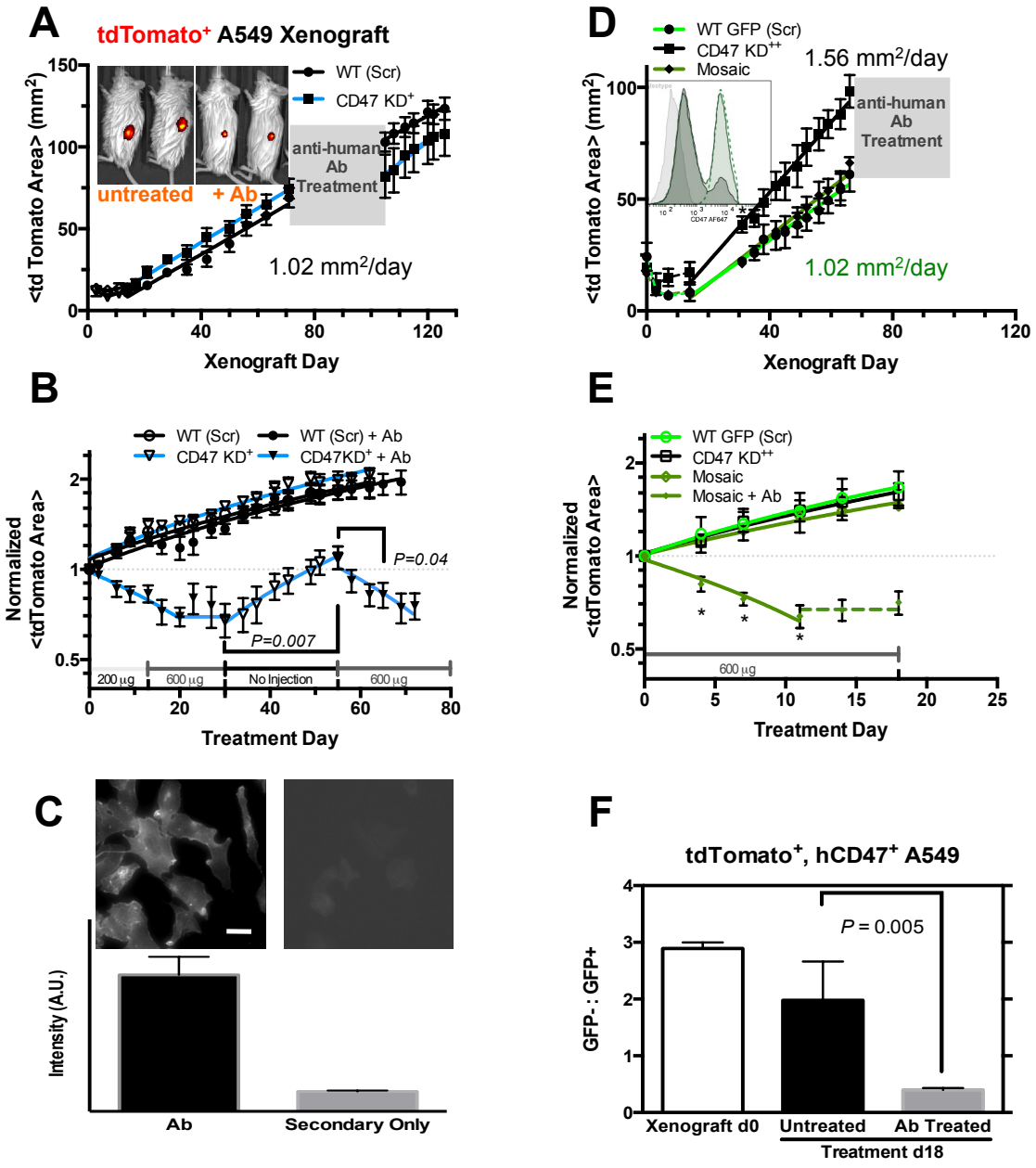

Figure 4.1 *In Vivo* tumor growth and Ab treatment

(**A**) *In vivo* growth curve of CD47 KD^{+} "deep knockdown" during 2 periods of no treatment. (WT Scr: n=4 mice, 8 tumors; CD47 KD^{+}: n=6 mice, 12 tumors. Mean ± SEM). Slope of linear fit = 1.02 mm^2/d corresponding to tumor growth rate (R^2=0.99). (**A, inset**) Representative fluorescent overlays of untreated (left) and Ab-treated (right) mice at the end of the treatment period. (**B**) Tumor response to 200 and 600 μg Ab / mouse followed by removal of antibody and subsequent re-administration. (WT Scr ± Ab, CD47 KD^{+} - antibody: n=2 mice, 4 tumors; CD47 KD^{+} + antibody: n=4 mice, 8 tumors. Mean ± SEM). (**C**) Immunofluorescence confirms Ab binding (left) to A549 *in vitro* compared to secondary antibody only control (right) (scale bar = 10 μm). Images have been adjusted to allow visualization of cells in control image. Bar graph below the images reflects true fluorescence of each unaltered image. (**D**) CD47 KD^{+} cells were further sorted to generate CD47 KD^{++}, an ultra-deep knockdown. Xenotransplants in NSG mouse flanks show a slight growth advantage for CD47 KD^{++} (linear fit slope = 1.56 mm^2/d, R^2=0.99) compared to tumors comprised of WT GFP Scr either in part or in whole (linear fit slope = 1.02 mm^2/d, R^2=0.98). (WT GFP Scr: n=2 mice, 4 tumors; CD47 KD^{++}: n=2 mice, 4 tumors; Mosaic: n=6 mice, 12 tumors. ± SEM). (**D, inset**) Flow cytometry of cells used in xenotransplants. (gray=isotype; black=CD47 KD^{++}; green dashed outline=WT GFP Scr; green fill=Mosaic) (**E**) Treatment of tumors shown in (A) with 600 μg Ab / mouse twice a week. Solid lines are corresponding linear fits with R^2>0.97. Dashed line is fit of average of final three points each of which are insignificant from d 15. (* P<0.05, compared to previous data point, within a treatment arm. (WT GFP Scr, KD^{++}, and Mosaic - antibody: n=2 mice, 4 tumors; CD47 KD^{+}: n=2 mice, 4 tumors; Mosaic + antibody: n=4 mice, 8 tumors. Mean ± SEM). (**F**) Ratio of GFP^{-}:GFP^{+} as determined by flow cytometry following removal of tumors from sacrificed mice. (Xenograft d0: n=9, 3 independent experiments done in triplicate; Untreated: n=4 tumors; Ab Treated: n=8 tumors. Mean ± SEM). Xenograft d0 was measured using cells reserved during xenotransplantation and subsequently measured by flow cytometry.

Table 4.1. Relative IgG Supplementation

	Total IgG	For 30 g mouse		Inject 0.6 mg IgG Ab
	mg/mL	Blood (mL)[1]	mg IgG	% of IgG
C57BL/6[2]	1.5	2.4	3.6	17%
Humanized NSG[3]	0.165	2.4	0.4	154%
				300 ug Rhogam
	mg/mL	L	mg IgG	% of IgG
Hu IgG	10	5	50000	0.0006%

Table 4.1. Relative IgG Supplementation

Calculated estimate of the IgG percent in immunocompetent mouse strains. Calculation assumes a 30 g mouse and 0.6 mg Ab injection. % of IgG is calculated as 0.6 mg injected Ab / total mg IgG * 100%. This value provides a magnitude of the Ab dosage for comparison with what is present in immuncompetent animals. Also as a comparison, a typical 300μg dose of Rhogam represents 0.0006% of total human IgG. Literature values: mouse blood volume[1] from (Mitruka and Rowan, 1981), C57BL/6 IgG concentration[2] from (Klein-Schneegans et al., 1989) , humanized NSG IgG concentration[3] from (Rajesh et al., 2010).

Figure 4.2 Ab treatment does not cause significant adverse side effects

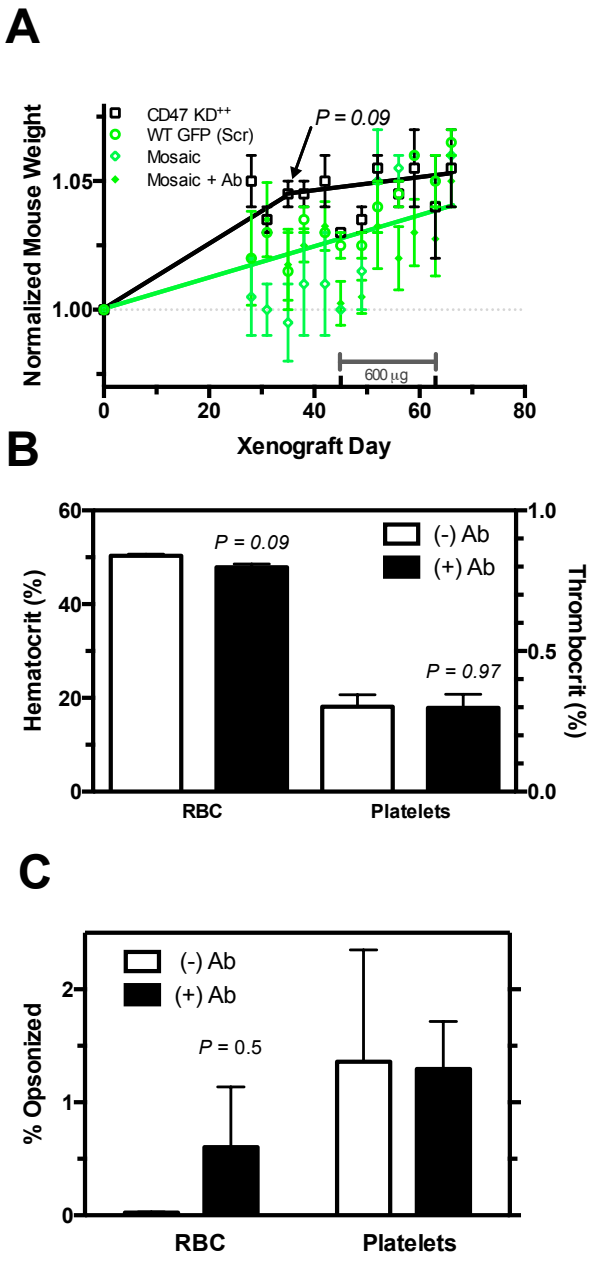

Figure 4.2 Ab treatment does not cause significant adverse side effects

(**A**) Weight throughout duration of study (including pre-treatment, treatment, and post-treatment). Weight is normalized to weight at date of xenograft implantation. Mice used in Mosaic Study. (WT GFP Scr: n=2 mice; CD47 KD^{++}: n=2 mice; Mosaic: n=2 mice; Mosaic+Ab: n=4 mice). WT GFP Scr, Mosaic, Mosaic+Ab are grouped together and the green solid line reflects the linear fit. CD47 KD^{++} mice show slightly different weight responses as shown by the black solid line. (**B**) Addition of antibody shows a slight decrease in hematocrit, but no change in thrombocrit. ($n \geq 2$ per group. Mean ± SEM). (**C**) Minimal opsonization of annucleated PB cells. ($n \geq 2$ per group. Mean ± SEM).

Figure 4.3 Combined ab + chemotherapy treatment of CD47 knockdown tumors

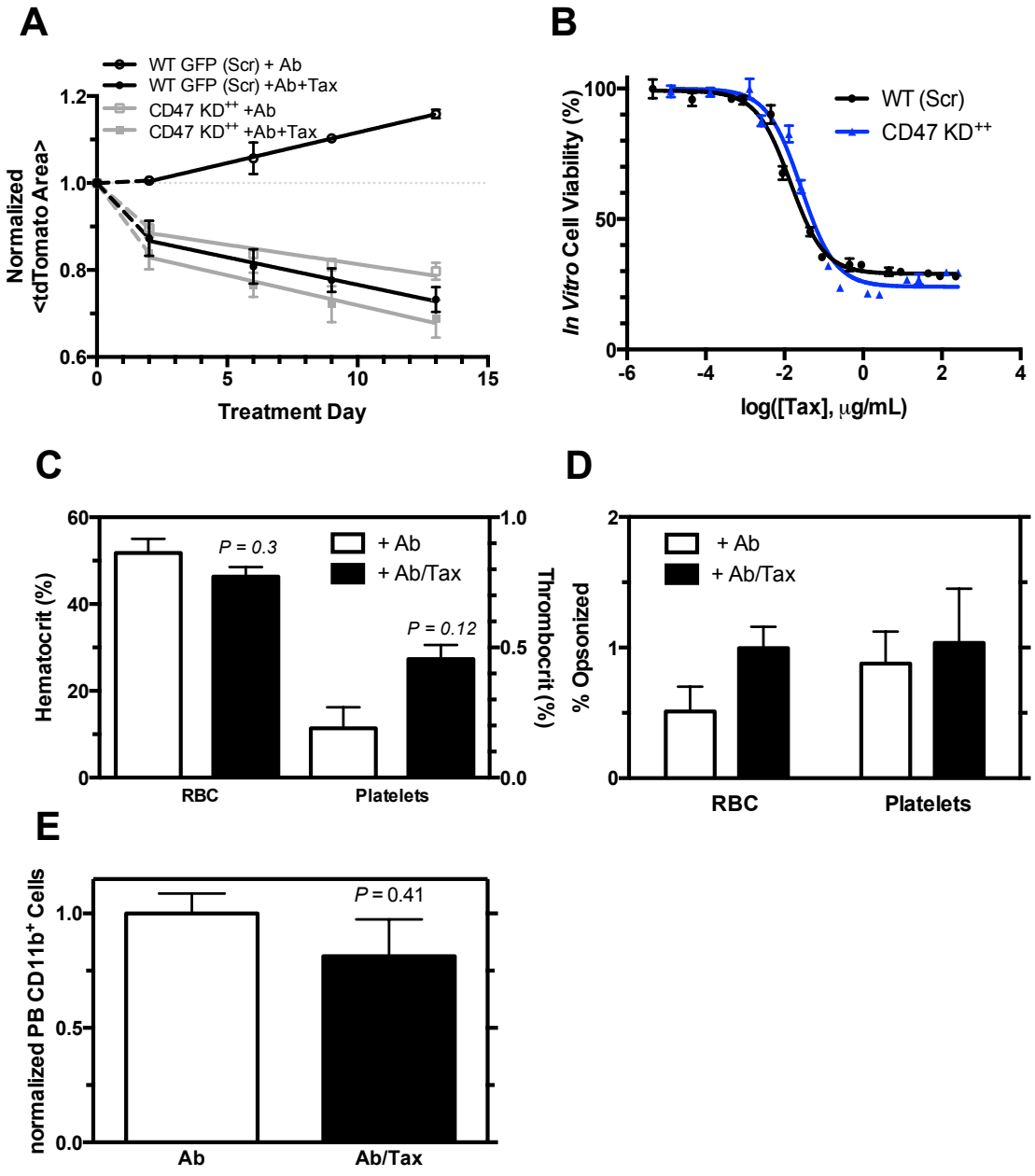

Figure 4.3 Combined Ab + chemotherapy treatment of CD47 knockdown tumors

(**A**) Treatment with Ab is efficacious only for CD47 knockdown tumors (similar to Fig. 1), but paclitaxel loaded polymer worms (TW) shrink tumors regardless of CD47 expression level. Combining Ab, chemotherapy, and CD47 knockdown shows a slight enhancement in tumor responsiveness. Mice were treated 2 times per week (n=2 tumors per treatment arm. Mean ± SEM). (**A**) Quantification of *in vitro* cytotoxicity of paclitaxel loaded polymer worms against wild-type (WT) and knockdown (KD) A549 cells. Data fit with the following equation: $CV\% = A + B/(1+10((\log(conc)-\log(IC_{50}))))$. Fits summarized in Fig. S3A. (n=4 independent experiments, Mean ± SEM). (**C**) Addition of taxol to the treatment shows a slight decrease in hematocrit and a more significant increase in thrombocrit (n=2 per group. mean ± SEM). (**D**) Taxol does not significantly effect opsonization of anucleated PB cells (n=2 per group. Mean ± SEM). (**E**) Addition of Taxol to Ab treatment results in a slight reduction in $CD11b^{+}$ leukocytes (n=2 per group. Mean ± SEM).

Figure 4.4 *Ex vivo* analysis of mouse tissue following treatment

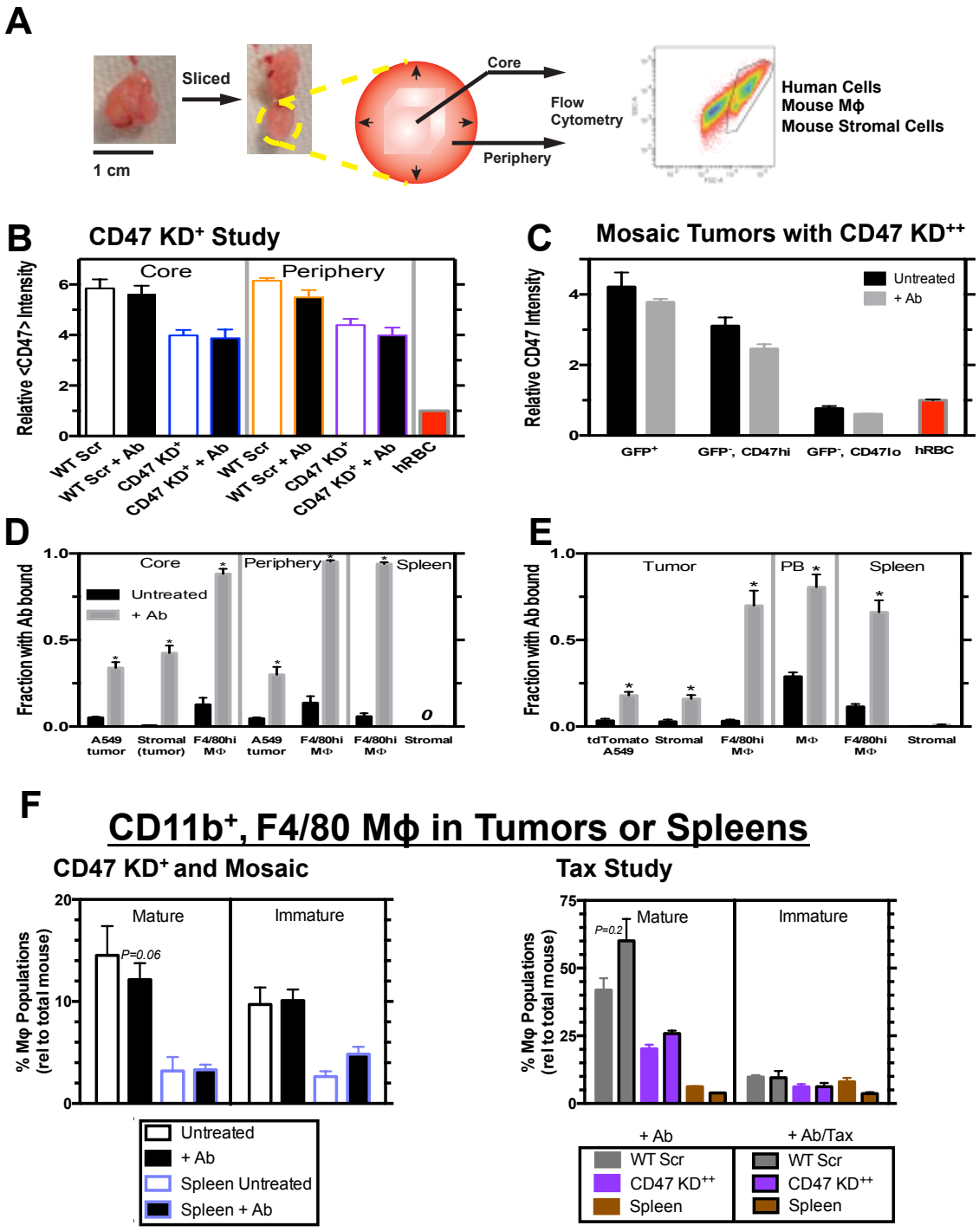

Figure 4.4 *Ex vivo* analysis of mouse tissue following treatment

(**A**) Schematic of method used to assess tumor tissue. Tumors are removed and when possible the periphery and core are prepared separately. Following dissociation and antibody incubation, samples are analyzed using flow cytometry. (**B**) Relative CD47 expression (normalized by human RBC, average of at least triplicate) of various tumor types and specific location for CD47 KD^+ study. ($n \geq 8$ tumors per group. Mean ± SEM). (**C**) Relative CD47 expression, as in B, for specific populations as resolved by WT GFP Scr GFP expression ($n \geq 4$ per group. Mean ± SEM). (**D**) Ab binding to various tissue types for CD47 KD^+ study. Value represents the fraction of a given tissue type that is Ab^+ per tissue. ($n \geq 10$ tumors/spleens per group. Mean ± SEM). (**E**) Ab binding to various tissue types for Mosaic Tumor study. Value represents the fraction of a given tissue type that is Ab^+ per tissue. ($n \geq 4$ tumors, $n \geq 2$ spleens per group. Mean ± SEM). (**F**) Quantification of both mature and immature macrophages as represented as the % of total non-human cells for the CD47 KD^+ and Mosaic Study (left), and Taxol study (right) (*P<0.05).

Table 4.2 CD47 Cell surface density

			In Vitro		*In Vivo*		
		Area (μm²)	CD47 (norm)	CD47/μm²	CD47 (norm)	CD47/μm²	
	WT Scr	382	5.00±0.04	463	5.5±0.2	509	
	CD47 KD⁺		2.12±0.05	196	4.1±0.1	379	←
	CD47 KD⁺⁺		1.26±0.04	117	2.37±0.07	219	←
Mosaic	GFP⁺, CD47hi		6.20±0.02	574	3.9±0.2	361	
Mosaic	GFP⁻, CD47hi		4.73±0.03	438	2.7±0.2	250	
Mosaic	GFP⁻, CD47lo		0.41±0.05	38	0.66±0.03	61	←
	hRBC	141±3.0	1.00	250			
		Engstrom 1998		Tsai 2008			

Table 4.2 CD47 cell surface density

In vitro (cells used for xenotransplant) and *in vivo* (cells recovered from excised tumors) CD47 surface density determined by flow cytometry and immunofluorescence. A549 cell area was determined by measuring area of well spread cells imaged by immunofluorescence. This value was multiplied by two assuming negligible height for well spread cells. We acknowledge that this method underestimates cell area and calculated values for CD47/μm^2 are thus likely overestimates. CD47 intensity was determined by flow cytometry mean fluorescence intensity and normalized to human RBCs. Arrows indicate IgG treatment responsive cells. We previously reported a CD47 surface density value for hRBCs (Tsai and Discher, 2008). Multiplying this value by the normalized CD47 intensity and scaling by the ratio of A549 area to hRBC area previously reported (Engström and Löfvenberg, 1998), results in the values presented in the table.

Figure 4.5 Assessment of phagocytic activity of mature macrophage subpopulation

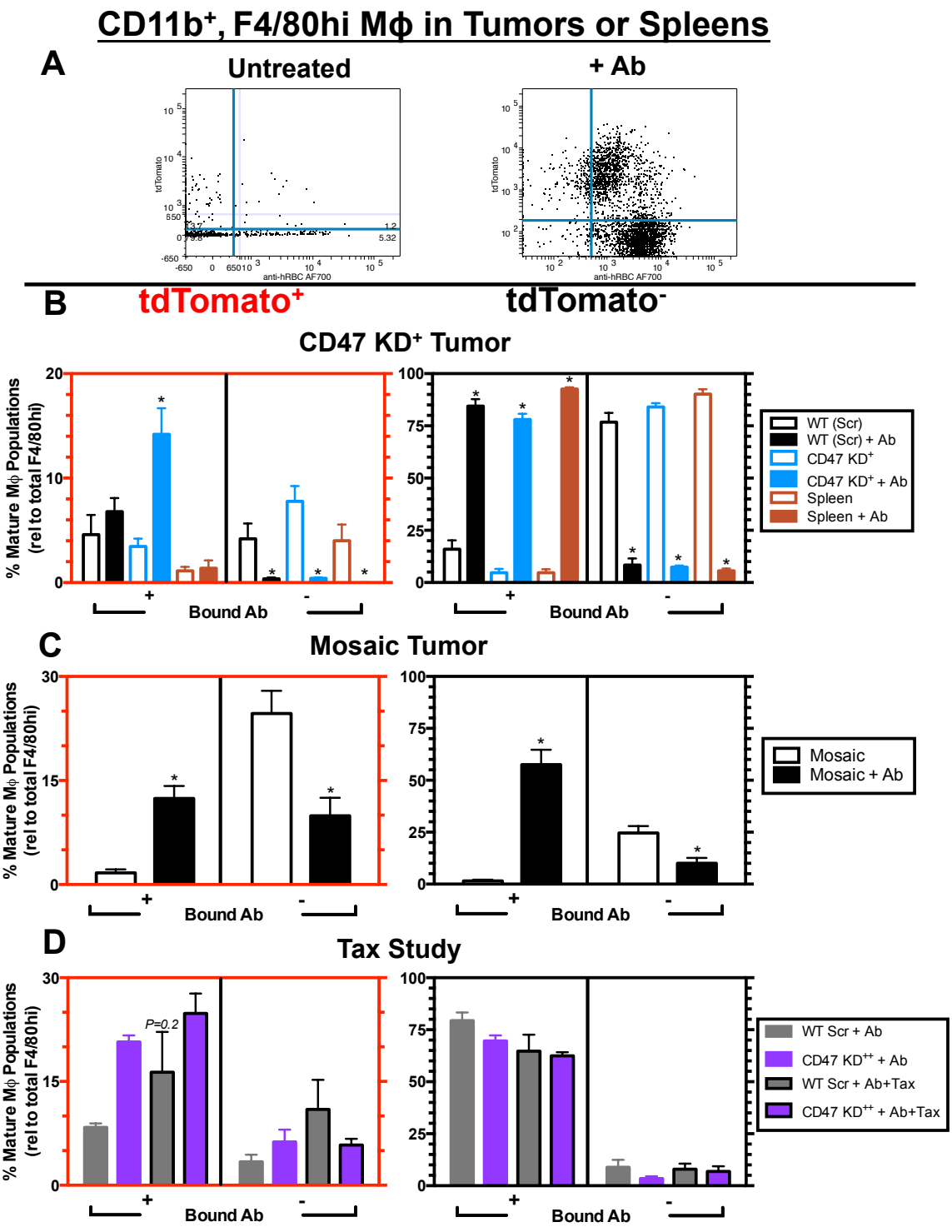

Figure 4.5 Assessment of phagocytic activity of mature macrophage subpopulation

(**A**) Representative flow cytometetry scatter plots of $CD11b^{+}F4/80hi$ populations depicting Ab binding (x-axis) and phagocytosis (y-axis, $tdTomato^{+}$) for untreated (left) and Ab treated (right) tumor samples. (**B**) Breakdown of mature macrophage populations as the % of total mature macrophages either $tdTomato^{+}$ (left) or $tdTomato^{-}$ (right) for CD47 KD^{+} study animals ($n \geq 5$ tumors/spleens per group. Mean ± SEM). (**C**) Breakdown of mature macrophage populations as the % of total mature macrophages either $tdTomato^{+}$ (left) or $tdTomato^{-}$ (right) for Mosaic Tumor study animals ($n \geq 4$ tumors/spleens per group. Mean ± SEM). (**D**) Breakdown of mature macrophage populations as the % of total mature macrophages either $tdTomato^{+}$ (left) or $tdTomato^{-}$ (right) for Taxol study animals ($n \geq 4$ tumors/spleens per group. Mean ± SEM).

4.4 DISCUSSION

In this study, we provide a mechanistic view of ADCC amplified by the loss of CD47 expression without adverse effects to anucleated PB cells. Compared with CD47 knockdown tumors, growth of tumors displaying normal levels of CD47 was unaffected by antibody treatment. Additionally, treated tumors resume growing at rates similar to those before treatment and are responsive to reapplication of antibody after allowed to regrow to sizes similar to those at the onset of the initial treatment period (**Fig. 4.1A**). Response to the second round of treatment shows similar efficacy as the initial treatment period indicating the presence of an antibody responsive low CD47 expressing component. Treatment with IgG does not directly impact CD47 expression of tumor cells as seen by comparing tissue samples *ex vivo* (**Fig. 4.4B, C**). Flow cytometry of A549 cells prior at the time of xenotransplant shows conservative estimates of CD47 surface density of knockdown cell types to be much lower (**Table 4.2**) than what we have previously reported for normal human RBCs (Tsai and Discher, 2008). Tsai and Discher also reported an inhibition constant of ~20 molecules/μm^2 for human THP-1 cells phagocytosing human CD47 coated beads (Tsai and Discher, 2008). Considering that the values determined in Table 4.1 are likely overestimates and that the affinity of mouse SIRPα for human CD47 is likely less than that of human SIRPα for human CD47, the CD47 surface density of our knockdown cell agree remarkably well with the K_i determined by Tsai and Discher.

Use of a mosaic tumor composed of GFP^+ cells that have normal CD47 levels and CD47 knockdown GFP^- cells support the view that antibody treatment is dependent on the disruption of the CD47-SIRPα interaction. Particularly, the GFP^+ : GFP^- ratio is

unchanged in the absence of Ab, but the ratio is inverted after Ab treatment (1:2.7 vs 3.3:1, **Fig. 4.1F**). Surprisingly, we find that CD47 KD^{++} cells grow more rapidly than WT Scr cells (**Fig. 4.1C**) *in vivo*. The expression of the prophagocytic surface protein CRT has been shown to be highly correlated with CD47 expression for a number of cancers (Chao et al., 2010b) and provides a means of selective clearance when treated with anti-CD47 antibody. It would thus seem that CD47 knockdown would tip the balance toward calreticulin, resulting in an increase in phagocytosis and limit or prevent tumor progression. The accelerated growth rate of CD 47 KD^{++} tumors in the present work could be a result of concomitant reduction in calreticulin following CD47 knockdown to maintain the WT calreticulin:CD47 ratio as has been seen in colorectal cancer (Steinert et al., 2014). Alternatively, high levels of calreticulin have been found to be a poor clinical prognostic in numerous malignancies (Chao et al., 2010b). Transfection of vasostatin, the N-terminal domain of calreticulin, results in downregulation of tumor suppressor genes including p53, nm23, Rb, and vinculin as well as enhancement of cell spreading, adhesion, and invasion (Liu et al., 2005). Each of these factors could be a driver in accelerating tumor growth. It is known that A549 cells have the capacity for some plasticity as they express key stem cell transcription factors (Teng et al., 2010), which we have confirmed (**Fig. 4.S1D**). CD47 loss from endothelial cells promotes stemness and proliferation with a role for altered adhesion (Kaur et al., 2013). Since the mosaic tumors show similar growth kinetics as WT Scr tumors, the mosaic tumors could, in principle, be dominated by the adhesive signaling of WT Scr cells which acts to repress stem-like proliferation. Combination of the chemotherapeutic drug paclitaxel with Ab treatment, while slightly additive, did not significantly improve CD47 knockdown tumor shrinking.

Interestingly, taxol treated tumors showed an increase in total mature macrophages at the expense of immature macrophages in the spleen (**Fig. 4.4F**) as well as an increase in phagocyotsing opsonized mature macrophages in the tumor (**Fig. 4.5D**). These results may be an effect of macrophage mobilization in response to a taxol induced inflammatory signal (Funada et al., 2003; Le et al., 2007; Welsh et al., 2005), or may be evidence of a larger effect of taxol on upstream hematopoiesis (**Fig. 4.3C**), as we also observe a slight increase in thrombocrit, decrease in hematocrit, and decrease in PB $CD11b^{+}$ leukocytes (**Fig. 4.3E**) when mice are treated with taxol. Others have reported similar effects of taxol on hematopoiesis in which BFU-E and CFU-GM are drastically reduced by taxol *in vitro*, while CFU-Meg is only minimally effected (Pertusini et al., 2001). Since taxol induces apoptosis by inhibition of microtubule depolymerization, it would be sensible that megakaryocytes, which normally divide without cytokinesis, would be less sensitive than other lineages.

Others have demonstrated macrophages to be the main effector responsible for tumor shrinking during CD47 targeted antibody treatment. Depletion of NK cells or complement was not shown to have an affect on tumor clearance, but depletion of macrophages did abrogate efficacy (Chao et al., 2010a). Further, with use of Fc truncated ($F(ab')_2$) anti-CD47 antibody or cancer targeted monoclonal $F(ab')_2$ it was shown that treatment with anti-CD47 antibody is FcR-independent, while synergistic phagocytosis is only observed with full length monoclonal antibody (Chao et al., 2010a; Pallasch et al., 2014). These observations indicate opsonization of the tumor cell to be sufficient to overcome the CD47-SIRPα interaction in the case of the former, whereas the monoclonal antibody acts not through directly binding to the cancer cell, but through engagement of

the FcR on the macrophage. We also found that the antibody used to stimulate macrophage phagocytosis only needs to be capable of binding tumor cells. Both anti-human IgG antibody and anti-hRBC antibody showed similar tumor shrinking capacity when treating CD47 knockdown tumors (**Fig. 4.1B, 4.1E, 4.S1C**). Clinical antibodies used to treat malignancies are, mostly, highly specific to an epitope upregulated in a specific cancer, but also present on normal cells resulting in opsonization of tumor and normal tissue and thus destruction of both. The ability to use any polyclonal antibody, as in the current work, could provide a cost effective means of treatment if combined with selective CD47 expression modulation.

Analysis of macrophages harvested from tumors and spleen provides insight into the mechanism of CD47 dependent ADCC. These data show mature macrophages to be much more highly bound by Ab than their immature brethren. These opsonized mature macrophages also show an increase in phagocytosis, as indicated by tdTomato^{+} by flow cytometry (**Fig. 4.5B-D**). Ab opsonizes human tumor and mouse stroma to a similar level (**Fig. 4.4D** & **4.4E**), however no significant anemia, thrombocytopenia, or weight loss is observed (**Fig. 4.2**). With the observation that CD47-low expressing cells are selectively eliminated upon antibody treatment, the selective phagocytosis seems to come from a combination of suppression of a "don't eat me" signal (CD47-SIRPα disruption) and the addition of an "eat me" signal (FcR engagement by opsonizing antibody).

One of the limitations of many chemotherapeutic drugs is that they are large molecules dependent on the vasculature for delivery to the tumor. This limitation is particularly problematic in treating metastases of the brain, as the blood-brain barrier is notoriously difficult to traverse. Our laboratory has previously demonstrated this using

Tax-loaded polymer filomicelles. Subcutaneous flank tumors were responsive to treatment, but cranial xenograft tumors of the same cell type were not responsive (Baumann et al., 2013). Cell based means of tumor shrinking can avoid vascular dependence since, for example, macrophages are highly motile and capable of invading tissue. Despite the tumor core being undervascularized, and commonly necrotic, we see similar macrophage and tumor opsonization in core versus periphery, indicating that the antibody freely permeates the tumor, as well as similar numbers of phagocytic macrophages regardless of tumor site, supporting the view of macrophage invasiveness. Tumor-associated macrophages (TAMs) are known to polarize to either anti-tumor M1 type or pro-angiogenic, and thus pro-tumor, M2 type (Condeelis and Pollard, 2006; Mantovani et al., 2002; Murdoch et al., 2008). Perhaps CD47 targeted antibody treatment may provide an environment that favors M1 programs.

Crude polyclonal antibodies have been used for decades, most commonly in the suppression of Rh isoimmunization (e.g. (Moise and Argoti, 2012; Tiblad et al., 2013)). Products such as RhoGam, introduced in 1968, are initially given to Rh^- women who are pregnant with their first Rh^+ fetus immediately following a sensitizing event typically birth, but also including abortion, miscarriage, and ectopic pregnancy. Fetal RBCs cannot cross the placenta during development, but during the sensitizing event, Rh^+ RBCs from the fetus enter the mother's blood stream. Left unchecked the mother's immune system will begin to make antibodies against the Rh^+ RBCs. These antibodies are capable of crossing the placenta and could cause complication for each subsequent pregnancy of a Rh^+ fetus ranging from jaundice and anemia to mental retardation and heart failure. RhoGam and similar Rh antibodies bind to fetal Rh^+ RBCs and destroy them before the

mother's immune system can start producing her own antibodies despite the dosage of IgG representing <1% of total IgG (**Table 4.1**). Recently, other products, such as WinRho (anti-D IgG), have found additional applications including the treatment of immune thrombocytopenic purpura (ITP) in Rh^+ individuals. Anti-D IgG treatment causes a slight decrease in hematocrit and hemoglobin, but treatment is as effective as intravenous immunoglobulin thus proving to be a lower cost alternative (Celik et al., 2013; O'Brien et al., 2007). The hemolytic side effects of anti-D IgG are similar to what is observed with administration of our antibody (**Fig. 4.2B**).

Recent efforts have readdressed decades old methods of treating cancer with tumor-derived vaccines. Anti-cancer vaccines in clinical trials (e.g. NCT01995227 and NCT00459069 per ClinicalTrials.gov) take advantage of a diversity of complex antigens as indicated by proteomic analyses of tumor-derived cells and/or lysates used for such vaccines (Mayer-Sonnenfeld et al., 2013). As a consequence, tumor cell sub-populations that down-regulate a particular antigen are likely to retain other antigens capable of attracting and antagonizing key immune cells, including macrophages, to attack the tumor. These broader approaches thus seem robust compared to single antigen approaches.

Ultimately, this work motivates a potential extension wherein tumor CD47 expression is attenuated, perhaps by treatment with a CD47 siRNA followed shortly thereafter with a macrophage stimulating antibody. Such a scheme of CD47 siRNA delivery has already been shown to inhibit tumor growth and metastasis without systemic organ damage or anemia (Wang et al., 2013), but they did not treat established tumors nor did they infuse an antibody. Alternatively, recent work has shown the ability to generate a "probody" of

monoclonal antibody cetuximab (Desnoyers et al., 2013). Such a probody maintains the efficacy of cetuximab, but contains a protective linker that is cleaved by proteases typically found in abundance in the tumor microenvironment. It seems reasonable to propose a strategy wherein anti-CD47 antibody is generated with such protection, selectively binds tumor tissue, and then treated with a polyclonal opsonin. We thus have demonstrated a mechanism of macrophage stimulation and infiltration efficacious in the treatment of solid tumors in which the CD47-SIRPα interaction has been disrupted. Demonstration of the efficacy of a crude polyclonal antibody following CD47 expression reduction could open up a number of potentially cheaper, safer, and more efficient means of treating cancer.

Figure 4.S1. Preliminary studies of CD47 knockdown *in vitro* and *in vivo*

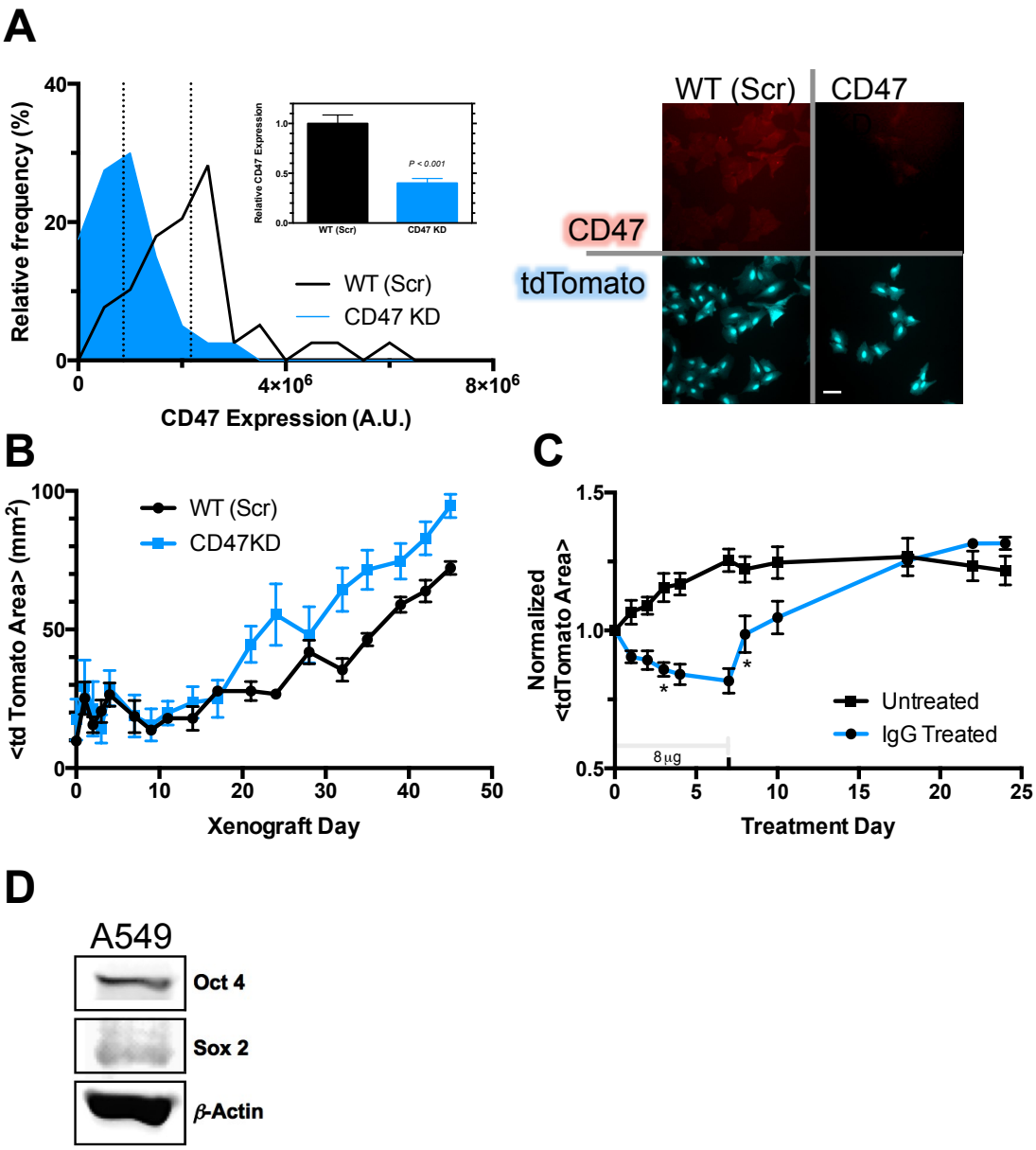

Figure 4.S1. Preliminary studies of CD47 knockdown *in vitro* and *in vivo*

(**A**) Quantification (left) of immunofluorescence (right) of WT Scr and CD47 KD tdTomato cells. (n≥40 cells per group. Scale bar = 10 μm) (**B**) *In vivo* growth curves of tdTomato xenografts in NSG flank. (n=2 mice, 4 tumors for all tumor types. Mean ± SEM) (**C**) Treatment of CD47 KD tumors from Fig. 4.S1C with polyclonal anti-human IgG antibody. (Treated: n=2 mice, 4 tumors; Untreated: n=3 mice, 6 tumors. **P*<0.05 within a cohort compared to the previous day. Mean ± SEM) (**D**) Western blot of A549 cells for pluripotency markers Oct4 and Sox2.

Figure 4.S2. Anti-human RBC antibody binding and initial treatment study

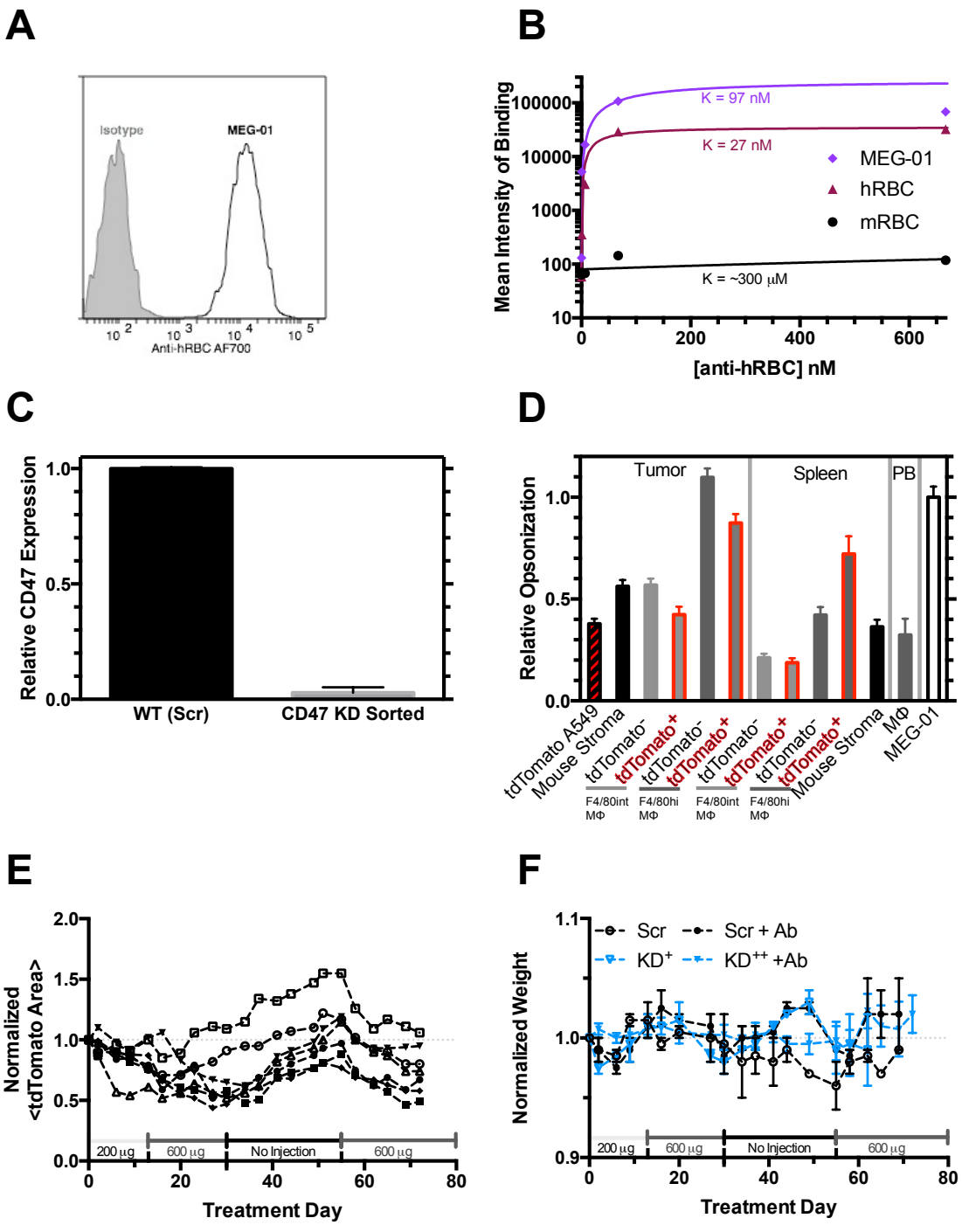

Figure 4.S2. Anti-human RBC antibody binding and initial treatment study

(**A**) Flow cytometry (gray=isotype control; black=MEG-01) of 67 nM Ab binding to MEG-01 cells. (**B**) Binding curve for Ab to human RBC (hRBC), mouse RBC (mRBC) and MEG-01 (a human megakaryocytic cell line). Fitting parameters indicate that when B is similar for mRBC and hRBC K for mRBC >> hRBC indicating weak affinity to mRBC. Mixing human and mouse RBCs did not effect binding to either species. Model: $Y=A+B*X/(K+X)$; hRBC: A=80, B=35524, K=26.5nM, R^2=0.97; mRBC: A=80, B=14210, K=323427nM, R^2=0.22; MEG-01: A=80, B=262480, K=97nM, R^2=0.99. (**C**) Quantification of CD47 following sorting to establish CD47 KD^+. (**D**) Relative average intensity of opsonization by Ab for various cell types and location (tumor, peripheral blood, and spleen). Intensity normalized to MEG-01 calibration (n>11 per group, Mean ± SEM). (**E**) Scatter plot of individual CD47 KD^+ treated tumors. (n=4 mice, 8 tumors). (**F**) Weight throughout treatment period. Weight is normalized to weight at date of treatment initiation. Mice used in CD47 KD^+ study.

Figure 4.S3 Ab + taxol treatment cytotoxicity, animal monitoring, and tumor assessment

A

	CV% = A +B /(1+10((log(conc)-log(IC_{50})))			
	A	B	IC_{50}	R^2
WT (Scr)	29.03	70.15	0.014	0.9784
CD47 KD^{++}	24.05	75.86	0.026	0.9693

B

		Mouse weight (g)		[Tax] (mg/kg)	
Injection date	[Taxol](ug/mL)	Scr Ab+TW	KD^{++} Ab+TW	Scr Ab+TW	KD^{++} Ab+TW
d0	710	30.7	30.7	4.63	4.63
d2	690	30.6	31.1	4.06	3.99
d6	730	30.3	30.5	4.82	4.79
d9	580	30.6	31.3	3.79	3.71

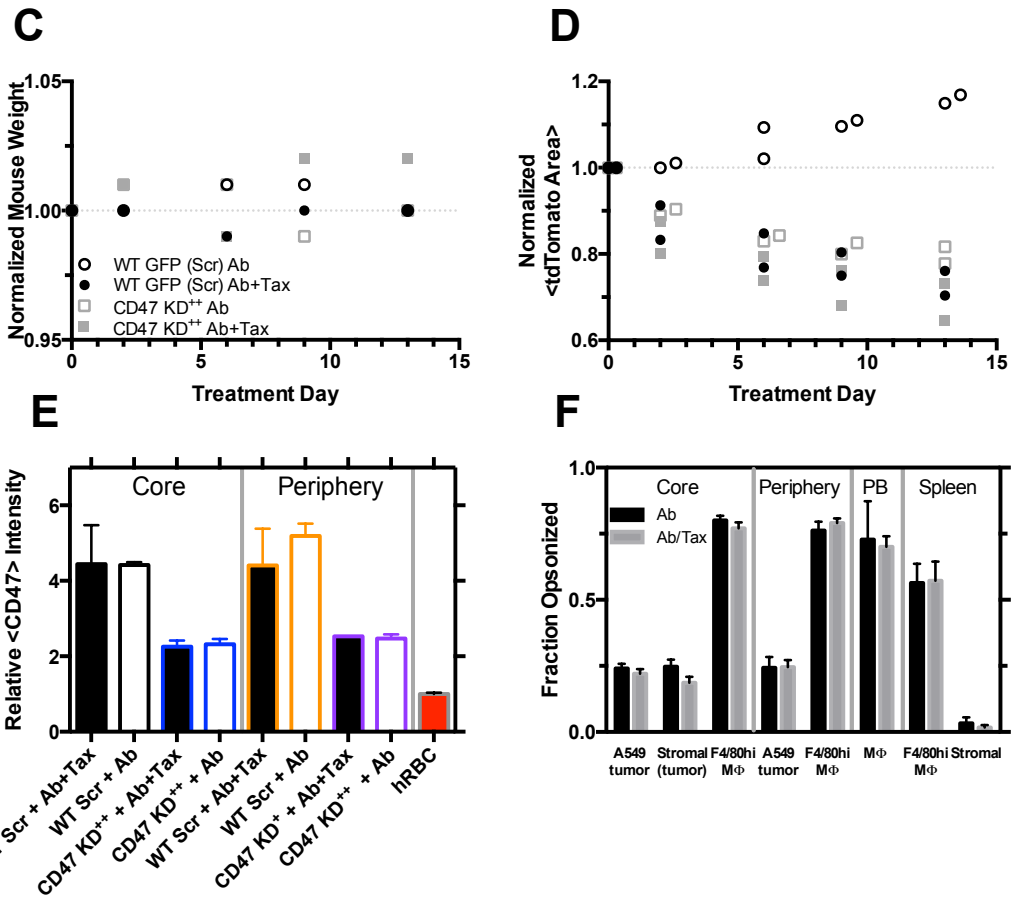

Figure 4.S3 Ab + taxol treatment cytotoxicity, animal monitoring, and tumor assessment

(**A**) Fitting parameters from *in vitro* cytotoxicity assay. (**B**) Summary of taxol doses delivered. (**C**) Monitoring of animal weight during co-therapy does not show any significant weight loss. Weight normalized to weight at initiation of co-therapy. (**D**) Individual tumor response presented in Fig. 3A. (**E**) Relative CD47 expression, normalized by human RBC, for Taxol Study tumors (n = 2 per group. Mean ± SEM). (**F**) Opsonization of various tissue types by Ab for Taxol study. Value represents the fraction of a given tissue type that is opsonized per tissue. ($n \geq 4$ tumors, n = 2 spleens per group. Mean ± SEM).

Figure 4.S4 Macrophage localization and population breakdown

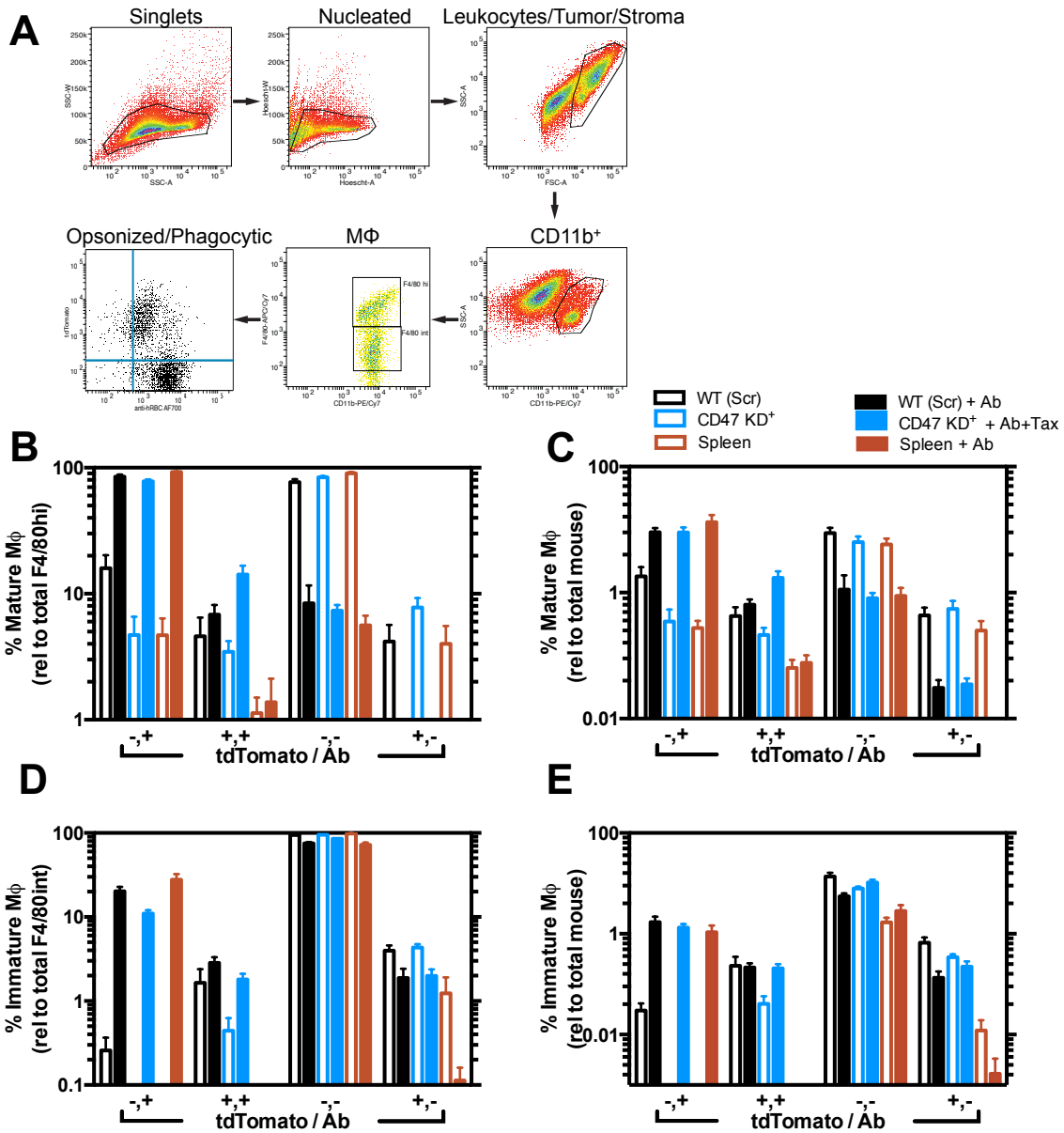

Figure 4.S4 Macrophage localization and population breakdown

(**A**) Flow cytometry gating strategy used to analyze mature ($CD11b^{+}F4/80hi$) and immature ($CD11b^{+}F4/80int$) macrophages. (**B-E**) Macrophage subpopulation analysis for CD47 KD^{+} study. (B) % mature macrophages relative to total mature macrophages in a given tissue/spleen (C) % mature macrophages relative to total murine cells in a given tissue/spleen. (D) % immature macrophages relative to total number of immature macrophages in a given tissue/spleen. (E) % mature macrophages relative to total murine cells in a given tissue/spleen ($n \geq 4$ tumors/spleens per group. Mean ± SEM).

Figure 4.S5 WT GFP Scr/KD^{++} mosaic tumor analysis

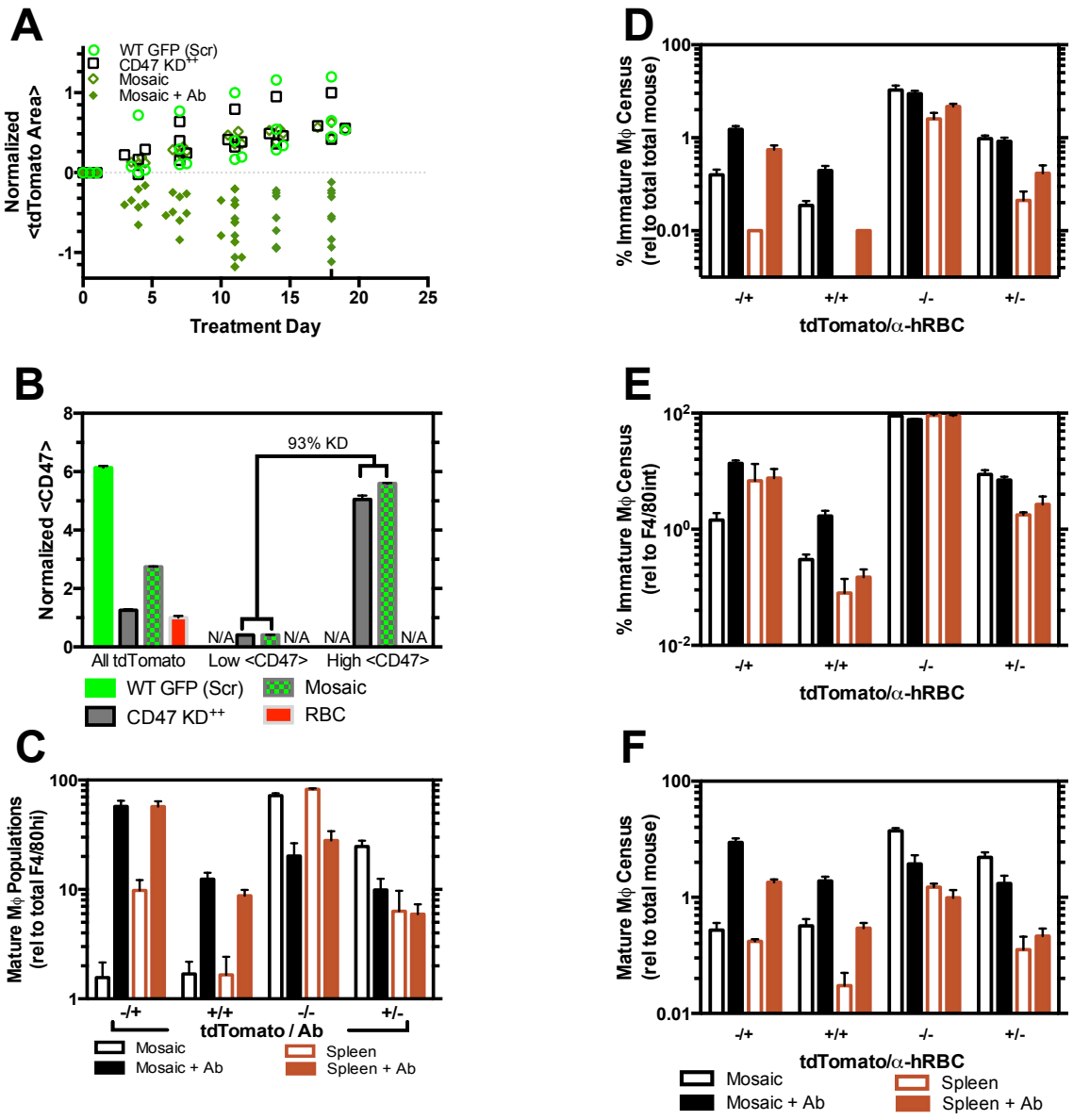

Figure 4.S5 WT GFP Scr/KD^{++} mosaic tumor analysis

(**A**) Scatter plot of individual tumors presented in Figure 1B. (WT GFP Scr: n=2 mice, 4 tumors; CD47 KD^{++}: n=2 mice, 4 tumors; Mosaic: n=6 mice, 12 tumors). (**B**) Flow cytometry of cells 1 day after xenograft implantation. CD47 intensity is normalized to human RBC. (n=3 for all groups. Mean ± SEM). (**C-F**) Macrophage subpopulation analysis of tumors shown in Fig. 1C, D. (C) % immature macrophages relative to total murine cells in a given tissue/spleen. (D) % immature macrophages relative to total number of immature macrophages in a given tissue/spleen. (E) % mature macrophages relative to total mature macrophages in a given tissue/spleen. (F) % mature macrophages relative to total murine cells in a given tissue/spleen ($n \geq 4$ tumors/spleens per group. Mean ± SEM).

CHAPTER 5: CONCLUSIONS AND FUTURE DIRECTIONS

The work presented in this dissertation provides evidence for specific roles of lamin-A and –B in HSC/P differentiation and trafficking of progeny. Additionally, specific roles for MIIA and MIIB in blood cell generation and long-term engraftment have been demonstrated. Temporal and spatial control of MIIA function has also been shown to be critical to MK proplatelet extension, fragmentation, and generation of platelets of normal size and number. Specifically, we have shown that the lamin-A:B ratio controls both nuclear viscoelasticity and cell trafficking. High A:B rigidifies erythroblast nuclei to favor marrow retention and enhance erythropoiesis. Thrombopoiesis is enhanced by intermediate A:B that also opposes cell division thereby favoring marrow anchorage of MKs. Moderate lamin levels are seen in HSC/Ps while white cells have low lamin levels thus contribute to marrow retention and circulation respectively. Our MII results in early hematopoiesis reveals MIIB to be highly polarized in HSC/Ps and as a result, is downregulated in differentiated cells through asymmetric division. The use of xenograft mouse models has shown that MIIB is required for generation of blood, MIIA is required for long-term HSC/P engraftment, and inhibition of either MII isoform with blebbistatin enriches for long-term hematopoietic multilineage reconstituting cells. Focusing on MKs and platelet generation, we have found an optimal shear stress for generation of platelet-like-particles that is enhanced by MII inhibition. Furthermore, phosphorylation at S1943 on the MIIA heavy chain is found to be shear stress sensitive. Micropipette aspiration confirms the enhancement in MK fragmentation following pharmacological inhibition or mutagenic means of introducing a phospho-mimetic mutation. Extending the work to *MYH9*-RD mutations, we recapitulate the macrothrombocytopenia *in vitro* using micropipette aspiration. Peripheral blood samples

from normal donors treated with blebbistatin is shown to arrest cleavage and generation of normal size platelets as seen by an increase in the number of large discoidal preplatelets. These blebbistatin treated blood samples share a striking resemblance to samples obtained from a *MYH9*-RD patient supporting our hypothesis that MIIA activity is necessary for fission of proplatelets to platelets. Without proper MIIA activity platelets are not released and a macrothrombocytopenia results. Thus, macrothrombocytopenia resulting from *MYH9* mutation is not an effect of pathologic MK extension or initial fragmentation, but rather arises from an inability of circulating preplatelets to undergo fission.

After the investigation of biophysical aspects of hematopoiesis in the marrow and PB in Chapters 2 and 3, Chapter 4 explored the ability of leukocytes respond to the presence of a tumor and how one subset, the macrophage, can drive tumor clearance. The Discher laboratory's previous work with evading macrophage phagocytosis by display of a CD47 peptide (Rodriguez et al., 2013) provided the foundation from which the work presented herein built off. Others have previously demonstrated efficacious treatment regimens by combining an anti-CD47 antibody (Chao et al., 2010a) or an engineered SIRPα variant (Weiskopf et al., 2013) with a monoclonal tumor-specific antibody. However, since CD47 is nearly ubiquitously expressed on all cells, these treatment methods are typically accompanied by anemia and other adverse hematological side effects. Additionally, evidence exists for tumor clearance being driven by macrophages, but a direct observation of macrophages internalizing tumor cells is lacking. We proposed that if CD47 is blocked or knocked down on the tumor cell then any IgG antibody capable of opsonizing the surface of the tumor would be sufficient to stimulate

phagocytosis by macrophages. We, in fact, see such an effect. Treatment of mice bearing human xenograft tumors with CD47 expression knocked down showed drastic reduction in tumor size following administration of a general human specific polyclonal antibody while tumors expressing normal levels of CD47 were unaffected by treatment. Additionally, significant adverse hematological side effects are not observed. By spiking a known fraction of GFP-expressing normal CD47 cells into our CD47 knockdown tumors we observe an enrichment of GFP cells after Ab treatment demonstrated upon tumor excision indicating, the selective removal of CD47 knockdown cells. Macrophages from CD47 knockdown Ab treated tumors show an increase in the presence of tdTomato (fluorescent protein expressed by tumor cells) and co-localization is increased when macrophages are also positive for the Ab. These observations provide direct evidence that macrophages are engaging the CD47 knockdown cells, being further stimulated to eat by the treatment antibody, and then proceed to phagocytose the target cell.

The results of these recent tumor studies provide the potential for an efficacious treatment without significant side-effects. Granted, we are starting with tumors in which CD47 is already knocked down, whereas normal tumors typically express elevated levels of CD47 (Majeti et al., 2009). Methods of delivering siRNA directed toward CD47 may prove to be the solution. Other have delivered liposomes containing CD47 siRNA and have shown inhibition of tumor establishment without hematopoietic toxicity (Wang et al., 2013). However, siRNA was not delivered to animals carrying already established tumors, siRNA was administered concurrently with tumor inoculation, nor did they simultaneously treat with an antibody. Our laboratory is in the early stages of developing a non-toxic siRNA against CD47 that we would use in our xenograft tumor model and

accompany with antibody treatment. siRNA seems to be a safe and efficacious means of tumor CD47 knockdown as anucleated RBCs and platelets would be unaffected by siRNA. There is a possibility of siRNA incorporating into circulating leukocytes, marrow cells, or even the endothelium lining the circulation. Incorporation into HSC/Ps could be particularly harmful as the progeny of these cells would also display reduced CD47 levels and be rapidly phagocytosed as they frequently encounter macrophages in the circulation. These potential issues could be resolved by proper delivery design, dosing schedule, and/or specificity in targeting only tumor cells.

A second study that we are currently undertaking is the generation of an Fc truncated version of the treatment antibody. Others have demonstrated that $F(ab')_2$ fragments of anti-cancer antibodies are capable of binding tumor cells with similar affinity as their full length version, however, the loss of the Fc portion abrogates macrophage engagement and thus treatment efficacy is greatly impaired (Pallasch et al., 2014). We hope to show similar effects *in vitro* and *in vivo* using our xenograft model. If successful, it will prove that CD47 knockdown removes the normal "don't eat me" signal through interaction with SIRPα while the presence of the treatment antibody provides an additional "eat me" stimulus through engagement of the Fc receptor on the macrophage.

Another potentially exciting avenue that may be pursued is the generation of a anti-CD47 probody similar to the cetuximab analog developed recently by CytomX Therapeutics. The cetuximab probody, an anti-epidermal growth factor receptor antibody, is synthesized with a masking peptide linked to the Fab arm of the antibody that is cleaved by proteases commonly found in the tumor microenvironment. They show reduced EGFR binding and inhibitory activity of the probody, but upon cleavage, binding

and inhibitory activity is similar to cetuximab (Desnoyers et al., 2013). We hypothesize that instead of using CD47 siRNA or unprotected anti-CD47 antibodies that would interact with normal tissue as well as cancerous tissue, we would generate a protected anti-CD47 antibody that can only be deprotected in the tumor microenvironment. Simultaneous administration of polyclonal IgG would then provide the additional stimulatory signal necessary for efficient macrophage clearance of CD47 masked, IgG opsonized cancer cells.

In total, the work presented in this dissertation and the efforts currently being undertaken demonstrate significant contributions to the understanding of biophysical principles in hematopoiesis through lamin and MII. Using a combination of *in vitro* and *in vivo* methods as well as patient samples, we were able to provide insight into the roles of lamin-A and –B in HSC/P differentiation and trafficking, MIIA and MIIB in generation of blood cells and long-term engraftment, and MK fragmentation and platelet generation. We additionally provide a mechanism for understanding CD47 modulated antibody treatment of cancer through phagocytosis of tumor cells by macrophages. Such a treatment option may prove applicable beyond the NSG mouse, but for now it offers an *in vivo* means of exploring immunotherapy and a platform from which we can explore less harmful treatment options than chemotherapy and radiation.

REFERENCES

Adamo, L., Naveiras, O., Wenzel, P.L., McKinney-Freeman, S., Mack, P.J., Gracia-Sancho, J., Suchy-Dicey, A., Yoshimoto, M., Lensch, M.W., Yoder, M.C., et al. (2009). Biomechanical forces promote embryonic haematopoiesis. Nature *459*, 1131–1135.

Adelstein, R.S., Conti, M.A., Johnson, G.S., Pastan, I., and Pollard, T.D. (1972). Isolation and characterization of myosin from cloned mouse fibroblasts. Proc. Natl. Acad. Sci. U. S. A. *69*, 3693–3697.

Alberts, B., Johnson, A., Lewis, J., Martin, R., Roberts, K., and Walter, P. (2007). Molecular Biology of the Cell (New York: Garland Science).

Andrade, R., Alonso, R., Peña, R., Arlucea, J., and Aréchaga, J. (2003). Localization of importin alpha (Rch1) at the plasma membrane and subcellular redistribution during lymphocyte activation. Chromosoma *112*, 87–95.

Andzelm, M.M., Chen, X., Krzewski, K., Orange, J.S., and Strominger, J.L. (2007). Myosin IIA is required for cytolytic granule exocytosis in human NK cells. J. Exp. Med. *204*, 2285–2291.

Apostolidis, P. a, Lindsey, S., Miller, W.M., and Papoutsakis, E.T. (2012). Proposed megakaryocytic regulon of p53: the genes engaged to control cell cycle and apoptosis during megakaryocytic differentiation. Physiol. Genomics *44*, 638–650.

Balduini, C.L., Pecci, A., and Savoia, A. (2011). Recent advances in the understanding and management of MYH9-related inherited thrombocytopenias. Br. J. Haematol. *154*, 161–174.

Basu, S., Hodgson, G., Katz, M., and Dunn, A.R. (2002). Evaluation of role of G-CSF in the production, survival, and release of neutrophils from bone marrow into circulation. Blood *100*, 854–861.

Baumann, B.C., Kao, G.D., Mahmud, A., Harada, T., Swift, J., Chapman, C., Xu, X., Discher, D.E., and Dorsey, J.F. (2013). Enhancing the efficacy of drug-loaded nanocarriers against brain tumors by targeted radiation therapy. Oncotarget *4*, 64–79.

Beach, J.R., Hussey, G.S., Miller, T.E., Chaudhury, A., Patel, P., Monslow, J., Zheng, Q., Keri, R. a, Reizes, O., Bresnick, A.R., et al. (2011). Myosin II isoform switching mediates invasiveness after TGF-β-induced epithelial-mesenchymal transition. Proc. Natl. Acad. Sci. U. S. A. *108*, 17991–17996.

Becker, A.J., McCulloch, E.A., and Till, J.E. (1963). Cytological demonstration of the clonal nature of spleen colonies derived from transplanted mouse marrow cells. Nature *197*, 452–454.

Beckmann, J., Scheitza, S., Wernet, P., Fischer, J.C., and Giebel, B. (2007). Asymmetric cell division within the human hematopoietic stem and progenitor cell compartment: identification of asymmetrically segregating proteins. Blood *109*, 5494–5501.

Ben-Ze'ev, a, and Raz, a (1981). Multinucleation and inhibition of cytokinesis in suspended cells: reversal upon reattachment to a substrate. Cell *26*, 107–115.

Blazar, B.R., Lindberg, F.P., Ingulli, E., Panoskaltsis-Mortari, a, Oldenborg, P. a, Iizuka, K., Yokoyama, W.M., and Taylor, P. a (2001). CD47 (integrin-associated protein) engagement of dendritic cell and macrophage counterreceptors is required to prevent the clearance of donor lymphohematopoietic cells. J. Exp. Med. *194*, 541–549.

Bluteau, D., Glembotsky, A.C., Raimbault, A., Balayn, N., Gilles, L., Rameau, P., Nurden, P., Alessi, M.C., Debili, N., Vainchenker, W., et al. (2012). Dysmegakaryopoiesis of FPD/AML pedigrees with constitutional RUNX1 mutations is linked to myosin II deregulated expression. Blood *120*, 2708–2718.

Brown, E.J., and Frazier, W.A. (2001). Integrin-associated protein (CD47) and its ligands. Trends Cell Biol. *11*, 130–135.

Cai, S., Vijayan, K., Cheng, D., Lima, E.M., and Discher, D.E. (2007). Micelles of different morphologies--advantages of worm-like filomicelles of PEO-PCL in paclitaxel delivery. Pharm. Res. *24*, 2099–2109.

Campbell, I.G., Freemont, P.S., Foulkes, W., and Trowsdale, J. (1992). An ovarian tumor marker with homology to vaccinia virus contains an IgV-like region and multiple transmembrane domains. Cancer Res. *52*, 5416–5420.

Canman, J.C., Cameron, L.A., Maddox, P.S., Straight, A., Tirnauer, J.S., Mitchison, T.J., Fang, G., Kapoor, T.M., and Salmon, E.D. (2003). Determining the position of the cell division plane. Nature *424*, 1074–1078.

Canobbio, I., Noris, P., Pecci, a, Balduini, a, Balduini, C.L., and Torti, M. (2005). Altered cytoskeleton organization in platelets from patients with MYH9-related disease. J. Thromb. Haemost. *3*, 1026–1035.

Celik, M., Bulbul, A., Aydogan, G., Tugcu, D., Can, E., Uslu, S., and Dursun, M. (2013). Comparison of anti-D immunoglobulin, methylprednisolone, or intravenous immunoglobulin therapy in newly diagnosed pediatric immune thrombocytopenic purpura. J. Thromb. Thrombolysis *35*, 228–233.

Chan, K.S., Espinosa, I., Chao, M., Wong, D., Ailles, L., Diehn, M., Gill, H., Presti, J., Chang, H.Y., van de Rijn, M., et al. (2009). Identification, molecular characterization, clinical prognosis, and therapeutic targeting of human bladder tumor-initiating cells. Proc. Natl. Acad. Sci. U. S. A. *106*, 14016–14021.

Chao, M.P., Alizadeh, A. a, Tang, C., Myklebust, J.H., Varghese, B., Gill, S., Jan, M., Cha, A.C., Chan, C.K., Tan, B.T., et al. (2010a). Anti-CD47 antibody synergizes with rituximab to promote phagocytosis and eradicate non-Hodgkin lymphoma. Cell *142*, 699–713.

Chao, M.P., Jaiswal, S., Weissman-Tsukamoto, R., Alizadeh, A. a, Gentles, A.J., Volkmer, J., Weiskopf, K., Willingham, S.B., Raveh, T., Park, C.Y., et al. (2010b). Calreticulin is the dominant pro-phagocytic signal on multiple human cancers and is counterbalanced by CD47. Sci. Transl. Med. *2*, 63ra94.

Chao, M.P., Alizadeh, A. a, Tang, C., Jan, M., Weissman-Tsukamoto, R., Zhao, F., Park, C.Y., Weissman, I.L., and Majeti, R. (2011a). Therapeutic antibody targeting of CD47 eliminates human acute lymphoblastic leukemia. Cancer Res. *71*, 1374–1384.

Chao, M.P., Tang, C., Pachynski, R.K., Chin, R., Majeti, R., and Weissman, I.L. (2011b). Extranodal dissemination of non-Hodgkin lymphoma requires CD47 and is inhibited by anti-CD47 antibody therapy. Blood *118*, 4890–4901.

Chen, B.P.C., Li, Y., Zhao, Y., Chen, K., Li, S., Lao, J., Yuan, S., Shyy, J.Y., Chien, S.H.U., Swift, J., et al. (2001). DNA microarray analysis of gene expression in endothelial cells in response to 24-h shear stress DNA microarray analysis of gene expression in endothelial cells in response to 24-h shear stress. Physiol. Genomics *7*, 55–63.

Chen, G., Hou, Z., Gulbranson, D.R., and Thomson, J. a (2010). Actin-myosin contractility is responsible for the reduced viability of dissociated human embryonic stem cells. Cell Stem Cell *7*, 240–248.

Chen, M.J., Yokomizo, T., Zeigler, B.M., Dzierzak, E., and Speck, N. a (2009). Runx1 is required for the endothelial to haematopoietic cell transition but not thereafter. Nature *457*, 887–891.

Chen, Y., Boukour, S., Milloud, R., Favier, R., Saposnik, B., Schlegel, N., Nurden, A., Raslova, H., Vainchenker, W., Balland, M., et al. (2013). The abnormal proplatelet formation in MYH9-related macrothrombocytopenia results from an increased actomyosin contractility and is rescued by myosin IIA inhibition. J. Thromb. Haemost. 2163–2175.

Chen, Z., Naveiras, O., Balduini, A., Mammoto, A., Conti, M.A., Adelstein, R.S., Ingber, D., Daley, G.Q., and Shivdasani, R. a (2007). The May-Hegglin anomaly gene MYH9 is

a negative regulator of platelet biogenesis modulated by the Rho-ROCK pathway. Blood *110*, 171–179.

Chowdhury, F., Na, S., Li, D., Poh, Y.-C., Tanaka, T.S., Wang, F., and Wang, N. (2010). Material properties of the cell dictate stress-induced spreading and differentiation in embryonic stem cells. Nat. Mater. *9*, 82–88.

Christian, D.A., Cai, S., Garbuzenko, O.B., Harada, T., Zajac, A.L., Minko, T., and Discher, D.E. (2009). Flexible filaments for in vivo imaging and delivery: persistent circulation of filomicelles opens the dosage window for sustained tumor shrinkage. Mol. Pharm. *6*, 1343–1352.

Cicalese, A., Bonizzi, G., Pasi, C.E., Faretta, M., Ronzoni, S., Giulini, B., Brisken, C., Minucci, S., Di Fiore, P.P., and Pelicci, P.G. (2009). The tumor suppressor p53 regulates polarity of self-renewing divisions in mammary stem cells. Cell *138*, 1083–1095.

Clark, K., Langeslag, M., van Leeuwen, B., Ran, L., Ryazanov, A.G., Figdor, C.G., Moolenaar, W.H., Jalink, K., and van Leeuwen, F.N. (2006). TRPM7, a novel regulator of actomyosin contractility and cell adhesion. EMBO J. *25*, 290–301.

Clynes, R. a, Towers, T.L., Presta, L.G., and Ravetch, J. V (2000). Inhibitory Fc receptors modulate in vivo cytotoxicity against tumor targets. Nat. Med. *6*, 443–446.

Coiffier, B., Lepage, E., Briere, J., Herbrecht, R., Tilly, H., Bouabdallah, R., Morel, P., Van Den Neste, E., Salles, G., Gaulard, P., et al. (2002). CHOP chemotherapy plus rituximab compared with CHOP alone in elderly patients with diffuse large-B-cell lymphoma. N. Engl. J. Med. *346*, 235–242.

Condeelis, J., and Pollard, J.W. (2006). Macrophages: obligate partners for tumor cell migration, invasion, and metastasis. Cell *124*, 263–266.

Conti, M.A., Even-Ram, S., Liu, C., Yamada, K.M., and Adelstein, R.S. (2004). Defects in cell adhesion and the visceral endoderm following ablation of nonmuscle myosin heavy chain II-A in mice. J. Biol. Chem. *279*, 41263–41266.

Dahl, K.N., Scaffidi, P., Islam, M.F., Yodh, A.G., Wilson, K.L., and Misteli, T. (2006). Distinct structural and mechanical properties of the nuclear lamina in Hutchinson-Gilford progeria syndrome. Proc. Natl. Acad. Sci. U. S. A. *103*, 10271–10276.

Daley, G.Q., and Scadden, D.T. (2008). Prospects for stem cell-based therapy. Cell *132*, 544–548.

Dechat, T., Adam, S. a, Taimen, P., Shimi, T., and Goldman, R.D. (2010). Nuclear lamins. Cold Spring Harb. Perspect. Biol. *2*, a000547.

Desnoyers, L.R., Vasiljeva, O., Richardson, J.H., Yang, A., Menendez, E.E.M., Liang, T.W., Wong, C., Bessette, P.H., Kamath, K., Moore, S.J., et al. (2013). Tumor-specific activation of an EGFR-targeting probody enhances therapeutic index. Sci. Transl. Med. *5*, 207ra144.

Deutsch, S., Rideau, A., Bochaton-Piallat, M.-L., Merla, G., Geinoz, A., Gabbiani, G., Schwede, T., Matthes, T., Antonarakis, S.E., and Beris, P. (2003). Asp1424Asn MYH9 mutation results in an unstable protein responsible for the phenotypes in May-Hegglin anomaly/Fechtner syndrome. Blood *102*, 529–534.

Discher, D., Mohandas, N., and Evans, E. (1994). Molecular maps of red cell deformation: hidden elasticity and in situ connectivity. Science (80-.). *266*, 1032–1035.

Discher, D.E., Janmey, P., and Wang, Y.-L. (2005). Tissue cells feel and respond to the stiffness of their substrate. Science *310*, 1139–1143.

Dong, C., Skalak, R., and Sung, K.L. (1991). Cytoplasmic rheology of passive neutrophils. Biorheology *28*, 557–567.

Dougan, M., and Dranoff, G. (2009). Immune therapy for cancer. Annu. Rev. Immunol. *27*, 83–117.

Doulatov, S., Notta, F., Laurenti, E., and Dick, J.E. (2012). Hematopoiesis: a human perspective. Cell Stem Cell *10*, 120–136.

Dulyaninova, N.G., Malashkevich, V.N., Almo, S.C., and Bresnick, A.R. (2005). Regulation of myosin-IIA assembly and Mts1 binding by heavy chain phosphorylation. Biochemistry *44*, 6867–6876.

Dupont, S., Morsut, L., Aragona, M., Enzo, E., Giulitti, S., Cordenonsi, M., Zanconato, F., Le Digabel, J., Forcato, M., Bicciato, S., et al. (2011). Role of YAP/TAZ in mechanotransduction. Nature *474*, 179–183.

Eckly, A., Strassel, C., Freund, M., Cazenave, J.-P., Lanza, F., Gachet, C., and Léon, C. (2009). Abnormal megakaryocyte morphology and proplatelet formation in mice with megakaryocyte-restricted MYH9 inactivation. Blood *113*, 3182–3189.

Eckly, A., Rinckel, J.-Y., Laeuffer, P., Cazenave, J.-P., Lanza, F., Gachet, C., and Léon, C. (2010). Proplatelet formation deficit and megakaryocyte death contribute to thrombocytopenia in Myh9 knockout mice. J. Thromb. Haemost. *8*, 2243–2251.

Engler, A.J., Griffin, M. a, Sen, S., Bönnemann, C.G., Sweeney, H.L., and Discher, D.E. (2004). Myotubes differentiate optimally on substrates with tissue-like stiffness: pathological implications for soft or stiff microenvironments. J. Cell Biol. *166*, 877–887.

Engler, A.J., Sen, S., Sweeney, H.L., and Discher, D.E. (2006). Matrix elasticity directs stem cell lineage specification. Cell *126*, 677–689.

Engler, A.J., Carag-Krieger, C., Johnson, C.P., Raab, M., Tang, H.-Y., Speicher, D.W., Sanger, J.W., Sanger, J.M., and Discher, D.E. (2008). Embryonic cardiomyocytes beat best on a matrix with heart-like elasticity: scar-like rigidity inhibits beating. J. Cell Sci. *121*, 3794–3802.

Engström, K.G., and Löfvenberg, E. (1998). Treatment of myeloproliferative disorders with hydroxyurea: effects on red blood cell geometry and deformability. Blood *91*, 3986–3991.

Even-Faitelson, L., and Ravid, S. (2006). PAK1 and aPKCzeta regulate myosin II-B phosphorylation: a novel signaling pathway regulating filament assembly. Mol. Biol. Cell *17*, 2869–2881.

Faure-André, G., Vargas, P., Yuseff, M., Heuzé, M., Diaz, J., Lankar, D., Steri, V., Manry, J., Hugues, S., Vascotto, F., et al. (2008). Regulation of dendritic cell migration by CD74, the MHC class II-associated invariant chain. Science *322*, 1705–1710.

Fernandez, M., Heuzé, M.L., Martinez-Cingolani, C., Volpe, E., Donnadieu, M., Piel, M., Homey, B., Lennon-Duménil, A.-M., and Soumelis, V. (2011). The human cytokine TSLP triggers a cell-autonomous dendritic cell migration in confined environments. Blood *118*, 3862–3869.

Florian, M.C., Dörr, K., Niebel, A., Daria, D., Schrezenmeier, H., Rojewski, M., Filippi, M.-D., Hasenberg, A., Gunzer, M., Scharffetter-Kochanek, K., et al. (2012). Cdc42 activity regulates hematopoietic stem cell aging and rejuvenation. Cell Stem Cell *10*, 520–530.

Franke, J.D., Dong, F., Rickoll, W.L., Kelley, M.J., and Kiehart, D.P. (2005). Rod mutations associated with MYH9-related disorders disrupt nonmuscle myosin-IIA assembly. Blood *105*, 161–169.

Frost, H.M. (1987). Bone "mass" and the "mechanostat": a proposal. Anat. Rec. *219*, 1–9.

Fulcher, D. a, and Basten, a (1997). B cell life span: a review. Immunol. Cell Biol. *75*, 446–455.

Funada, Y., Noguchi, T., Kikuchi, R., Takeno, S., Uchida, Y., and Gabbert, H.E. (2003). Prognostic significance of CD8+ T cell and macrophage peritumoral infiltration in colorectal cancer. Oncol. Rep. *10*, 309–313.

Van Furth, R., and Cohn, Z. a (1968). The origin and kinetics of mononuclear phagocytes. J. Exp. Med. *128*, 415–435.

Gardai, S.J., McPhillips, K. a, Frasch, S.C., Janssen, W.J., Starefeldt, A., Murphy-Ullrich, J.E., Bratton, D.L., Oldenborg, P.-A., Michalak, M., and Henson, P.M. (2005). Cell-surface calreticulin initiates clearance of viable or apoptotic cells through trans-activation of LRP on the phagocyte. Cell *123*, 321–334.

Georges, P.C., Miller, W.J., Meaney, D.F., Sawyer, E.S., and Janmey, P. a (2006). Matrices with compliance comparable to that of brain tissue select neuronal over glial growth in mixed cortical cultures. Biophys. J. *90*, 3012–3018.

Gerner, C., and Sauermann, G. (1999). Nuclear matrix proteins specific for subtypes of human hematopoietic cells. J. Cell. Biochem. *72*, 470–482.

Gett, a V, and Hodgkin, P.D. (2000). A cellular calculus for signal integration by T cells. Nat. Immunol. *1*, 239–244.

Gilbert, P.M., Havenstrite, K.L., Magnusson, K.E.G., Sacco, a, Leonardi, N. a, Kraft, P., Nguyen, N.K., Thrun, S., Lutolf, M.P., and Blau, H.M. (2010). Substrate elasticity regulates skeletal muscle stem cell self-renewal in culture. Science *329*, 1078–1081.

Giordano, G.F., and Lichtman, M.A. (1973). Marrow cell egress. The central interaction of barrier pore size and cell maturation. J. Clin. Invest. *52*, 1154–1164.

Godwin, H.A., and Ginsburg, A.D. (1974). May-Hegglin anomaly: a defect in megakaryocyte fragmentation? Br. J. Haematol. *26*, 117–128.

Gratwohl, A., Baldomero, H., Aljurf, M., Pasquini, M.C., Bouzas, L.F., Yoshimi, A., Szer, J., Lipton, J., Schwendener, A., Gratwohl, M., et al. (2010). Hematopoietic stem cell transplantation: a global perspective. JAMA *303*, 1617–1624.

Guilly, M.N., Kolb, J.P., Gosti, F., Godeau, F., and Courvalin, J.C. (1990). Lamins A and C are not expressed at early stages of human lymphocyte differentiation. Exp. Cell Res. *189*, 145–147.

Guminski, A.D., Harnett, P.R., and DeFazio, A. (2001). Carboplatin and paclitaxel interact antagonistically in a megakaryoblast cell line--a potential mechanism for paclitaxel-mediated sparing of carboplatin-induced thrombocytopenia. Cancer Chemother. Pharmacol. *48*, 229–234.

Hale, J.S., Frock, R.L., Mamman, S. a, Fink, P.J., and Kennedy, B.K. (2010). Cell-extrinsic defective lymphocyte development in Lmna(-/-) mice. PLoS One *5*, e10127.

Hallek, M., Fischer, K., Fingerle-Rowson, G., Fink, a M., Busch, R., Mayer, J., Hensel, M., Hopfinger, G., Hess, G., von Grünhagen, U., et al. (2010). Addition of rituximab to fludarabine and cyclophosphamide in patients with chronic lymphocytic leukaemia: a randomised, open-label, phase 3 trial. Lancet *376*, 1164–1174.

Harada, T., Swift, J., Irianto, J., Shin, J.-W., Spinler, K.R., Athirasala, A., Diegmiller, R., Dingal, P.C.D.P., Ivanovska, I.L., and Discher, D.E. (2014). Nuclear lamin stiffness is a barrier to 3D migration, but softness can limit survival. J. Cell Biol. *204*, 669–682.

Hategan, A., Law, R., Kahn, S., and Discher, D.E. (2003). Adhesively-tensed cell membranes: lysis kinetics and atomic force microscopy probing. Biophys. J. *85*, 2746–2759.

Hernandez, O.M., Jones, M., Guzman, G., and Szczesna-Cordary, D. (2007). Myosin essential light chain in health and disease. Am. J. Physiol. Heart Circ. Physiol. *292*, H1643–54.

Hernandez-Ilizaliturri, F.J., Jupudy, V., Reising, S., Repasky, E.A., and Czuczman, M.S. (2005). Concurrent administration of granulocyte colony-stimulating factor or granulocyte-monocyte colony-stimulating factor enhances the biological activity of rituximab in a severe combined immunodeficiency mouse lymphoma model. Leuk. Lymphoma *46*, 1775–1784.

Holst, J., Watson, S., Lord, M.S., Eamegdool, S.S., Bax, D. V, Nivison-Smith, L.B., Kondyurin, A., Ma, L., Oberhauser, A.F., Weiss, A.S., et al. (2010). Substrate elasticity provides mechanical signals for the expansion of hemopoietic stem and progenitor cells. Nat. Biotechnol. *28*, 1123–1128.

Huebsch, N., Arany, P.R., Mao, A.S., Shvartsman, D., Ali, O. a, Bencherif, S. a, Rivera-Feliciano, J., and Mooney, D.J. (2010). Harnessing traction-mediated manipulation of the cell/matrix interface to control stem-cell fate. Nat. Mater. *9*, 518–526.

Ilani, T., Vasiliver-Shamis, G., Vardhana, S., Bretscher, A., and Dustin, M.L. (2009). T cell antigen receptor signaling and immunological synapse stability require myosin IIA. Nat. Immunol. *10*, 531–539.

Italiano, J.E., Lecine, P., Shivdasani, R. a, and Hartwig, J.H. (1999). Blood platelets are assembled principally at the ends of proplatelet processes produced by differentiated megakaryocytes. J. Cell Biol. *147*, 1299–1312.

Ivanovska, I., Swift, J., Harada, T., Pajerowski, J.D., and Discher, D.E. (2010). Physical plasticity of the nucleus and its manipulation. (Elsevier Inc.).

Jacobelli, J., Friedman, R.S., Conti, M.A., Lennon-Dumenil, A.-M., Piel, M., Sorensen, C.M., Adelstein, R.S., and Krummel, M.F. (2010). Confinement-optimized three-

dimensional T cell amoeboid motility is modulated via myosin IIA-regulated adhesions. Nat. Immunol. *11*, 953–961.

Jahn, D., Schramm, S., Schnölzer, M., Heilmann, C.J., de Koster, C.G., Schütz, W., Benavente, R., and Alsheimer, M. (2012). A truncated lamin A in the Lmna -/- mouse line: implications for the understanding of laminopathies. Nucleus *3*, 463–474.

Jaiswal, S., Jamieson, C.H.M., Pang, W.W., Park, C.Y., Chao, M.P., Majeti, R., Traver, D., van Rooijen, N., and Weissman, I.L. (2009). CD47 is upregulated on circulating hematopoietic stem cells and leukemia cells to avoid phagocytosis. Cell *138*, 271–285.

Junt, T., Schulze, H., Chen, Z., Massberg, S., Goerge, T., Krueger, A., Wagner, D.D., Graf, T., Italiano, J.E., Shivdasani, R. a, et al. (2007). Dynamic visualization of thrombopoiesis within bone marrow. Science *317*, 1767–1770.

Kaur, S., Soto-Pantoja, D.R., Stein, E. V, Liu, C., Elkahloun, A.G., Pendrak, M.L., Nicolae, A., Singh, S.P., Nie, Z., Levens, D., et al. (2013). Thrombospondin-1 signaling through CD47 inhibits self-renewal by regulating c-Myc and other stem cell transcription factors. Sci. Rep. *3*, 1673.

Kaushansky, K., Lok, S., Holly, R.D., Broudy, V.C., Lin, N., Bailey, M.C., Forstrom, J.W., Buddle, M.M., Oort, P.J., and Hagen, F.S. (1994). Promotion of megakaryocyte progenitor expansion and differentiation by the c-Mpl ligand thrombopoietin. Nature *369*, 568–571.

Kelley, M.J., Jawien, W., Ortel, T.L., and Korczak, J.F. (2000). Mutation of MYH9, encoding non-muscle myosin heavy chain A, in May-Hegglin anomaly. Nat. Genet. *26*, 106–108.

Kiel, M.J., Yilmaz, O.H., Iwashita, T., Yilmaz, O.H., Terhorst, C., and Morrison, S.J. (2005). SLAM family receptors distinguish hematopoietic stem and progenitor cells and reveal endothelial niches for stem cells. Cell *121*, 1109–1121.

Kikuchi, Y., Uno, S., Kinoshita, Y., Yoshimura, Y., Iida, S.-I., Wakahara, Y., Tsuchiya, M., Yamada-Okabe, H., and Fukushima, N. (2005). Apoptosis inducing bivalent single-chain antibody fragments against CD47 showed antitumor potency for multiple myeloma. Leuk. Res. *29*, 445–450.

Kim, Y., Sharov, A.A., McDole, K., Cheng, M., Hao, H., Fan, C.-M., Gaiano, N., Ko, M.S.H., and Zheng, Y. (2011). Mouse B-type lamins are required for proper organogenesis but not by embryonic stem cells. Science *334*, 1706–1710.

Klein, E. a, Yin, L., Kothapalli, D., Castagnino, P., Byfield, F.J., Xu, T., Levental, I., Hawthorne, E., Janmey, P. a, and Assoian, R.K. (2009). Cell-cycle control by physiological matrix elasticity and in vivo tissue stiffening. Curr. Biol. *19*, 1511–1518.

Klein-Schneegans, a S., Kuntz, L., Fonteneau, P., and Loor, F. (1989). Serum concentrations of IgM, IgG1, IgG2b, IgG3 and IgA in C57BL/6 mice and their congenics at the lpr (lymphoproliferation) locus. J. Autoimmun. *2*, 869–875.

Knoblich, J. a (2010). Asymmetric cell division: recent developments and their implications for tumour biology. Nat. Rev. Mol. Cell Biol. *11*, 849–860.

Knowles, D.W., Tilley, L., Mohandas, N., and Chasis, J.A. (1997). Erythrocyte membrane vesiculation: model for the molecular mechanism of protein sorting. Proc. Natl. Acad. Sci. U. S. A. *94*, 12969–12974.

Kong, H.J., Polte, T.R., Alsberg, E., and Mooney, D.J. (2005). FRET measurements of cell-traction forces and nano-scale clustering of adhesion ligands varied by substrate stiffness. Proc. Natl. Acad. Sci. U. S. A. *102*, 4300–4305.

Koury, S.T., Koury, M.J., and Bondurant, M.C. (1989). Cytoskeletal distribution and function during the maturation and enucleation of mammalian erythroblasts. J. Cell Biol. *109*, 3005–3013.

Krauss, S.W., Lo, A.J., Short, S.A., Koury, M.J., Mohandas, N., and Chasis, J.A. (2005). Nuclear substructure reorganization during late-stage erythropoiesis is selective and does not involve caspase cleavage of major nuclear substructural proteins. Blood *106*, 2200–2205.

Labbaye, C., Valtieri, M., Testa, U., Giampaolo, A., Meccia, E., Sterpetti, P., Parolini, I., Pelosi, E., Bulgarini, D., and Cayre, Y.E. (1994). Retinoic acid downmodulates erythroid differentiation and GATA1 expression in purified adult-progenitor culture. Blood *83*, 651–656.

Lam, W. a, Rosenbluth, M.J., and Fletcher, D. a (2007). Chemotherapy exposure increases leukemia cell stiffness. Blood *109*, 3505–3508.

Lam, W. a, Chaudhuri, O., Crow, A., Webster, K.D., Li, T.-D., Kita, A., Huang, J., and Fletcher, D. a (2011). Mechanics and contraction dynamics of single platelets and implications for clot stiffening. Nat. Mater. *10*, 61–66.

Lammerding, J., Fong, L.G., Ji, J.Y., Reue, K., Stewart, C.L., Young, S.G., and Lee, R.T. (2006). Lamins A and C but not lamin B1 regulate nuclear mechanics. J. Biol. Chem. *281*, 25768–25780.

Le, T., Williams, K., Senterman, M., Hopkins, L., Faught, W., and Fung-Kee-Fung, M. (2007). Histopathologic assessment of chemotherapy effects in epithelial ovarian cancer patients treated with neoadjuvant chemotherapy and delayed primary surgical debulking. Gynecol. Oncol. *106*, 160–163.

Lichtman, M.A. (1970). Cellular deformability during maturation of the myeloblast. Possible role in marrow egress. N. Engl. J. Med. *283*, 943–948.

Lichtman, M.A., Packman, C.H., and L.S., C. (1989). Handbook of the Hemopoietic Microenvironment (Clifton, NJ: The Humana Press Inc.).

Lindberg, F.P., Gao, A., Finn, M., Blystone, S., Brown, E., and Frazier, W.A. (1996). Integrin-associated Protein Is a Receptor for the C-terminal Domain of Thrombospondin. J. Biol. Chem. *271*, 21–24.

Liu, M., Imam, H., Oberg, K., and Zhou, Y. (2005). Gene transfer of vasostatin, a calreticulin fragment, into neuroendocrine tumor cells results in enhanced malignant behavior. Neuroendocrinology *82*, 1–10.

Liu, Y., Merlin, D., Burst, S.L., Pochet, M., Madara, J.L., and Parkos, C. a (2001). The role of CD47 in neutrophil transmigration. Increased rate of migration correlates with increased cell surface expression of CD47. J. Biol. Chem. *276*, 40156–40166.

Lordier, L., Bluteau, D., Jalil, A., Legrand, C., Pan, J., Rameau, P., Jouni, D., Bluteau, O., Mercher, T., Leon, C., et al. (2012). RUNX1-induced silencing of non-muscle myosin heavy chain IIB contributes to megakaryocyte polyploidization. Nat. Commun. *3*, 717.

Lu, Q., Hofferbert, B. V, Koo, G., and Malinauskas, R. a (2013). In vitro shear stress-induced platelet activation: sensitivity of human and bovine blood. Artif. Organs *37*, 894–903.

Ma, X., Jana, S.S., Conti, M.A., Kawamoto, S., Claycomb, W.C., and Adelstein, R.S. (2010). Ablation of nonmuscle myosin II-B and II-C reveals a role for nonmuscle myosin II in cardiac myocyte karyokinesis. Mol. Biol. Cell *21*, 3952–3962.

Majeti, R., Chao, M.P., Alizadeh, A. a, Pang, W.W., Jaiswal, S., Gibbs, K.D., van Rooijen, N., and Weissman, I.L. (2009). CD47 is an adverse prognostic factor and therapeutic antibody target on human acute myeloid leukemia stem cells. Cell *138*, 286–299.

Manna, P.P., and Frazier, W.A. (2004). CD47 mediates killing of breast tumor cells via Gi-dependent inhibition of protein kinase A. Cancer Res. *64*, 1026–1036.

Mantovani, A., Sozzani, S., Locati, M., Allavena, P., and Sica, A. (2002). Macrophage polarization: tumor-associated macrophages as a paradigm for polarized M2 mononuclear phagocytes. Trends Immunol. *23*, 549–555.

Matsumura, F. (2005). Regulation of myosin II during cytokinesis in higher eukaryotes. Trends Cell Biol. *15*, 371–377.

Mattia, G., Vulcano, F., Milazzo, L., Barca, A., Macioce, G., Giampalo, A., and Hassan, H.J. (2002). Different ploidy levels of megakaryocytes generated from peripheral or cord blood CD34+ cells are correlated with different levels of platelet release. Blood *99*, 888–897.

Maupin, P., Phillips, C.L., Adelstein, R.S., and Pollard, T.D. (1994). Differential localization of myosin-II isozymes in human cultured cells and blood cells. J. Cell Sci. *107 (Pt 1*, 3077–3090.

Mayer-Sonnenfeld, T., Har-Noy, M., Lillehei, K.O., and Graner, M.W. (2013). Proteomic analyses of different human tumour-derived chaperone-rich cell lysate (CRCL) anti-cancer vaccines reveal antigen content and strong similarities amongst the vaccines along with a basis for CRCL's unique structure: CRCL vaccine proteome leads to. Int. J. Hyperthermia *29*, 520–527.

Merideth, M.A., Gordon, L.B., Clauss, S., Sachdev, V., Smith, A.C.M., Perry, M.B., Brewer, C.C., Zalewski, C., Kim, H.J., Solomon, B., et al. (2008). Phenotype and course of Hutchinson-Gilford progeria syndrome. N. Engl. J. Med. *358*, 592–604.

Merkel, R., Simson, R., Simson, D. a, Hohenadl, M., Boulbitch, a, Wallraff, E., and Sackmann, E. (2000). A micromechanic study of cell polarity and plasma membrane cell body coupling in Dictyostelium. Biophys. J. *79*, 707–719.

Minard-Colin, V., Xiu, Y., Poe, J.C., Horikawa, M., Magro, C.M., Hamaguchi, Y., Haas, K.M., and Tedder, T.F. (2008). Lymphoma depletion during CD20 immunotherapy in mice is mediated by macrophage FcgammaRI, FcgammaRIII, and FcgammaRIV. Blood *112*, 1205–1213.

Mitruka, B., and Rowan, A. (1981). Clinical, biochemical and hematological reference values in normal experimental animals and normal humans (New York: Masson Publishing).

Miyake, T., Kung, C.K., and Goldwasser, E. (1977). Purification of human erythropoietin. J. Biol. Chem. *252*, 5558–5564.

Miyashita, M., Ohnishi, H., Okazawa, H., Tomonaga, H., Hayashi, A., Fujimoto, T., Furuya, N., and Matozaki, T. (2004). Promotion of neurite and filopodium formation by CD47: roles of integrins, Rac, and Cdc42. Mol. Biol. Cell *15*, 3950–3963.

Moise, K.J., and Argoti, P.S. (2012). Management and prevention of red cell alloimmunization in pregnancy: a systematic review. Obstet. Gynecol. *120*, 1132–1139.

Molina, A. (2008). A decade of rituximab: improving survival outcomes in non-Hodgkin's lymphoma. Annu. Rev. Med. *59*, 237–250.

Murdoch, C., Muthana, M., Coffelt, S.B., and Lewis, C.E. (2008). The role of myeloid cells in the promotion of tumour angiogenesis. Nat. Rev. Cancer *8*, 618–631.

Naetar, N., Korbei, B., Kozlov, S., Kerenyi, M. a, Dorner, D., Kral, R., Gotic, I., Fuchs, P., Cohen, T. V, Bittner, R., et al. (2008). Loss of nucleoplasmic LAP2alpha-lamin A complexes causes erythroid and epidermal progenitor hyperproliferation. Nat. Cell Biol. *10*, 1341–1348.

Naito, M., Omoteyama, K., Mikami, Y., Takagi, M., and Takahashi, T. (2012). Suppression of lamin A/C by short hairpin RNAs promotes adipocyte lineage commitment in mesenchymal progenitor cell line, ROB-C26. Histochem. Cell Biol. *137*, 235–247.

Nishino, T., Wang, C., Mochizuki-Kashio, M., Osawa, M., Nakauchi, H., and Iwama, A. (2011). Ex vivo expansion of human hematopoietic stem cells by garcinol, a potent inhibitor of histone acetyltransferase. PLoS One *6*, e24298.

North, T.E., Goessling, W., Peeters, M., Li, P., Ceol, C., Lord, A.M., Weber, G.J., Harris, J., Cutting, C.C., Huang, P., et al. (2009). Hematopoietic stem cell development is dependent on blood flow. Cell *137*, 736–748.

Notta, F., Doulatov, S., Laurenti, E., Poeppl, A., Jurisica, I., and Dick, J.E. (2011). Isolation of single human hematopoietic stem cells capable of long-term multilineage engraftment. Science *333*, 218–221.

Novershtern, N., Subramanian, A., Lawton, L.N., Mak, R.H., Haining, W.N., McConkey, M.E., Habib, N., Yosef, N., Chang, C.Y., Shay, T., et al. (2011). Densely interconnected transcriptional circuits control cell states in human hematopoiesis. Cell *144*, 296–309.

O'Brien, J.J., Spinelli, S.L., Tober, J., Blumberg, N., Francis, C.W., Taubman, M.B., Palis, J., Seweryniak, K.E., Gertz, J.M., and Phipps, R.P. (2008). 15-deoxy-delta12,14-PGJ2 enhances platelet production from megakaryocytes. Blood *112*, 4051–4060.

O'Brien, S.H., Ritchey, A.K., and Smith, K.J. (2007). A cost-utility analysis of treatment for acute childhood idiopathic thrombocytopenic purpura (ITP). Pediatr. Blood Cancer *48*, 173–180.

Oakes, P.W., Patel, D.C., Morin, N.A., Zitterbart, D.P., Fabry, B., Reichner, J.S., and Tang, J.X. (2009). Neutrophil morphology and migration are affected by substrate elasticity. Blood *114*, 1387–1395.

Obeid, M., Tesniere, A., Ghiringhelli, F., Fimia, G.M., Apetoh, L., Perfettini, J.-L., Castedo, M., Mignot, G., Panaretakis, T., Casares, N., et al. (2007). Calreticulin exposure dictates the immunogenicity of cancer cell death. Nat. Med. *13*, 54–61.

Oguro, H., Ding, L., and Morrison, S.J. (2013). SLAM family markers resolve functionally distinct subpopulations of hematopoietic stem cells and multipotent progenitors. Cell Stem Cell *13*, 102–116.

Oldenborg, P. -a. (2000). Role of CD47 as a Marker of Self on Red Blood Cells. Science (80-.). *288*, 2051–2054.

Olins, A.L., Zwerger, M., Herrmann, H., Zentgraf, H., Simon, A.J., Monestier, M., and Olins, D.E. (2008). The human granulocyte nucleus: Unusual nuclear envelope and heterochromatin composition. Eur. J. Cell Biol. *87*, 279–290.

Olson, E.N., and Nordheim, A. (2010). Linking actin dynamics and gene transcription to drive cellular motile functions. Nat. Rev. Mol. Cell Biol. *11*, 353–365.

Orford, K.W., and Scadden, D.T. (2008). Deconstructing stem cell self-renewal: genetic insights into cell-cycle regulation. Nat. Rev. Genet. *9*, 115–128.

Ou, G., Stuurman, N., D'Ambrosio, M., and Vale, R.D. (2010). Polarized myosin produces unequal-size daughters during asymmetric cell division. Science *330*, 677–680.

Pajerowski, J.D., Dahl, K.N., Zhong, F.L., Sammak, P.J., and Discher, D.E. (2007). Physical plasticity of the nucleus in stem cell differentiation. Proc. Natl. Acad. Sci. U. S. A. *104*, 15619–15624.

Pallasch, C.P., Leskov, I., Braun, C.J., Vorholt, D., Drake, A., Soto-Feliciano, Y.M., Bent, E.H., Schwamb, J., Iliopoulou, B., Kutsch, N., et al. (2014). Sensitizing protective tumor microenvironments to antibody-mediated therapy. Cell *156*, 590–602.

Pecci, A., Canobbio, I., Balduini, A., Stefanini, L., Cisterna, B., Marseglia, C., Noris, P., Savoia, A., Balduini, C.L., and Torti, M. (2005). Pathogenetic mechanisms of hematological abnormalities of patients with MYH9 mutations. Hum. Mol. Genet. *14*, 3169–3178.

Pelham, R.J., and Wang, Y.L. (1997). Cell locomotion and focal adhesions are regulated by the mechanical properties of the substrate. Proc. Natl. Acad. Sci. U. S. A. *94*, 13661–13665.

Peric-Hupkes, D., Meuleman, W., Pagie, L., Bruggeman, S.W.M., Solovei, I., Brugman, W., Gräf, S., Flicek, P., Kerkhoven, R.M., van Lohuizen, M., et al. (2010). Molecular maps of the reorganization of genome-nuclear lamina interactions during differentiation. Mol. Cell *38*, 603–613.

Pertusini, E., Ratajczak, J., Majka, M., Vaughn, D., Ratajczak, M.Z., and Gewirtz, a M. (2001). Investigating the platelet-sparing mechanism of paclitaxel/carboplatin combination chemotherapy. Blood *97*, 638–644.

Pollard, T.D., and Korn, E.D. (1973). Acanthamoeba myosin. I. Isolation from Acanthamoeba castellanii of an enzyme similar to muscle myosin. J. Biol. Chem. *248*, 4682–4690.

Raab, M., Swift, J., Dingal, P.C.D.P., Shah, P., Shin, J.-W., and Discher, D.E. (2012). Crawling from soft to stiff matrix polarizes the cytoskeleton and phosphoregulates myosin-II heavy chain. J. Cell Biol. *199*, 669–683.

Rajesh, D., Zhou, Y., Jankowska-Gan, E., Roenneburg, D.A., Dart, M.L., Torrealba, J., and Burlingham, W.J. (2010). Th1 and Th17 immunocompetence in humanized NOD/SCID/IL2rgammanull mice. Hum. Immunol. *71*, 551–559.

Reichl, E.M., Ren, Y., Morphew, M.K., Delannoy, M., Effler, J.C., Girard, K.D., Divi, S., Iglesias, P. a, Kuo, S.C., and Robinson, D.N. (2008). Interactions between myosin and actin crosslinkers control cytokinesis contractility dynamics and mechanics. Curr. Biol. *18*, 471–480.

Reinhold, M.I., Lindberg, F.P., Plas, D., Reynolds, S., Peters, M.G., and Brown, E.J. (1995). In vivo expression of alternatively spliced forms of integrin-associated protein (CD47). J. Cell Sci. *108 (Pt 1*, 3419–3425.

Ren, Y., Effler, J.C., Norstrom, M., Luo, T., Firtel, R. a, Iglesias, P. a, Rock, R.S., and Robinson, D.N. (2009). Mechanosensing through cooperative interactions between myosin II and the actin crosslinker cortexillin I. Curr. Biol. *19*, 1421–1428.

Rey, M., Valenzuela-Fernández, A., Urzainqui, A., Yáñez-Mó, M., Pérez-Martínez, M., Penela, P., Mayor, F., and Sánchez-Madrid, F. (2007). Myosin IIA is involved in the endocytosis of CXCR4 induced by SDF-1alpha. J. Cell Sci. *120*, 1126–1133.

Röber, R. a, Sauter, H., Weber, K., and Osborn, M. (1990). Cells of the cellular immune and hemopoietic system of the mouse lack lamins A/C: distinction versus other somatic cells. J. Cell Sci. *95 (Pt 4)*, 587–598.

Rodriguez, P.L., Harada, T., Christian, D. a, Pantano, D. a, Tsai, R.K., and Discher, D.E. (2013). Minimal "Self" peptides that inhibit phagocytic clearance and enhance delivery of nanoparticles. Science *339*, 971–975.

Rose, S., Misharin, A., and Perlman, H. (2012). A novel Ly6C/Ly6G-based strategy to analyze the mouse splenic myeloid compartment. Cytometry. A *81*, 343–350.

Sabin, F. (1928). Bone Marrow. Physiol. Rev. *8*, 151–190.

Samaniego, R., Sánchez-Martín, L., Estecha, A., and Sánchez-Mateos, P. (2007). Rho/ROCK and myosin II control the polarized distribution of endocytic clathrin structures at the uropod of moving T lymphocytes. J. Cell Sci. *120*, 3534–3543.

Sanda, M.G., Bolton, E., Mulé, J.J., and Rosenberg, S.A. (1992). In vivo administration of recombinant macrophage colony-stimulating factor induces macrophage-mediated antibody-dependent cytotoxicity of tumor cells. J. Immunother. (1991). *12*, 132–137.

Sarfati, M., Fortin, G., Raymond, M., and Susin, S. (2008). CD47 in the immune response: role of thrombospondin and SIRP-alpha reverse signaling. Curr. Drug Targets *9*, 842–850.

Savoia, A., De Rocco, D., Panza, E., Bozzi, V., Scandellari, R., Loffredo, G., Mumford, A., Heller, P.G., Noris, P., De Groot, M.R., et al. (2010). Heavy chain myosin 9-related disease (MYH9 -RD): neutrophil inclusions of myosin-9 as a pathognomonic sign of the disorder. Thromb. Haemost. *103*, 826–832.

Scaffidi, P., and Misteli, T. (2008). Lamin A-dependent misregulation of adult stem cells associated with accelerated ageing. Nat. Cell Biol. *10*, 452–459.

Schofield, R. (1978). The relationship between the spleen colony-forming cell and the haemopoietic stem cell. Blood Cells *4*, 7–25.

Schubert, A., Cattaruzza, M., Hecker, M., Darmer, D., Holtz, J., and Morawietz, H. (2000). Shear stress-dependent regulation of the human beta-tubulin folding cofactor D gene. Circ. Res. *87*, 1188–1194.

Schwertz, H., Köster, S., Kahr, W.H. a, Michetti, N., Kraemer, B.F., Weitz, D. a, Blaylock, R.C., Kraiss, L.W., Greinacher, A., Zimmerman, G. a, et al. (2010). Anucleate platelets generate progeny. Blood *115*, 3801–3809.

Sedzinski, J., Biro, M., Oswald, A., Tinevez, J.-Y., Salbreux, G., and Paluch, E. (2011). Polar actomyosin contractility destabilizes the position of the cytokinetic furrow. Nature *476*, 462–466.

Seri, M., Cusano, R., Gangarossa, S., Caridi, G., Bordo, D., Lo Nigro, C., Ghiggeri, G.M., Ravazzolo, R., Savino, M., Del Vecchio, M., et al. (2000). Mutations in MYH9 result in the May-Hegglin anomaly, and Fechtner and Sebastian syndromes. The May-Heggllin/Fechtner Syndrome Consortium. Nat. Genet. *26*, 103–105.

Seri, M., Pecci, A., Di Bari, F., Cusano, R., Savino, M., Panza, E., Nigro, A., Noris, P., Gangarossa, S., Rocca, B., et al. (2003). MYH9-related disease: May-Hegglin anomaly, Sebastian syndrome, Fechtner syndrome, and Epstein syndrome are not distinct entities but represent a variable expression of a single illness. Medicine (Baltimore). *82*, 203–215.

Shimi, T., Pfleghaar, K., Kojima, S., Pack, C.-G., Solovei, I., Goldman, A.E., Adam, S. a, Shumaker, D.K., Kinjo, M., Cremer, T., et al. (2008). The A- and B-type nuclear lamin

networks: microdomains involved in chromatin organization and transcription. Genes Dev. *22*, 3409–3421.

Shimi, T., Butin-Israeli, V., Adam, S. a, and Goldman, R.D. (2010). Nuclear lamins in cell regulation and disease. Cold Spring Harb. Symp. Quant. Biol. *75*, 525–531.

Shin, J.-W., Swift, J., Spinler, K.R., and Discher, D.E. (2011). Myosin-II inhibition and soft 2D matrix maximize multinucleation and cellular projections typical of platelet-producing megakaryocytes. Proc. Natl. Acad. Sci. U. S. A. *108*, 11458–11463.

Shin, J.-W., Spinler, K.R., Swift, J., Chasis, J. a, Mohandas, N., and Discher, D.E. (2013). Lamins regulate cell trafficking and lineage maturation of adult human hematopoietic cells. Proc. Natl. Acad. Sci. U. S. A. *110*, 18892–18897.

Shin, J.-W., Buxboim, A., Spinler, K.R., Swift, J., Christian, D. a, Hunter, C. a, Léon, C., Gachet, C., Dingal, P.C.D.P., Ivanovska, I.L., et al. (2014). Contractile forces sustain and polarize hematopoiesis from stem and progenitor cells. Cell Stem Cell *14*, 81–93.

Shin, M.E., He, Y., Li, D., Na, S., Chowdhury, F., Poh, Y., Collin, O., Su, P., de Lanerolle, P., Schwartz, M.A., et al. (2010). Spatiotemporal organization, regulation, and functions of tractions during neutrophil chemotaxis. Blood *116*, 3297–3310.

Shivashankar, G. V (2011). Mechanosignaling to the cell nucleus and gene regulation. Annu. Rev. Biophys. *40*, 361–378.

Shu, S., Liu, X., and Korn, E.D. (2005). Blebbistatin and blebbistatin-inactivated myosin II inhibit myosin II-independent processes in Dictyostelium. Proc. Natl. Acad. Sci. U. S. A. *102*, 1472–1477.

Smith, C.M., Burris, S.M., and White, J.G. (1989). Micropipette aspiration of guinea pig megakaryocytes: absence of fragmentation and dependence on maturation stage. Blood *73*, 1570–1575.

Sprent, J., and Basten, A. (1973). Circulating T and B lymphocytes of the mouse. II. Lifespan. Cell. Immunol. *7*, 40–59.

Steinert, G., Schölch, S., Niemietz, T., Iwata, N., García, S. a, Behrens, B., Voigt, A., Kloor, M., Benner, A., Bork, U., et al. (2014). Immune escape and survival mechanisms in circulating tumor cells of colorectal cancer. Cancer Res. *74*, 1694–1704.

Stiehler, M., Bünger, C., Baatrup, A., Lind, M., Kassem, M., and Mygind, T. (2009). Effect of dynamic 3-D culture on proliferation, distribution, and osteogenic differentiation of human mesenchymal stem cells. J. Biomed. Mater. Res. A *89*, 96–107.

Stockmeyer, B., Valerius, T., Repp, R., Heijnen, I.A., Bühring, H.J., Deo, Y.M., Kalden, J.R., Gramatzki, M., and van de Winkel, J.G. (1997). Preclinical studies with Fc(gamma)R bispecific antibodies and granulocyte colony-stimulating factor-primed neutrophils as effector cells against HER-2/neu overexpressing breast cancer. Cancer Res. *57*, 696–701.

Straight, A.F., Cheung, A., Limouze, J., Chen, I., Westwood, N.J., Sellers, J.R., and Mitchison, T.J. (2003). Dissecting temporal and spatial control of cytokinesis with a myosin II Inhibitor. Science *299*, 1743–1747.

Strowig, T., Rongvaux, A., Rathinam, C., Takizawa, H., Borsotti, C., Philbrick, W., Eynon, E.E., Manz, M.G., and Flavell, R.A. (2011). Transgenic expression of human signal regulatory protein alpha in Rag2-/-gamma(c)-/- mice improves engraftment of human hematopoietic cells in humanized mice. Proc. Natl. Acad. Sci. U. S. A. *108*, 13218–13223.

Swift, J., Ivanovska, I.L., Buxboim, A., Harada, T., Dingal, P.C.D.P., Pinter, J., Pajerowski, J.D., Spinler, K.R., Shin, J.-W., Tewari, M., et al. (2013). Nuclear lamin-A scales with tissue stiffness and enhances matrix-directed differentiation. Science *341*, 1240104.

Szilvassy, S.J., Humphries, R.K., Lansdorp, P.M., Eaves, a C., and Eaves, C.J. (1990). Quantitative assay for totipotent reconstituting hematopoietic stem cells by a competitive repopulation strategy. Proc. Natl. Acad. Sci. U. S. A. *87*, 8736–8740.

Takeda, K., Kishi, H., Ma, X., Yu, Z.-X., and Adelstein, R.S. (2003). Ablation and mutation of nonmuscle myosin heavy chain II-B results in a defect in cardiac myocyte cytokinesis. Circ. Res. *93*, 330–337.

Takenaka, K., Prasolava, T.K., Wang, J.C.Y., Mortin-Toth, S.M., Khalouei, S., Gan, O.I., Dick, J.E., and Danska, J.S. (2007). Polymorphism in Sirpa modulates engraftment of human hematopoietic stem cells. Nat. Immunol. *8*, 1313–1323.

Takeuchi, K., Satoh, M., Kuno, H., Yoshida, T., Kondo, H., and Takeuchi, M. (1998). Platelet-like particle formation in the human megakaryoblastic leukaemia cell lines, MEG-01 and MEG-01s. Br. J. Haematol. *100*, 436–444.

Teng, Y., Wang, X., Wang, Y., and Ma, D. (2010). Wnt/beta-catenin signaling regulates cancer stem cells in lung cancer A549 cells. Biochem. Biophys. Res. Commun. *392*, 373–379.

Thomas, E.D., Lochte, H.L., Lu, W.C., and Ferrebee, J.W. (1957). Intravenous infusion of bone marrow in patients receiving radiation and chemotherapy. N. Engl. J. Med. *257*, 491–496.

Thompson, C.B., and Jakubowski, J. a (1988). The pathophysiology and clinical relevance of platelet heterogeneity. Blood *72*, 1–8.

Thon, J.N., Montalvo, A., Patel-Hett, S., Devine, M.T., Richardson, J.L., Ehrlicher, A., Larson, M.K., Hoffmeister, K., Hartwig, J.H., and Italiano, J.E. (2010). Cytoskeletal mechanics of proplatelet maturation and platelet release. J. Cell Biol. *191*, 861–874.

Thon, J.N., Macleod, H., Begonja, A.J., Zhu, J., Lee, K.-C., Mogilner, A., Hartwig, J.H., and Italiano, J.E. (2012). Microtubule and cortical forces determine platelet size during vascular platelet production. Nat. Commun. *3*, 852.

Tiblad, E., Taune Wikman, A., Ajne, G., Blanck, A., Jansson, Y., Karlsson, A., Nordlander, E., Holländer, B.S., and Westgren, M. (2013). Targeted routine antenatal anti-D prophylaxis in the prevention of RhD immunisation--outcome of a new antenatal screening and prevention program. PLoS One *8*, e70984.

Ting, S.B., Deneault, E., Hope, K., Cellot, S., Chagraoui, J., Mayotte, N., Dorn, J.F., Laverdure, J., Harvey, M., Hawkins, E.D., et al. (2012). Asymmetric segregation and self-renewal of hematopoietic stem and progenitor cells with endocytic Ap2a2. Blood *119*, 2510–2522.

Trumpp, A., Essers, M., and Wilson, A. (2010). Awakening dormant haematopoietic stem cells. Nat. Rev. Immunol. *10*, 201–209.

Tsai, R.K., and Discher, D.E. (2008). Inhibition of "self" engulfment through deactivation of myosin-II at the phagocytic synapse between human cells. J. Cell Biol. *180*, 989–1003.

Tullio, a N., Accili, D., Ferrans, V.J., Yu, Z.X., Takeda, K., Grinberg, a, Westphal, H., Preston, Y. a, and Adelstein, R.S. (1997). Nonmuscle myosin II-B is required for normal development of the mouse heart. Proc. Natl. Acad. Sci. U. S. A. *94*, 12407–12412.

Ubukawa, K., Guo, Y., Takahashi, M., Hirokawa, M., Michishita, Y., Nara, M., Tagawa, H., Takahashi, N., Komatsuda, A., Nunomura, W., et al. (2012). Enucleation of human erythroblasts involves non-muscle myosin IIB. Blood *119*, 1036–1044.

Ulrich, T. a, de Juan Pardo, E.M., and Kumar, S. (2009). The mechanical rigidity of the extracellular matrix regulates the structure, motility, and proliferation of glioma cells. Cancer Res. *69*, 4167–4174.

Valerius, T., Repp, R., de Wit, T.P., Berthold, S., Platzer, E., Kalden, J.R., Gramatzki, M., and van de Winkel, J.G. (1993). Involvement of the high-affinity receptor for IgG (Fc gamma RI; CD64) in enhanced tumor cell cytotoxicity of neutrophils during granulocyte colony-stimulating factor therapy. Blood *82*, 931–939.

Vascotto, F., Lankar, D., Faure-André, G., Vargas, P., Diaz, J., Le Roux, D., Yuseff, M.-I., Sibarita, J.-B., Boes, M., Raposo, G., et al. (2007). The actin-based motor protein myosin II regulates MHC class II trafficking and BCR-driven antigen presentation. J. Cell Biol. *176*, 1007–1019.

Vicente-Manzanares, M., Koach, M. a, Whitmore, L., Lamers, M.L., and Horwitz, A.F. (2008). Segregation and activation of myosin IIB creates a rear in migrating cells. J. Cell Biol. *183*, 543–554.

Vogel, V., and Sheetz, M. (2006). Local force and geometry sensing regulate cell functions. Nat. Rev. Mol. Cell Biol. *7*, 265–275.

De Vos, W.H., Houben, F., Kamps, M., Malhas, A., Verheyen, F., Cox, J., Manders, E.M.M., Verstraeten, V.L.R.M., van Steensel, M. a M., Marcelis, C.L.M., et al. (2011). Repetitive disruptions of the nuclear envelope invoke temporary loss of cellular compartmentalization in laminopathies. Hum. Mol. Genet. *20*, 4175–4186.

Wang, N., Tytell, J.D., and Ingber, D.E. (2009). Mechanotransduction at a distance: mechanically coupling the extracellular matrix with the nucleus. Nat. Rev. Mol. Cell Biol. *10*, 75–82.

Wang, Y., Xu, Z., Guo, S., Zhang, L., Sharma, A., Robertson, G.P., and Huang, L. (2013). Intravenous delivery of siRNA targeting CD47 effectively inhibits melanoma tumor growth and lung metastasis. Mol. Ther. *21*, 1919–1929.

Waugh, R.E., Mantalaris, a, Bauserman, R.G., Hwang, W.C., and Wu, J.H. (2001). Membrane instability in late-stage erythropoiesis. Blood *97*, 1869–1875.

Weinbaum, S., Cowin, S.C., and Zeng, Y. (1994). A model for the excitation of osteocytes by mechanical loading-induced bone fluid shear stresses. J. Biomech. *27*, 339–360.

Weiskopf, K., Ring, A.M., Ho, C.C.M., Volkmer, J.-P., Levin, A.M., Volkmer, A.K., Ozkan, E., Fernhoff, N.B., van de Rijn, M., Weissman, I.L., et al. (2013). Engineered SIRPα variants as immunotherapeutic adjuvants to anticancer antibodies. Science *341*, 88–91.

Weissman, I.L., and Shizuru, J.A. (2008). The origins of the identification and isolation of hematopoietic stem cells, and their capability to induce donor-specific transplantation tolerance and treat autoimmune diseases. Blood *112*, 3543–3553.

Welsh, T.J., Green, R.H., Richardson, D., Waller, D. a, O'Byrne, K.J., and Bradding, P. (2005). Macrophage and mast-cell invasion of tumor cell islets confers a marked survival advantage in non-small-cell lung cancer. J. Clin. Oncol. *23*, 8959–8967.

Wendtner, C.-M., Ritgen, M., Schweighofer, C.D., Fingerle-Rowson, G., Campe, H., Jäger, G., Eichhorst, B., Busch, R., Diem, H., Engert, a, et al. (2004). Consolidation with alemtuzumab in patients with chronic lymphocytic leukemia (CLL) in first remission--experience on safety and efficacy within a randomized multicenter phase III trial of the German CLL Study Group (GCLLSG). Leukemia *18*, 1093–1101.

White, J.G., Burris, S.M., Tukey, D., Smith, C., and Clawson, C.C. (1984). Micropipette aspiration of human platelets: influence of microtubules and actin filaments on deformability. Blood *64*, 210–214.

Willingham, S.B., Volkmer, J.-P., Gentles, A.J., Sahoo, D., Dalerba, P., Mitra, S.S., Wang, J., Contreras-Trujillo, H., Martin, R., Cohen, J.D., et al. (2012). The CD47-signal regulatory protein alpha (SIRPa) interaction is a therapeutic target for human solid tumors. Proc. Natl. Acad. Sci. U. S. A. *109*, 6662–6667.

Wilson, C. a, Tsuchida, M. a, Allen, G.M., Barnhart, E.L., Applegate, K.T., Yam, P.T., Ji, L., Keren, K., Danuser, G., and Theriot, J. a (2010). Myosin II contributes to cell-scale actin network treadmilling through network disassembly. Nature *465*, 373–377.

Yamazaki, S., Ema, H., Karlsson, G., Yamaguchi, T., Miyoshi, H., Shioda, S., Taketo, M.M., Karlsson, S., Iwama, A., and Nakauchi, H. (2011). Nonmyelinating Schwann cells maintain hematopoietic stem cell hibernation in the bone marrow niche. Cell *147*, 1146–1158.

Zang, J.H., Cavet, G., Sabry, J.H., Wagner, P., Moores, S.L., and Spudich, J. a (1997). On the role of myosin-II in cytokinesis: division of Dictyostelium cells under adhesive and nonadhesive conditions. Mol. Biol. Cell *8*, 2617–2629.

Zeng, L., Xiao, Q., Margariti, A., Zhang, Z., Zampetaki, A., Patel, S., Capogrossi, M.C., Hu, Y., and Xu, Q. (2006). HDAC3 is crucial in shear- and VEGF-induced stem cell differentiation toward endothelial cells. J. Cell Biol. *174*, 1059–1069.

Zermati, Y., Garrido, C., Amsellem, S., Fishelson, S., Bouscary, D., Valensi, F., Varet, B., Solary, E., and Hermine, O. (2001). Caspase activation is required for terminal erythroid differentiation. J. Exp. Med. *193*, 247–254.

Zhang, Y., Conti, M.A., Malide, D., Dong, F., Wang, A., Shmist, Y. a, Liu, C., Zerfas, P., Daniels, M.P., Chan, C.-C., et al. (2012). Mouse models of MYH9-related disease: mutations in nonmuscle myosin II-A. Blood *119*, 238–250.

Zwerger, M., Herrmann, H., Gaines, P., Olins, A.L., and Olins, D.E. (2008). Granulocytic nuclear differentiation of lamin B receptor-deficient mouse EPRO cells. Exp. Hematol. *36*, 977–987.